Quantum acoustics with diamond color centers

Quantum acoustics with diamond color centers

A dissertation presented
by

Srujan Meesala

to
The Department of Engineering and Applied Sciences
in partial fulfillment of the requirements
for the degree of
Doctor of Philosophy
in the subject of
Applied Physics

Harvard University
Cambridge, Massachusetts
May 2019

Quantum acoustics with diamond color centers

Abstract

Realization of physical systems for quantum information processing fundamentally rests on the ability to generate entanglement among many quantum bits. To this end, solid state quantum systems are often considered a scalable approach due to the relative ease of generating of a large number of individual qubits. However, realizing strong coherent interactions that dominate decoherence processes in the solid state environment is a formidable challenge that has continued to motivate the investigation of new physical systems to store quantum information and new mechanisms to achieve controllable interactions. This thesis takes steps in these directions with diamond color centers, which can store optically accessible quantum information in their electronic spin. We study color center spins as acoustic two level systems, and consider whether their interaction with single phonons in diamond can be engineered to be coherent. Through spectroscopy of color centers in diamond nanomechanical devices and follow-up theoretical work, we identify the negatively charged silicon vacancy (SiV) color center as a promising candidate for phonon-mediated quantum information processing. In the process, an electromechanical device platform capable of tuning the strain environment of color centers is developed. It is used to mitigate thermal decoherence of the SiV spin and demonstrate photon-mediated quantum interference between two SiV centers on a diamond chip, highlighting the utility of nanomechanical devices for photonic quantum networks. Finally, we present high quality factor, wavelength scale acoustic resonators in diamond using phononic crystals towards a coherent interface between SiV centers and single phonons.

Contents

Citations to published work

Many chapters of this thesis have appeared in print elsewhere. In order, they are:

Chapter 1: S Meesala*, Y-I Sohn*, H A Atikian, S Kim, M J Burek, J T Choy, M Lončar, "Enhanced strain coupling of nitrogen-vacancy spins to nanoscale diamond cantilevers", *Phys. Rev. Appl.* **5**, 3 (2016)

Chapter 2: S Meesala*, Y-I Sohn*, B Pingault, L Shao, H A Atikian, J Holzgrafe, M Gundogan, C Stavrakas, A Sipahigil, C Chia, M J Burek, M Zhang, J L Pacheco, J Abraham, E Bielejec, M D Lukin, M Atature, M Lončar, "Strain engineering of the silicon vacancy center in diamond", *Phys. Rev. B* **97**, 205444 (2018)

Chapter 3: B J Machielse*, S Bogdanovic*, S Meesala*, S Gauthier, M J Burek, G Joe, M Chalupnik, Y-I Sohn, J Holzgraffe, R E Evans, C Chia, M K Bhaskar, D Sukachev, L Shao, S Maity, M D Lukin, M Lončar, "Electromechanical control of quantum emitters in nanophotonic devices", arXiv:1901.09103 (2019)

Chapter 4: Y-I Sohn*, S Meesala*, B Pingault*, H A Atikian, J Holzgrafe, M Gundogan, C Stavrakas, M J Stanley, A Sipahigil, J Choi, M Zhang, J L Pacheco, J Abraham, E Bielejec, M D Lukin, M Atature, M Lončar, "Controlling the coherence of a diamond spin qubit through strain engineering", *Nat. Commun.* **9**, 2012 (2018)

Chapter 5: S Meesala*, Y-I Sohn*, B Pingault, L Shao, H A Atikian, J Holzgrafe, M Gundogan, C Stavrakas, A Sipahigil, C Chia, M J Burek, M Zhang, J L Pacheco, J Abraham, E Bielejec, M D Lukin, M Atature, M Lončar, "Strain engineering of the silicon vacancy center in diamond", *Phys. Rev. B* **97**, 205444 (2018)

Chapter 7: M-A Lemonde, S Meesala, A Sipahigil, M J A Schuetz, M D Lukin, M Lončar, P Rabl, "Phonon networks with SiV centers in diamond", *Phys. Rev. Lett.* **120**, 213603 (2018)

* indicates equal contribution

To my family

Acknowledgments

I am incredibly fortunate to have been advised by Marko Lončar. Marko's bold dreams of fabricating devices in materials that no sane fabber would think of etching and his initiative to create and perfect them has led to new avenues in nanophotonics and nanomechanics, quantum and classical. His imagination and enthusiasm fueled me through the highs and lows of my PhD. These attributes can only be matched by his boundless patience, which meant there was always an ear for the most stubborn issues, experimental and existential, and there was always time to tell stories about science and life. I will always be indebted to Marko for his mentorship.

I am grateful to my committee members, Misha Lukin and Evelyn Hu. Having started my PhD as an electrical engineer, Misha's excellent teaching filled with crisp physical insights provided most of my background in AMO physics. The many intellectually stimulating discussions with friends and colleagues in his group, not to mention frequent exchange of equipment and expertise, were key enablers of the work in this thesis. I want to thank Evelyn for her valuable scientific and professional advice and above all, unmatched kindness over the years. I was also lucky to have shared an office with the Hu group at multiple points during my PhD.

A good chunk of the work in this thesis would have been impossible without fantastic collaborations across the pond. I want to thank Mete Atature for essentially providing a second PhD home in Cambridge UK, leading to the work in Chapters 2 and 4. My time as a visitor in his group left me with much expertise in spectroscopy and more importantly, helped me rediscover the joy of doing science, which was easy to lose sight of in fast-paced Cambridge MA. For this, I am grateful to Mete. I want to thank Peter Rabl and Marc Antoine-Lemonde for letting me try my hand at theory in a fruitful collaboration that led to the work in Chapter 7. Peter's seminal theory papers pushed me to think about coupling defects to phonons very early on in my PhD, and conversations with him continue to be enriching.

Over the seven years of my PhD, I have worked with and learned from many incredibly talented and hardworking people. I can only begin by thanking Young-Ik Sohn, partner in crime for most of my PhD. Young-Ik's tenacity in the clean room and at the optical bench is only matched by his enthusiasm for politics, past and present, making him the ideal companion for late night Bon Me. We shared both the joy of watching diamond MEMS deflect for the first time in the lab, and the subsequent frustration of watching them literally explode due to mysterious surface currents. Young-Ik's calm and methodical approach was essential to tame the long tail of technical challenges that can arise while working with diamond devices. Somewhere in the middle of our PhDs, we joined hands with Ben

Pingault, who performed some of the early pioneering spectroscopy work on the SiV. In its openness and friendship, this triumvirate will continue to be a role model for any scientific collaborations I undertake in the future. I don't miss our constant back and forth between the laser room and cryostat room in Rutherford but I do miss the longer walks from the Cavendish to the town center. I am excited for Ben to join the Lončar family more formally as a postdoc.

I am lucky to have overlapped with Mike Burek for a substantial chunk of my time at Harvard. Mike taught me diamond fabrication in my first year, and everything I know about lab organization in my subsequent years - from building a proper shelf to neatly routing cables. Mike and I also shared the experience of designing the first diamond optomechanical crystals during my first year, and eventually building the Montana setup towards the end of my PhD to finally marry these devices with color centers. I am thankful to Haig Atikian for teaching me the art of cryostat surgery and for his astute insights on science and life. Haig and I shared the joy and frustration of inaugurating both the McKay basement lab and Faraday cage room with new confocal microscopes shortly after the first generation of Marko's diamonds left the group. Our misadventures trying to measure SNSPDs on diamond eventually led him to pioneer a new diamond etching technique, which generated cantilevers for all the experiments in this thesis. Beyond our technical collaboration, I thank him for his friendship and generosity, for all the car rides and subsequent food coma without which I would not have made it through grad school.

Of the first generation, I am especially thankful to Jen Choy. Jen taught me how to build a confocal microscope in my first year, and oversaw my fledgling efforts to set up ESR and cryogenic measurement capabilities for NV centers. I can only aspire to be as patient and kind a mentor as Jen. I am excited for her new stint at UW Madison, and am looking forward to more PlayStation time with her in the near future. During those early days of setup build-up, I was fortunate to have worked closely with two exceptional undergrads. Sam Kim developed flawless Labview infrastructure for the NV experiments. His VIs are still being somewhat poorly repurposed as he ponders weighty problems at the intersection of machine learning and physics down the river at MIT. Jeff Holzgrafe and I took the very first SiV spectra in the basement lab during a summer in which he taught me much about hacking old equipment and taking meticulous lab notes. He continued to be a presence through my time in Cambridge UK and is now back in the Lončar group working on lithium niobate. Sam and Jeff, who are both formidable PhD students now, made me discover the joy of learning through mentoring, and for this, I will remain grateful to them.

More recently, I have had the pleasure of working closely with Bart Machielse and Stefan Bogdanovic on my first two-emitter experiments. Bart has taken the diamond fabrication toolkit to new heights through the herculean task of combining every modality developed in the lab even as he continues to add more capabilities by the day. I am constantly impressed by his ability to instantly pick up new concepts and to seamlessly switch between the clean room, optical bench and whiteboard, all fueled by his impeccable work ethic. Stefan has been instrumental in expanding the measurement capabilities in the basement lab. His clarity of thinking has been invaluable to me and the diamond team as a whole over the past year and a half, often providing much needed direction in times of confusion. I have enjoyed our many fun outings in Boston area, but most of all admire

him for successfully turning Rustica into a lab institution.

I am grateful to Cleaven Chia for all his efforts on the optomechanics project over the years. Cleaven's perseverance through the many ups and downs of the effort, often tied to the uncontrollable whims of CNS diamond etchers make him a paragon of dedication to ideas. I am excited beyond words for the newly resurrected OMC devices and their potential to explore single phonon level effects with SiV spins. Thanks to Graham Joe and Michelle Chalupnik for the excellent teamwork in measuring version 2.0 of OMCs just weeks before my thesis defense. I am confident that along with the new diamond cohort, they will transform the basement lab into the Diamond Underground.

While the larger diamond community at Harvard has undoubtedly been a central part of my PhD experience, I am especially indebted to the Lukin SiV team. Alp Sipahigil was a beacon of constant good news in the early days of transitioning from the NV to the SiV and convinced me that I was on the right path. I am grateful to Alp for the many whiteboard brainstorming sessions and the valuable sanity checks on fresh experimental results. Ruffin Evans' advice was crucial to make it through the dark days of NVs in nanostructures. His tips and tricks for furnace building and cryostat hacking can only be superseded by his friendship and support during the final days of finishing this thesis. I am thankful to Denis Sukachev, Christian Nguyen and Mihir Bhaskar for enriching discussions and for help with annealing samples.

A major highlight of my grad school experience was serving as a teaching fellow for Federico Capasso's optics and photonics course. Through his curiosity-driven approach to both teaching and doing science, Federico and through him, the students in the class taught me much that will remain with me after leaving Harvard. With the class being taught for the first time, my labmate and co-TF, Zin Lin and I had the rare opportunity to design a large chunk of the course material, an endeavor which made the teaching experience all the more rewarding. Zin's pure, unadulterated passion for science continues to inspire me. Another incredibly rewarding teaching/learning experience was working with the team of Carol Lynn Alpert and Karine Thate on the Quantum Matters event at the Museum of Science, Boston. This experience greatly sharpened my ability to communicate science and forced me to rethink quantum mechanics as if I were a child approaching it for the first time.

There are still more labmates I am fortunate to have interacted with during my PhD. I feel privileged to have learned diamond sample prep and annealing from the Queen of Diamonds herself, Birgit Hausmann. Grad school was a lot brighter thanks to adventures with Birgit, both in Cambridge and California. I am grateful to Vivek Venkataraman for many whiteboard discussions and for being a voice of moderation for my more outlandish ideas early on in my PhD. Thanks to I-Chun Huang for all the fun we had working on SiVs in plasmonic apertures. I enjoyed interacting with Smarak Maity and Linbo Shao over the course of the GeV strain tuning project and more recently on the fastest experiment of my PhD, SAW driving of SiV spins. Thanks to Scarlett Gauthier for her patience with the most fickle Fabry-Perot cavity and to Nayera El-Sawah for all the help with measurements on OMCs 1.0. Thanks to Erika Janitz for the fun with NVs in the Janis and for the most adventurous summer in Boston. I am grateful to Pawel Latawiec for always being the calm voice of reason, most notably and recently in dealing with the leader of Colombia. Amirhassan Shams Ansari, thank you, my friend, nice to meet you. Thanks to Anna

Shneidman, Cheng Wang, Stefan Kalchmair, Thibaud Ruelle, Daniel Assumpcao, Eric Puma, Neil Sinclair and Boris Desiatov for being wonderful officemates in 219/213/B7. Thanks to Yinan Zhang for being Yinan Zhang. Going further back in time, I am ever so grateful to Parag Deotare who mentored me during my gateway stint in the lab as an undergrad intern. This wonderful experience convinced me to come back to Harvard for grad school. Thanks to Leo Kogos and Dan Ramos for the fun times that summer in the clean room and at the resonant scattering setup.

I am thankful to my labmates in the Atature group and SiV partners in crime, Mustafa Gündogan and Camille Stavrakas. I continue to fear the Cavendish jacket potato and miss The Vending Machine. I am grateful to Christian Hepp for the initial wave of stimulating conversations in Oxford and Cambridge that led to the SiV strain tuning work. Christian's thesis has also been an invaluable resource to me and much of the diamond community. Coming back to Harvard, I have gained much insight from discussions with Kristiaan De Greve, Nathalie de Leon, Jan Gieseler, Martin Schuetz, Aaron Kabcenell and Hannes Bernien in the Lukin group. Thanks to Joonhee Choi for his thorough and insightful model for the double dip CPT feature on the high strain SiV experiment. Thanks to Yiwen Chu for her support and friendly advice over the years. I am grateful to Arthur Safira, carrier of all news and stories on Oxford St and beyond, for his friendship and constant support, especially in the final days of grad school. Thanks to Matt Turner and Nick Langellier in the Walsworth group and to Edlyn Levine for all the fun on the IC imaging project towards the end of my PhD. I have learned much about diamond growth and surface preparation from Alex Zhang, Andy Greenspon and Shanying Cui in the Hu group. I am grateful to Bob Westervelt and Naomi Brave for their incredible work in running CIQM, which provided me an excellent platform to meet other 'quantum people'. Thanks to Norman Yao and his students for all the stimulating discussions and special interest in strained diamond; I am incredibly excited for their upcoming experiments. Members of the Vuckovic diamond team - Marina Radulaski, Constantin Dory, Alison Rugar and Shuo Sun have been like extended family. Thanks in particular to Shuo for finding a hard-to-track calculation error in the PRB paper on SiV strain response. I am thankful to Ronald Hanson, Tim Taminiau, Simon Groeblacher and their students for the stimulating discussions during my time in Delft.

My PhD would have been impossible without the constant support of Kathy Masse and Stacia Zatsiorsky. Thanks to Kathy for helping me with tracking everything from Marko to my reimbursements and for Horsin' Around in her emails. Thanks to Stacia for promptly approving every single one of my last minute iprocurement requests. I am grateful to Jim MacArthur and Mike McKenna for turning many ambiguous drawings into functioning PCBs and parts for various experiments in this thesis. Thanks to folks at CNS without whom none of the amazing devices that are the cornerstones of this thesis would exist. I am personally thankful to Greg Lin for his help with XPS and Jason Tresback for advice on imaging diamond MEMS deflection.

Throughout grad school, my friends outside the lab ensured there was not a single dull moment. Raji Shankar was one of the few who stood firmly at the lab/life boundary, always with snacks and stories. I eagerly await her production of 11 Wendell, co-written by Xinghui Yin. I am grateful to Priyanka DeSouza for our long friendship that has now traveled four continents, and am constantly amazed by her tireless work as Chief Wow

Officer of my life. Thanks to Kit Heintzman, Lucas Mueller and Ashawari Chaudhuri for making me think more critically about science and for profoundly shaping my worldview, but really for just always being there and being the coolest. Carmen Palacios-Berraquero has brought much excitement and perspective to my life; she continues to astound me with her ability to juggle qutting edge science and qutting edge music. Thanks to Vivien Chong, Ali Hamandi, Mikey Reback, Fiz Poliks, Arick Wong, Lenny Schnier, Önder Gül, Tanja Vuksanovic, Margaret Hayden and Sanjay Kishore for making Boston warmer and worth it. I am grateful to Jonathan Ripley for nurturing my interest in Tamil and to Aditya Menon and Iraj de Alwis for the shenanigans that followed. I am fortunate to know Martin Falk and to have shared many soups, sweets and long walks with him. I am grateful to Queen Susanna, Balthasar Müller, Sarada Anne, Nishad Avari, Indrasen Bhattacharya, Jimmy Narang, Aditya Vikram, Vinit Atal, Nitish Reddy and Anupama Kumar for their open homes, open hearts and slightly crazy minds; I will remember every time I have traveled far to see them.

Words will never express how thankful I am to my family. My grandparents raised me through my early childhood teaching me to be curious; their idealism and humility will always inspire me. My parents were the first to teach me maths, science and how to build things. My sister, Smruthi constantly amazes me with her academic drive and ability to put up with me. Their countless sacrifices and unconditional love are the reason I could reach this milestone.

Chapter 0

Introduction

0.1 Background

Quantum mechanics arose at the beginning of the previous century from the need for a microscopic theory to explain phenomena such as black-body radiation and the photoelectric effect, which were at odds with classical physics. In the decades that followed, as ideas of quantum physics gained wider scientific acceptance, they had enormous technological impact, most notably through revolutionizing our understanding of chemistry and the development of solid state physics. The latter led to devices such as the transistor and the laser, and eventually modern day computing and telecommunication. In parallel, our ability to probe materials and the natural world was revolutionized through the development of new sensing and imaging technologies such as scanning electron microscopy (SEM) and magnetic resonance imaging (MRI).

While all of the above technologies have quantum mechanics at their heart, they can for the most part be qualitatively explained by the single particle behavior of atoms and electrons and the interaction of classical electromagnetic fields with dipoles. Rarely does one have to invoke coherent interactions and interference between individual quantum entities in the ensemble, let alone the more classically non-intuitive effect of entanglement. In con-

trast with this first wave of quantum technologies, the past few decades have seen rapid development in our ability to isolate, control and measure individual atom-like systems and single photons. Moreover, one can now assemble many such quantum building blocks and control the interactions between them. These capabilities have brought with them the promise of a new wave of technologies through the advent of quantum information science.

Storing and processing information in the form of entangled states of quantum bits or qubits and realizing a quantum computer can lead to dramatic, sometimes exponential reduction in the computational complexity of certain problems in computer science and chemistry[1]. Quantum communication, i.e. transmitting information using quantum states of light can offer theoretically secure communication and the ability to link distinct quantum computing modules. Quantum correlations can be utilized to enhance the sensitivity of measurements in certain scenarios to achieve sensitivity better than that of classical systems; this is now referred to as quantum sensing. Finally and more fundamentally, the physical realization of controllable quantum many-body systems essential to many of these technologies could make it possible to simulate several phenomena in condensed matter physics and understand the microscopic mechanisms that govern them.

Presently, several atom-like systems are being explored to realize quantum information processing in its various avatars. These fall into the categories of 'natural' systems such as neutral atoms, ions and molecules, and 'artificial' atom-like systems in solids such as superconducting circuits, quantum dots and defect centers. In the context of quantum computing and simulation, some of these platforms are at the cusp of scaling from few to many qubits and hence into the regime where it may not be possible to efficiently classically simulate their behavior[2]. In the context of quantum communication and quantum networks, following demonstrations of the basic ingredients of a quantum repeater through remote entanglement[3] and quantum teleportation[4], work is underway to improve entanglement generation rates and scale to a larger number of nodes[5]. It is also beginning to be believed that quantum network schemes may offer a more modular approach to build

a quantum processor[6]. While these developments have inspired much excitement, tremendous challenges remain en route to the more ambitious goals of quantum information processing such as a universal quantum computer or a large quantum simulator or network.

The gap between the requirements for these goals and current experimental state of the art often boils down to the need for a larger difference in scale between the rate of coherent interaction (or entanglement generation) between qubits and the rates of decoherence processes. It is also crucial to maintain a large ratio between coherence and decoherence as one scales up to a large number of qubits. A central challenge in this context is the tradeoff between controllability and isolation. A high susceptibility to the physical quantity used to control a single qubit and couple it to another can also expose it to a decoherence mechanism. Due to their complex environment, solid state systems can be susceptible to multiple decoherence mechanisms, such as electric, magnetic and thermal fluctuations. These considerations have motivated the study of a variety of solid state quantum platforms, each with distinct decoherence phenomena and distinct physical fields for control and mutual coupling.

In this thesis, we study color centers in diamond as a platform for quantum information processing. Color centers are luminescent point defects in a wide bandgap crystal, typically formed by a dopant atom acting as a substituional impurity at a lattice site. The orbitals of the dopant atom hybridize with nearest neighboring host atoms to form electronic states that lie within the bandgap of the host crystal. These systems can often be qualitatively treated as trapped molecules. Transitions between distinct electronic configurations of these molecules lie in the optical frequency range. By virtue of being embedded in the host, these electronic states couple to phonons in the host crystal. Additionally, the spin degree of freedom of the electronic levels can be long-lived and serve as a memory qubit. Resonance fluorescence can be used to map the quantum state of this memory onto a photon that can be sent over long distances. This makes color centers particularly well-suited for quantum networks. Indeed the past decade has seen several pioneering demonstrations

in this context with nitrogen vacancy (NV) centers in diamond[3,4,5].

However, generating controllable local interactions between color center electron spins in the same crystal is challenging. Magnetic dipolar coupling would be the most obvious physical mechanism and indeed this has been used to show two-qubit gates in registers with a single color center spin and naturally occurring, neighboring nuclear spins[7]. However, a more scalable approach would require deterministic placement of spins with ∼nm precision to achieve interaction strengths that exceed decoherence from the nuclear spin bath in the crystal, and this is experimentally very challenging[8]. This motivates the search for other physical mechanisms to achieve effective interactions between them. In this thesis, we look at photons and phonons as intermediaries to this end. The photonic approach is extensively studied in the framework of cavity quantum electrodynamics (QED)[9], and fits into the narrative of the color center as a spin-photon interface for quantum networks. The tools of cavity QED can also be readily transferred to the more exploratory phononic approach[10], which is appealing from the point of view of either realizing a chipscale quantum information processor with spins or to couple spins to other qubits[11]. We will see that with the use of appropriate nanoscale devices, either approach requires the placement of color centers to within the optical or acoustic wavelength (100 nm - 1 μm), which is easily achievable with current nanofabrication techniques[12,13]. The chapters of this thesis will often alternate between both these approaches and the slightly different narratives associated with them.

Finally, the push towards quantum information applications with color centers can lead to greater insight into a variety of phenomena in solid state physics. This is made possible by using color centers as atomic scale sensors for the same physical fields that cause decoherence. The most relevant example is the development of high spatial resolution magnetometry with NV centers[14].

0.2 Cavity quantum electrodynamics

Cavity QED refers to the study of interactions between atoms and light confined in a cavity. Canonically, one considers an atom that can exchange a single photon coherently with the cavity field at the rate g as in Fig. 1. In principle, the framework holds for any two oscillators. The atomic state decoheres at the rate γ, for instance due to spontaneous emission into non cavity modes, while the cavity has a damping rate κ. When the coherent rate g far exceeds the dephasing and dissipative rates γ, κ, the atom and cavity are said to be strongly coupled. This regime provides access to quantum non-linearities for single photons and allows entanglement generation between the atom and photons in the cavity[15]. The cavity QED approach has been used across multiple physical platforms to demonstrate quantum gates between atoms[16,17,18]. From a photon extraction standpoint, the cavity provides a means to engineer the atom to dominantly emit into a single well-defined mode, for instance that of an optical fiber[19]. Subsequently, photons in this mode can either be measured or routed to another cavity QED module. This is believed to be a modular or scalable approach to build a quantum processor or network[9].

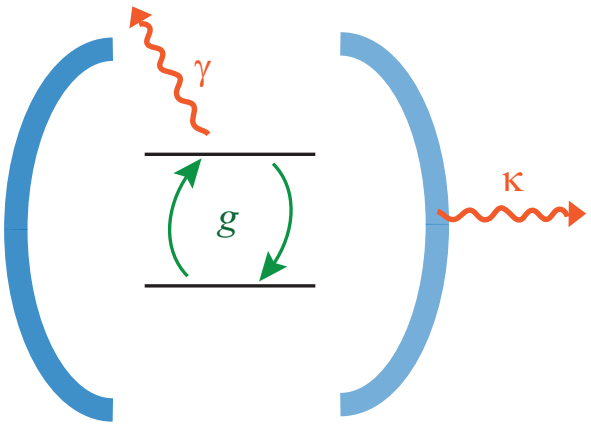

Figure 1: Schematic of atom-photon interaction in cavity QED

A frequent figure of merit that appears in the cavity QED worldview is the *co-operativity*

of the atom-photon interaction defined as

$$C = \frac{4g^2}{\kappa\gamma} \tag{1}$$

$C \gg 1$ dictates the regime for quantum coherent phenomena* and frequently, the co-operativity is the main parameter that determines the fidelity of quantum operations. It is important to note that the coherent rate g need not itself exceed the decoherence rates κ, γ but the co-operativity exceed 1. Typically, in the case of atom-cavity systems, one lies in the regime $\kappa \gg g \gg \gamma$. Ways to increase the co-operativity include increasing the Q factor of the cavity (lowering κ) and increasing g, which scales as $\mu/\sqrt{V}$, where μ is the dipole moment of the optical transition and V is the mode volume of the cavity. This has motivated the use of nanophotonic cavities in cavity QED with optical photons. In particular, photonic crystal cavities provide a high Q/V ratio and hence can offer high co-operativity when integrated with atoms or atom-like emitters.

0.3 Quantum acoustics

In parallel with the development of nanophotonic devices for strong atom-photon interactions, recent years have witnessed studies of nanomechanical devices at the single phonon level. In particular, the field of cavity optomechanics[20] has enabled parametric interaction between photons and phonons. This has allowed the use of laser light to cool nanomechanical oscillators to the ground state[21], prepare non-classical mechanical states[22] and entangle mechanical oscillators[23]. Nanomechanical resonators can be engineered to have extremely low dissipation rates[24], orders of magnitude below nanophotonic devices due to the difference in energy scale between optical photons and phonons, and the absence of loss from scattering into vacuum. Further, mechanical vibrations couple to a wide variety of quantum systems and can therefore serve as a low decoherence bus between them.

* If the environment for the cavity field is not at zero temperature, its thermal occupation n_{th} enters the denominator of C as $(n_{th} + 1)$

The vision for such hybrid quantum systems[11] is to couple disparate oscillators/qubits and carefully choose the underlying physical mechanisms to achieve high coherent interaction rates with low decoherence. Recent demonstrations of strong coupling between superconducting qubits and phonons[25,26] and the closely related push for phonon-mediated microwave to optical frequency conversion[27,28] are pertinent examples.

This context of hybrid quantum systems is another key motivation for the question of whether one can engineer a high co-operativity interface between color centers and phonons. Seminal experiments on coupling spins to mechanical oscillators relied on placing a cantilever with a magnetic tip close to the spin of interest[29,30,31]. The magnetic field gradient from the tip leads to an oscillating magnetic field that couples to the spin. An alternative approach would be to rely on coupling between the electronic levels of the defect center and phonons in the host crystal[32,33]. Microscopically, this coupling arises from deformation of the defect orbitals by strain in the crystal[34]. Phonons generate AC strain that can either lead to transitions between defect electronic levels or a periodic modulation of their energy. Absorption of acoustic energy by two level systems (TLS) possessing such an elastic dipole is a known limitation for the Q-factors of micromechanical resonators at low temperatures (T <1 K)[24,35]. Such phenomenological TLS have long been known to determine the low temperature acoustic and thermal properties of glasses[36] and also to have dipolar interactions among each other mediated by strain[37,38]. These observations provide additional impetus to explore strain as a means to couple color centers coherently to phonons, since color centers are microscopically well-understood defects that can be individually isolated. The recent development of single crystal diamond nanofabrication techniques[39,40,41,42,43] and subsequent realization of high Q mechanical oscillators in diamond[44,45,46] can further allow for coupling between single color centers and well-defined mechanical modes of these structures.

For strain-mediated coupling, the coupling rate between the acoustic TLS and a single phonon in the mechanical resonator is given by $g = d\epsilon_{ZPM}$, where ϵ_{ZPM} is the strain due

to zero point motion, and d is the strain susceptibility, an intrinsic property of the TLS. Engineering the mechanical mode to provide large ϵ_{ZPM} can provide large g. For instance, for a cantilever of width w, thickness t, and length l, we can use Euler-Bernoulli beam theory[47] to show that the zero point strain for the fundamental out-of-plane flexural mode of frequency $\omega_m \propto t/l^2$ scales as

$$\epsilon_{ZPM} \propto \frac{1}{\sqrt{l^3 t^2 w}} \tag{2}$$

This sharp inverse scaling of ϵ_{ZPM} with cantilever dimensions is analogous to the $1/\sqrt{V}$ scaling of g in cavity QED and highlights the benefit of working with small resonators. Over the course of this thesis, we will progress from MHz frequency cantilevers of $l \sim 10\mu$m in Chapter 1 to ∼GHz frequency phononic crystal resonators in Chapter 6 and reduce acoustic mode volume by two orders of magnitude. The other parameter of interest to increase g is the strain susceptibility d, which is analogous to the dipole moment of the atom in cavity QED. Over the course of this thesis, we will see an increase in d by four orders of magnitude by switching from the NV center ground state ($d \sim 10$ GHz/strain) in Chapter 1 to the SiV center ground state ($d \sim 100$ THz/strain) in Chapter 5.

0.4 Silicon vacancy center in diamond

The work in this thesis was carried at a time when a variety of defect centers were being explored after extensive studies on the diamond NV center. This includes defects in other host materials such as silicon carbide[48] and 2D materials[49]. In diamond, there has been a push towards inversion-symmetric defects that include the SiV and similar group IV emitters, the germanium vacancy (GeV) and tin vacancy (SnV). This has been largely motivated by their excellent optical properties for photonic quantum networks owing to their inversion symmetry. In particular, inversion symmetry sets the permanent dipole moment of the electronic states to zero, which makes them insensitive to electric fields to first or-

der[50,51,52,53]. This alleviates the sensitivity of the SiV to fluctuating electric fields in the solid state environment, especially in nanostructures, which are known to reduce the coherence of photons emitted by the NV center through spectral diffusion[54,55]. This has allowed the realization of high co-operativity atom-photon interactions with the SiV center in photonic crystal cavities[17,56].

Another distinctive feature of the negatively charged SiV is its thermally limited spin coherence time, T_2. In contrast with the NV center which can have T_2 of a millisecond at room temperature and nearly a second at 77 K[57], the SiV center has a T_2 of tens of nanoseconds at 4K[58,59,60] and tens of milliseconds at 100 mK[61]. This strong thermal dependence arises from the electronic structure of the SiV ground state which makes it very sensitive to phonons. This observation provides the first indication that the SiV may intrinsically act as a better spin-phonon interface than the NV. The microscopic details of this mechanism are the topic of Chapters 2 and 5. This also begs the question of whether the spin coherence can somehow be engineered to make the SiV a good quantum memory at 4K, which would be beneficial for photonic quantum networks. Chapter 4 provides a solution to this problem using strain control.

0.5 Thesis outline

Chapter 1 describes a preliminary experiment on NV centers in diamond cantilevers. Driven motion of the cantilevers is detected via microwave spectroscopy of the ground state electron spin. The results allowed us to assess experimental challenges for strong electron-phonon coupling with a defect spin. Our conclusions spurred two parallel efforts towards this goal: the investigation of a more strain sensitive defect spin, the SiV center and the development of optomechanical crystals in diamond.

Chapter 2 describes strain dependent optical spectroscopy of SiV centers. This work is enabled by the development of electromechanical actuation for the diamond cantilever

devices used in Chapter 1. Herein, we determine the strain response of the electronic levels of the SiV center and corroborate our observations with a group theoretical description of the defect.

Chapter 3 describes the application of strain tuning to alleviate inhomogeneity and spectral diffusion of optical transitions - two key technical challenges in solid state quantum optics, particularly with emitters in nanophotonic devices. By tuning and stabilizing the optical transitions of two SiV centers in a nanophotonic waveguide, we perform a quantum interference experiment on the emitted photons and observe the signature of an entangled, superradiant state. This addition of local tunability and spectral stabilization features compatible with nanophotonic devices advances the SiV center for applications in long distance photonic quantum networks.

Chapter 4 describes control of electron-phonon interactions in the SiV center ground state at 4 K. With strain control, we tune the energy of an acoustic phonon mediated transition in the ground state by two orders of magnitude from 50 GHz to over 1 THz. This capability allows us to probe and eventually suppress the effect of the thermal phonon bath on electron spin coherence.

Chapter 5 is a continuation of the strain dependent optical spectroscopy in Chapter 2 with an eye towards tailoring the SiV for strong electron-phonon coupling. Based on observations from static strain response, we establish schemes to couple the ground state electron spin to mechanical resonators of various frequencies.

Chapter 6 describes experiments towards a quantum coherent interface between the SiV electron spin and GHz frequency phonons confined in phononic crystal resonators. Optomechanical crystals with high quality factor (10^5) mechanical resonances at cryogenic temperatures are demonstrated in diamond.

Chapter 7 describes theoretical work exploring phonon-mediated interactions between multiple SiV electron spins. Specifically, we study the problem of quantum state transfer between SiV centers in a 1D acoustic waveguide.

Chapter 1

Nitrogen vacancy centers driven by diamond cantilevers

In this chapter, we study NV centers in diamond cantilevers with lateral dimensions of a few hundred nm and resonance frequencies around ∼1 MHz. The effect of driven cantilever motion on the ground state electron spin is observed in electron spin resonance (ESR) spectra and spin echo measurements. We infer a spin-phonon coupling strength of 1 Hz, a 10-100× enhancement over previous NV-strain coupling demonstrations at the time of this work due to the smaller mode volumes of our devices. While far from the strong coupling regime, the use of dense NV ensembles instead of a single NV can allow this system to reach high co-operativity.

1.1 Introduction

Strain mediated coupling between solid state emitters and mechanical resonators was first proposed[32], and subsequently demonstrated[62,63] with the electronic levels of quantum dots. Such a mechanical hybrid quantum system with negatively charged nitrogen vacancy (NV(-), hereafter referred to as NV) centers in diamond would benefit from their long spin coherence times[57]. It has been proposed that in the strong spin-phonon coupling

regime, phonons can be used to mediate quantum state transfer, and generate effective interactions between NV spins[10]. Strong coupling of an NV spin ensemble to a mechanical resonator can also be used to generate squeezed spin states[64], which can enable high sensitivity magnetometry[65].

Prior to this work, the effect of lattice strain on the NV ground state spin sublevels was used to couple NVs to mechanical modes of diamond cantilevers[66,67], and bulk acoustic wave resonators fabricated on diamond[68,69,70]. Strain-mediated coupling is experimentally elegant since its origin is intrinsic to a monolithic device, and it does not involve functionalization of mechanical resonators, or precise and stable positioning of magnetic tips very close to a diamond chip[29]. However, current demonstrations are far from the strong coupling regime due to the small spin-phonon coupling strength provided by strain from relatively large mechanical resonators. In this work, we present an important step towards strong coupling by incorporating photostable NVs in a diamond cantilever with nanoscale transverse dimensions, and demonstrate a single phonon coupling rate of ~ 2 Hz from dispersive interaction of NV spins with the resonator. This was a $\sim 10 - 100\times$ improvement over previous NV-strain coupling demonstrations. In our experiments, we first detect the effect of driven cantilever motion on NVs as a broadening of their electron spin resonance (ESR) signal, and through follow-up measurements, establish this to be strain-mediated coupling to the mechanical mode of interest. Subsequently, we use spin echo to probe the temporal dynamics of NVs in the cantilever, and precisely measure the spin-phonon coupling rate. In conclusion, we discuss options to further improve this coupling strength by $\sim 100\times$, and reach the strong coupling regime.

1.2 Device fabrication and experimental setup

Incorporating photostable NV centers close to surfaces[71,72], particularly in nanostructures with small transverse dimensions such as nanophotonic cavities[54,55], has been found to

be a considerably challenging task in recent years. To prevent charge state blinking and photo-ionization of NVs under optical excitation[73], high quality surfaces with low defect density, and appropriate surface termination are necessary. Recent advances in annealing and surface passivation procedures[74] have significantly improved the ability to retain photostable NV centers generated by ion implantation even after fabrication of nanostructures around them[75]. Using these techniques in combination with our angled reactive ion etching (RIE) fabrication scheme[41] (details discussed in Appendix A), we were able to generate photostable NVs in diamond nano-cantilevers with a triangular cross section (Fig. 1.1(a,b)). Previously, we have demonstrated high Q-factor mechanical modes (Q approaching 100,000) with frequencies ranging from <1 MHz to tens of MHz in cantilevers, and doubly clamped nanobeams fabricated using the same angled etching scheme[46].

Our measurements are carried out at high vacuum (10^{-5} torr), and room temperature in a vacuum chamber with a view port underneath a homebuilt scanning confocal microscope for addressing NV centers. Microwaves for ESR measurements are delivered with a wire bond positioned close to the devices of interest. The diamond chip is mounted on a piezo actuator for resonant actuation of cantilevers. Mechanical mode spectroscopy performed via optical interferometry[76] is used to characterize the modes of the cantilevers. For the experiments described in this paper, we used a triangular cross-section cantilever with w=580 nm, t=170 nm, and l=19 μm. The mechanical mode of interest (Fig. 1.1(c)) is the out-of-plane flexural mode, which was found to have a frequency, $\omega_m = 2\pi \times 937.2$ kHz, and a quality factor, $Q \sim 10,000$.

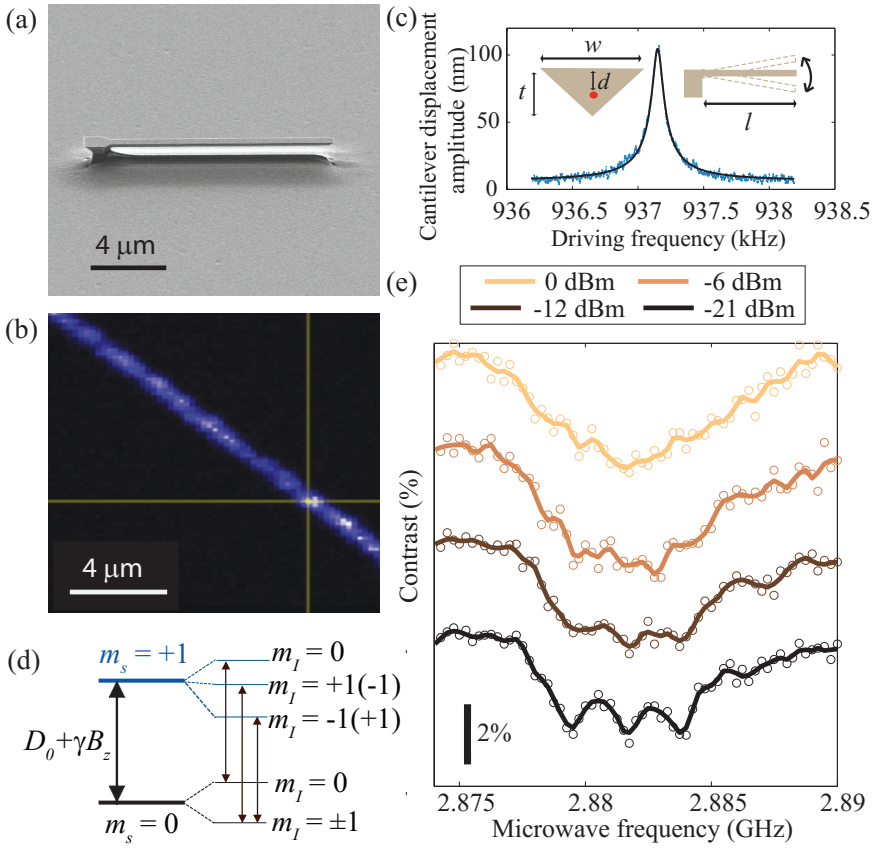

Figure 1.1: (a) Representative scanning electron microscope (SEM) image of the angle-etched diamond cantilevers used. (b) Representative confocal microscope scan of a section of the cantilever showing fluoresecence from NV centers. (c) Driven response of the fundamental out-of-plane flexural mode (right inset) of the triangular cross section (left inset) cantilevers studied in this work. For this particular device, we have w=580 nm, t=170 nm, and l=19 μm. The mode frequency is 937.2 kHz, and it has a Q-factor of 10,000. Measurements were taken in high vacuum (1e-5 torr) at room temperature. (d) Hyperfine structure of the $m_s = 0$ to $m_s = +1$ electron spin transition in the NV ground state indicating the three allowed microwave transitions. (e) AC strain induced broadening of the $m_s = 0$ to $m_s = +1$ hyperfine transitions near the clamp of the cantilever with gradually increasing mechanical amplitude. The mechanical mode is inertially driven at its resonance frequency with a piezo stack in all measurements. Open circles indicate measured data, and smoothed solid lines serve as a guide to the eye. Legend shows values of piezo drive power for each measurement. 0 dBm of drive power corresponds to an amplitude of 559 ± 2 nm at the tip of the cantilever.

1.3 Effect of strain on the NV ground state

The effect of lattice strain on the orbital singlet, spin triplet ($S = 1$) ground state manifold of the NV center has been described by the Hamiltonian[66,67,77,78,79] -

$$H = D_0 S_z^2 + \gamma \mathbf{S} \cdot \mathbf{B} + d_\parallel \epsilon_{zz} S_z^2 - \frac{d_\perp}{2} \left[\epsilon_+ S_+^2 + \epsilon_- S_-^2 \right] \tag{1.1}$$

Here S_i are the $S = 1$ Pauli spin operators. $D_0 = 2.87$ GHz is the zero-field splitting between $m_s = 0$ and $m_s = \pm 1$ levels due to spin-spin interaction, $\gamma = 2.8$ MHz/G is the gyromagnetic ratio for the NV ground state. At small B-fields ($\ll D_0/\gamma$), the spin quantization axis ($z-$axis in the above Hamiltonian) is the NV high symmetry axis. $d_\parallel$ and $d_\perp$ are respectively the strain susceptibilities for A_1 and E strain. ϵ_{ij} are strain tensor components defined in the coordinate basis of the NV[80], and $\epsilon_\pm = (\epsilon_{xx} - \epsilon_{yy}) \pm 2i\epsilon_{xy}$.

Physically, strain leads to shifting and mixing of electronic levels corresponding to different orbital occupation of the electrons (holes) on the defect molecule due to deformation of chemical bonds. Given that the NV ground state manifold corresponds to the occupation of two holes in the same singlet orbital state[80], the strain response of the spin sublevels must be due to an indirect mechanism, presently believed to be a perturbation to the spin-spin interaction between the two holes[78,79].

1.4 AC strain induced ESR broadening

The strain terms in Hamiltonian 1.1 lead to frequency shifts in the $m_s = \pm 1$ levels respectively given by

$$\Delta\omega_\pm = d_\parallel \epsilon_\parallel \pm \sqrt{(\gamma B_z)^2 + (d_\perp \epsilon_\perp)^2} \tag{1.2}$$

Here, $\epsilon_\perp$ denotes the magnitude of the E-strain vector and is given by $\sqrt{(\epsilon_{xx} - \epsilon_{yy})^2 + 4\epsilon_{xy}^2}$. Physically, Eq. 1.2 reveals that A_1-strain leads to a linear modification of the zero-field

splitting, while E-strain mixes the $m_s = \pm 1$ states, thereby causing a quadratically increasing splitting between them. In a mechanical resonator driven at the frequency ω_m, the local strain components $\epsilon_{\parallel}$ and $\epsilon_{\perp}$ oscillate at the frequency ω_m. The classical effect of driving the mechanical mode on the NV ground state is frequency modulation of the two transitions between $m_s = 0$ and $m_s = \pm 1$ levels. From the strain susceptibilities measured in[66], and finite element calculations on our structures, we anticipate a frequency modulation comparable to the ESR linewidth, when the mechanical mode is driven to an amplitude of ≈500 nm.

At the chosen nitrogen ion implantation density, we expect $\sim$ 10 NV centers within our confocal laser spot. ESR measurements are performed on such an NV ensemble at a fixed position in the cantilever, and simultaneously, the flexural mode shown in Fig. 1(c) is driven by supplying an RF voltage to the piezo actuator at the resonance frequency ω_m. A small static magnetic field B_z= 4 G is applied with a bar magnet placed outside the cryostat, and only the $m_s = 0$ to $m_s = +1$ transition is probed. The external magnetic field is aligned exactly vertically to ensure that all four NV classes experience the same projection B_z along their respective axes. The cantilever itself is fabricated such that its long axis is aligned to the $< 100 >$ crystal axis to within a few degrees as determined by electron back scatter diffraction (EBSD). As a result, all four NV classes are symmetrically aligned with respect to the dominant strain component of the flexural mode, which occurs along the cantilever long axis. Thus, at a given location in the cantilever, all four NV classes experience the same axial and transverse strain amplitudes, and hence experience identical transition frequency modulation. Low microwave power was used to prevent power broadening, and retain near native linewidths in the ESR.

Fig. 1.1(e) shows ESR spectra at the same location in the cantilever for progressively increasing mechanical amplitude. At the lowest piezo drive power of -21 dBm, we observe three dips spaced equally by 2.2 MHz corresponding to the hyperfine structure arising from interaction between the NV electron spin and the ^{14}N nuclear spin (Fig. 1.1(d)).

This was found to be identical to the ESR spectrum with no piezo drive (not shown). For each of the hyperfine transitions, we measure a linewidth of ≈2 MHz. As the piezo drive power is increased to -12 dBm, we observe a broadening of the hyperfine features to the point where the hyperfine structure is barely resolvable. At -6 dBm, the hyperfine structure is washed out, and at 0 dBm, the overall ESR dip is even broader. Such broadening of the ESR signal with progressively larger mechanical amplitude is expected, since the measurement sequence involves dwelling at each microwave frequency sample for many ($> 10^6$) cycles of the mechanical oscillation period. As a result, we would expect to average over the AC modulation of the microwave transition, and detect an overall broadening determined by the modulation amplitude.

To verify that the ESR broadening arises from the mechanical mode, we perform the same measurement at a fixed drive power of -12 dBm, and multiple drive frequencies around resonance. The slight asymmetry in the driven mechanical response (Fig. 1.2(a)) can be attributed to the onset of a Duffing-type nonlinearity at this drive power. When driven far off the mechanical resonance as in points 1 and 5 in Fig. 1.2(b), the ESR spectrum retains three clear hyperfine dips with linewidths close to the native linewidth. At smaller detunings as in points 2 and 4 in 1.2(b), we observe a broadening of the individual hyperfine features. When driven exactly on resonance as in point 3 in Fig. 1.2(d), the hyperfine features are on the verge of being washed out. Thus, the ESR broadening effect follows the frequency response of the mechanical mode. To further confirm that this is a strain-induced effect, we repeat the measurement at multiple points along the length of the cantilever for a fixed piezo drive power of -6 dBm. From the strain profile of the flexural mode (Fig. 1.2(c)), we expect a roughly linear variation in AC strain amplitude from its maximum value near the clamp of the cantilever to zero at the tip of the cantilever. This effect is observed in the form of ESR broadening for NVs near the clamp, and retention of native linewidths for NVs at the tip (Fig. 1.2(c)).

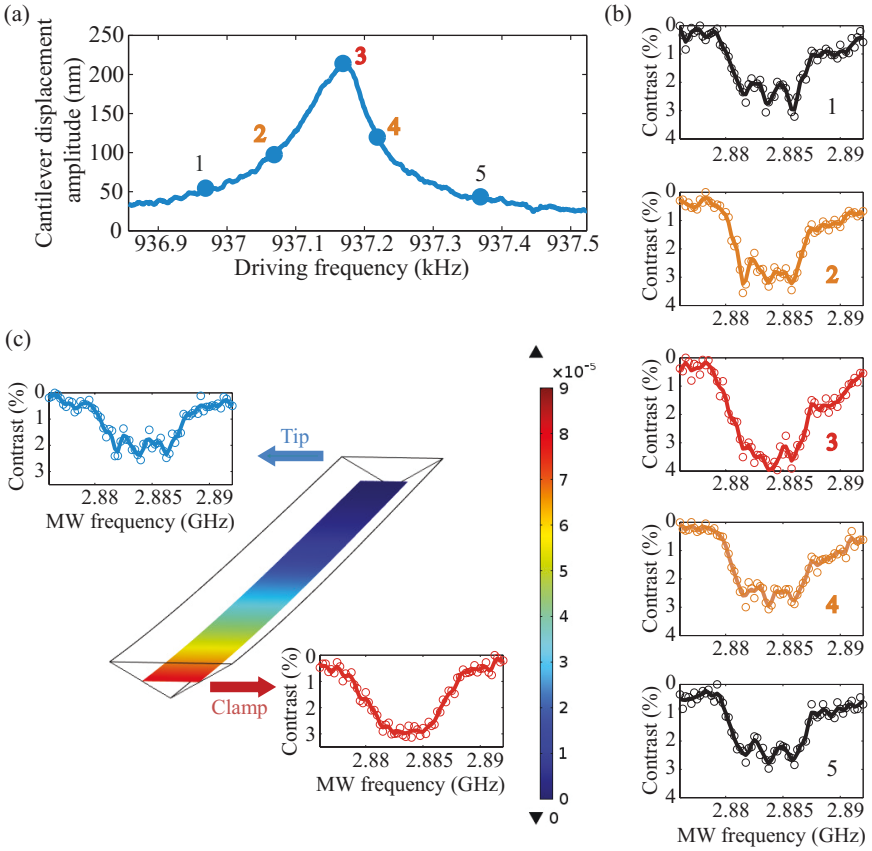

Figure 1.2: (a) Driven response of the cantilever at a piezo drive power of -12 dBm. The drive frequencies used for frequency dependent broadening measurements are indicated with numbers 1-5. (b) ESR spectra at the same location in the cantilever at mechanical drive frequencies 1-5 indicated in (a). (c) ESR spectra at the tip and clamp of the cantilever for -6 dBm drive power. Strain profile of the mechanical mode from an FEM simulation for the corresponding displacement amplitude is also shown. Open circles in each ESR spectrum are measured data, and smoothed lines serve as a guide to the eye

1.5 Temporal dynamics of the mechanically driven spin

The ESR broadening measurements in Figs. 1.1(e) and Fig. 1.2 provide strong evidence of strain from the driven mechanical mode coupling to the NV spin. From the washing out of hyperfine structure in the measurements, we can deduce driven coupling rates of the order of the hyperfine splitting (2.2 MHz). In order to probe the temporal dynamics of the NV spin due to mechanical motion, and precisely measure the coupling strength, we employ spin echo measurements. It has been shown in previous demonstrations that the two distinct modes of level shifts generated by axial and transverse strain can be used to achieve dispersive[66] and resonant interactions[68,81] of the spin with mechanical motion, respectively. In our work, the frequency of our mechanical mode ($\approx$1 MHz) is smaller than the ESR linewidth, and we will focus on the dispersive regime provided by axial strain. We apply a moderate static magnetic field, and suppress the effect of transverse strain to first order as evinced by Eq. 1.2. In this regime, if we work with the effective qubit defined by the $m_s = 0$ and $m_s = +1$ levels, driven motion of the mechanical resonator can modulate the phase of our effective qubit at the frequency ω_m, analogous to an AC magnetic field. This is described by the time dependent Hamiltonian

$$H_{int}(t) = 2\pi G \cos\left(\omega_m t + \phi\right) \sigma_z \tag{1.3}$$

Here $G = d_{\parallel}\epsilon_{zz}$ is the AC strain coupling rate from the driven motion, ϕ is an arbitrary phase offset, and σ_z is the corresponding $S = 1/2$ Pauli spin operator.

In our spin-echo measurements, we apply an external static magnetic field B_z= 27 G. As in the case of ESR measurements, the magnetic field is aligned to ensure equal Zeeman splittings for all four NV orientations. Our experimental sequence is shown in Fig. 1.3(a), wherein the piezo drive signal, and hence the strain field, has an arbitrary phase ϕ with respect to the microwave pulses that varies over multiple iterations of the sequence. The spin echo signal obtained from this measurement (Fig. 1.3(b)) at a piezo drive power of 0

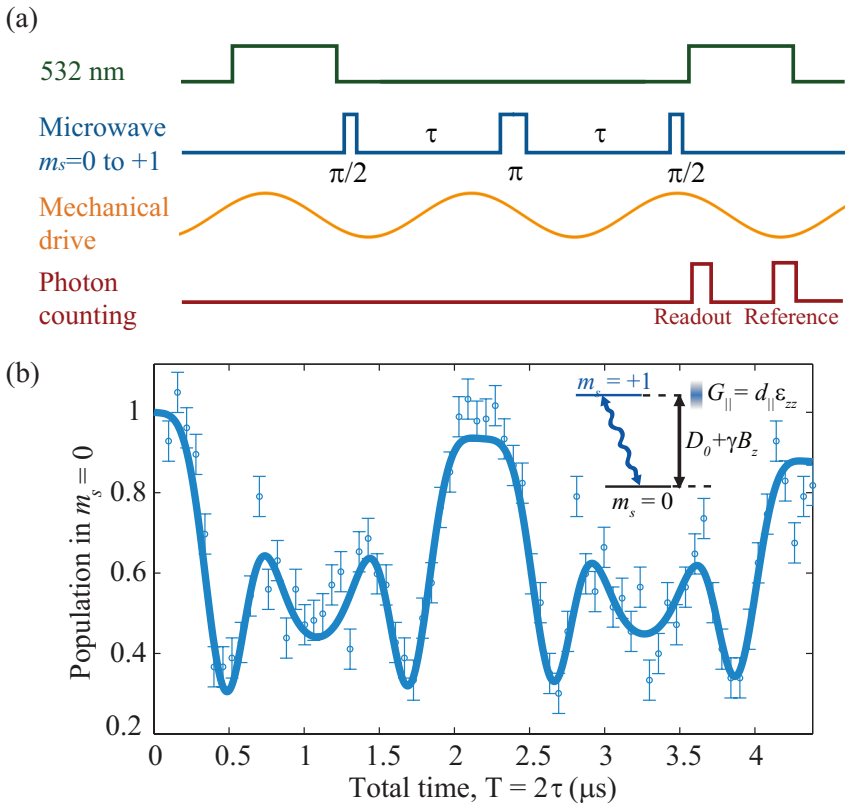

Figure 1.3: (a) Experimental pulse sequence for spin echo measurement of dispersive spin-cantilever interaction due to axial strain (b) Spin echo signal from NVs in the cantilever at a piezo drive power of 0 dBm (tip amplitude of 559±2 nm) for the mode at $\omega_m = 923.4$ kHz, showing two periods of the modulation due to axial strain coupling. The solid line is a fit to Eq. 1.4. Vertical error bars correspond to photon shot noise in the measurement. Inset shows schematic of dispersive interaction between the qubit and mechanical mode due to axial strain.

dBm shows a periodicity corresponding to twice the time period of the mechanical mode. The theoretically expected spin echo signal in this measurement has the form of a zero order Bessel function with a periodic argument[29,66].

$$p(2\tau) = \frac{1}{2}\left[1 + e^{-(2\tau/T_2)^3} J_0\left(\frac{8\pi G}{\omega_m}\sin^2\left(\frac{\omega_m \tau}{4}\right)\right)\right] \tag{1.4}$$

The exponential damping term multiplying the periodic function corresponds to dephasing of the NV electron spin due to interactions with the surrounding ^{13}C nuclear spin bath in diamond, and T_2 is the dephasing time[82]. In our experiments, $T_2 \gg$ the mechanical oscillation period ($2\pi/\omega_m$), and the effect of spin decoherence is relatively small. A fit to expression 1.4 yields $\omega_m = 2\pi \times 918.7 \pm 5.6$ kHz, which is in reasonable agreement with the driving frequency of 923.4 kHz used in the experiment. The extracted driven coupling rate $G = 2.10 \pm 0.07$ MHz is of the order of the hyperfine splitting as observed in our ESR broadening measurements.

Finally, we performed spin echo measurements at the same location on the cantilever for varying piezo drive powers (Fig. 1.4(a)). The no-drive spin echo signal (not shown) is flat, indicating that this measurement is not sensitive to the thermal motion of the cantilever mode (estimated to have an amplitude of 0.53 nm). As the cantilever is driven, the spin echo signal begins to show a dip when the evolution time 2τ equals the mechanical oscillation period ($2\pi/\omega_m$). At larger amplitudes, the spin precesses by more than one full rotation on the equator of the Bloch sphere, and we observe higher order fringes within one period of the signal. These drive-power dependent measurements further allow us to verify that the axial strain coupling is linear in the displacement amplitude (Fig. 1.4(b)). From the linear fit, we infer a displacement sensitivity $dG/dx = 4.02 \pm 0.40$ kHz/nm. By estimating the zero point motion of the mode from its effective mass, this displacement sensitivity yields a single phonon coupling strength, $g = 1.84 \pm 0.18$ Hz for an NV at the clamp of this cantilever. Compared with previous demonstrations of NV-strain coupling, this was about two orders of magnitude larger than that measured in Ref.[66], and an order of magnitude

larger than that in Ref.[67].

1.6 Outlook

In conclusion, we demonstrate nanoscale diamond cantilevers for strain-mediated coupling of NV spins to mechanical resonators. The relatively small dimensions of our devices offer a significant improvement in the single phonon coupling strength compared to previous work with mechanical modes at similar frequencies. Shorter cantilevers will boost g even further according to the scaling in Eq. 2. This will also increase the mechanical frequencies, and allow operation in the sideband resolved regime with access to the resonant spin-phonon interaction provided by E-strain[68,81]. Nanostructures that allow strong coupling have mechanical frequencies in the few hundreds of MHz range. Dynamic actuation and transduction of single crystal diamond resonators up to frequencies of 50 MHz was achieved with dielectric gradient forces[83], and up to 9 GHz was achieved by using cavity optomechanics[84]. Given these developments, we anticipate that the major engineering challenge for strain-mediated strong spin-phonon coupling will be the ability to maintain photostable NVs in nanostructures with extremely small widths (the current state-of-the-art being nanobeams with $w \approx 200$ nm[75]). Another challenge is the demand for high Q-factors in the $10^5 - 10^6$ range from small resonators, which are usually challenging to engineer for high Q[35].

However, these device engineering requirements can be less demanding for magnetometry applications that can benefit from an NV ensemble coupled to a mechanical resonator[64]. In particular, collective enhancement from a dense spin ensemble can boost the co-operativity by a factor of the number of spins N[85], allowing one to work with device dimensions more favorable for NV photostability and high mechanical Q-factors. Alternatively, since the framework of strain coupling outlined in this work is fairly general, the same devices may be used, but with a different qubit, whose energy levels have a larger strain response. Po-

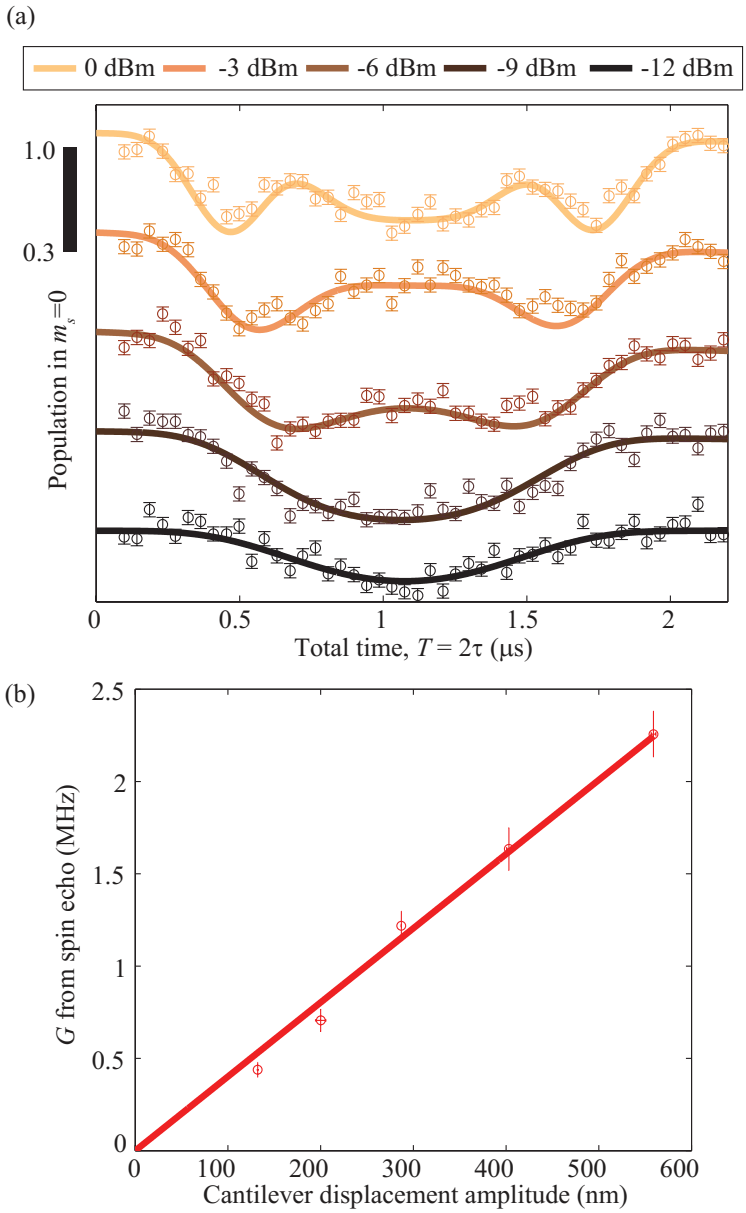

Figure 1.4: (a) Spin echo at the same location in the cantilever for varying piezo drive powers, offset along y-axis. One period of the signal is plotted in each case. Solid lines are fits to the zero order Bessel function form indicated in the text, and vertical error bars correspond to photon shot noise. The scale bar on the side is a guide for the y-axis indicating maximum (1.0) and minimum (0.3) possible population in $m_s = 0$ as dictated by Eq. 1.4. The legend on right side indicates the piezo drive powers used for each measurement. (b) Variation of driven spin-phonon coupling rate due to axial strain (G) with the calibrated displacement amplitude of the mechanical mode. The five data points correspond to the piezo drive powers used in plot (a) in increasing order. Vertical error bars correspond to the error in each G estimate from fitting to the spin echo function given by Eq. 1.4. Solid line is a linear fit, which yields $dG/dx = 4.02 \pm 0.40$ kHz/nm.

tential candidates include the NV center excited electronic state[86,87], and the orbital ground states of the silicon vacancy (SiV) center[88], both of which have 4-5 orders of magnitude larger strain susceptibility than the NV ground state spin sublevels.

Chapter 2

Strain tuning of the silicon vacancy center

In this chapter, we describe an experiment to control the electronic structure of the silicon-vacancy (SiV) color-center in diamond by changing its static strain environment with a nano-electro-mechanical system. We achieve deterministic and local tuning of SiV optical and spin transition frequencies over a wide range, an essential ingredient for multi-qubit photonic quantum networks. In the process, we infer the strain Hamiltonian of the SiV revealing large strain susceptibilities of order 1 PHz/strain for the electronic orbital states.

2.1 Introduction

Solid state emitters such as color-centers and epitaxially grown quantum dots provide both electronic spin qubits and coherent optical transitions, and are optically accessible quantum memories. They can therefore serve as building blocks of a quantum network composed of nodes in which information is stored in spin qubits and interactions between nodes are mediated by photons[9,3,89,90]. However, due to the effects of their complex solid state environment, most quantum emitters do not simultaneously provide long coherence time for the memory, and favorable optical properties such as bright, spectrally stable

emission. The negatively charged silicon vacancy center in diamond (SiV^-, hereafter simply referred to as SiV) has been recently identified as a system that can overcome these limitations, since it provides excellent optical and spin properties simultaneously. Its dominant zero-phonon-line (ZPL) emission and stable optical transition frequencies resulting from its inversion symmetry[50,51,52] have recently been used to realize single-photon switching[56] and a fibre-coupled coherent single-photon source[19] in a nanophotonic platform. Further, recent demonstrations of microwave[60] and all-optical[91] control of its electronic spin, as well as long ($\sim$10 ms) spin coherence times at mK temperatures[61], when electron-phonon processes in the center are suppressed,[59,60] make the SiV a good memory qubit. Scaling up these demonstrations to multi-qubit networks requires local tunability of individual emitters, as well as the realization of strong interactions between them. In this work, we control local strain in the SiV environment using a nano-electro-mechanical system (NEMS), and show wide tunability for both optical and spin transition frequencies. In particular, we demonstrate hundreds of GHz of optical tuning, sufficient to achieve spectrally identical emitters for photon-mediated entanglement[9,3]. Further, we characterize the strain Hamiltonian of the SiV and measure high strain susceptibilities for both the electronic and spin levels. Building on this strain response, we discuss schemes to realize strong coupling of the SiV spin to coherent phonons in GHz frequency nanomechanical resonators in Chapters 5, 7.

2.2 Strain response of optical transitions

The SiV center is an interstitial point defect in which a silicon atom is positioned midway between two adjacent missing carbon atoms in the diamond lattice as depicted in the inset of Fig. 2.1(a). Its electronic level structure at zero strain is shown in Fig. 2.1(a). The optical ground state (GS) and excited state (ES) each contain two distinct electronic configurations shown by the bold horizontal lines. Physically, each of the two branches in the

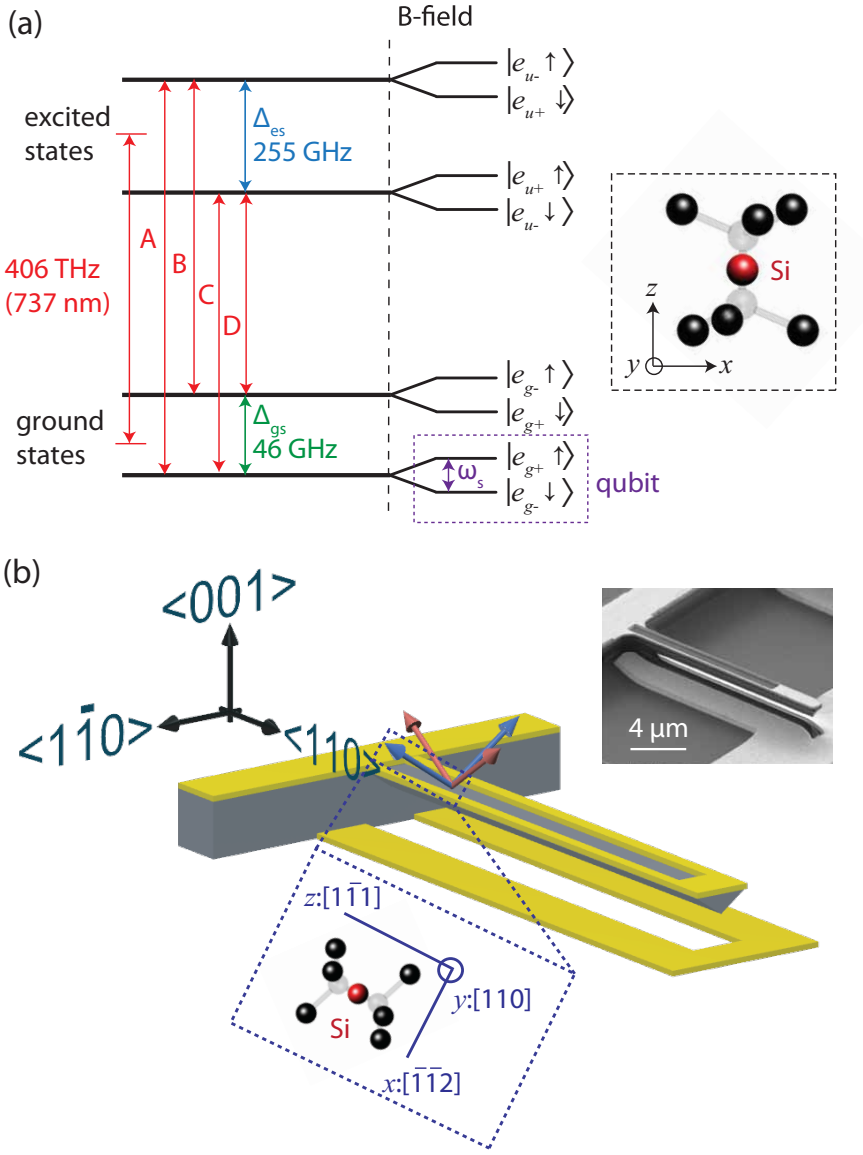

Figure 2.1: (a) Electronic level structure of the SiV center (molecular structure shown in inset) at zero strain showing ground and excited manifolds with spin-orbit eigenstates. The four optical transitions A, B, C, and D at zero magnetic field, and splittings between orbital branches in the ground state (GS) and excited state (ES), $\Delta_{\rm gs}$ and $\Delta_{\rm es}$ respectively are indicated. In the presence of a magnetic field, each orbital branch splits into two Zeeman sublevels. A long-lived qubit can be defined with the sublevels of the lower orbital branch in the GS. (b) Schematic of the diamond cantilever device and surrounding electrodes. Diamond crystal axes relative to the cantilever orientation are shown. Four possible orientations of the highest symmetry axis of an SiV are indicated by the four arrows above the cantilever. Under application of strain, these can be grouped into axial (red) and transverse (blue) orientations. Molecular structure of a transverse-orientation SiV as viewed in the plane normal to the cantilever axis is shown below, and crystal axes that define the internal co-ordinate frame of the color center are indicated. The z-axis is the highest symmetry axis, which defines the orientation of the SiV. (c) SEM image of diamond cantilever NEMS device.

GS and ES corresponds to the occupation of a specific E-symmetry orbital by an unpaired hole.[53] At zero magnetic field, the degeneracy of these orbitals is broken by spin-orbit (SO) coupling leading to frequency splittings $\Delta_{\text{gs}} = 46$ GHz, and $\Delta_{\text{es}} = 255$ GHz respectively. Due to inversion symmetry of the defect about the Si atom, the wavefunctions of these orbitals can be classified according to their parity with respect to this inversion center.[50,53] Thus, the GS configurations correspond to the presence of the unpaired hole in one of the even-parity orbitals e_{g+}, e_{g-}, while the ES configurations have this hole in one of the odd-parity orbitals e_{u+}, e_{u-}. Here the subscripts g, u refer to even (*gerade*) and odd (*ungerade*) parity respectively, and $+$, $-$ refer to the orbital angular momentum projecton L_z. This specific level structure gives rise to four distinct optical transitions in the ZPL indicated by A, B, C, D in Fig. 2.1(a). Upon application of a magnetic field, degeneracy between the SO eigenstates is further broken to reveal two sub-levels within each orbital branch corresponding to different spin states of the unpaired hole ($S = 1/2$). In this manner, a qubit can be defined on the two sublevels of the lowest orbital branch in the ground state.

To control local strain in the environment of the SiV center, we use a diamond cantilever, shown schematically in Fig. 2.1(b) and in a scanning electron microscope (SEM) image in Fig. 2.1(c). Electrodes are fabricated, one on top of the cantilever, and another on the substrate below the cantilever to form a capacitive actuator. By applying a specific DC voltage to these electrodes, we can deflect the cantilever to achieve a desired amount of static strain at the SiV site. The fabrication procedure based on angled etching of diamond[92,41] and device design are discussed in more detail in Chapter 4 and Appendix C. The diamond sample with cantilever NEMS is maintained at 4 K in a Janis ST-500 continuous-flow liquid helium cryostat. We perform optical spectroscopy on SiVs inside the cantilever by resonantly exciting the transitions shown in Fig. 2.1(a) with a tunable laser, and collecting fluorescence in the phonon sideband. Mapping the response of these transitions as a function of voltage applied to the device allows us to study the strain response

of the SiV electronic structure.

The diamond samples used in our study have a [001]-oriented top surface, and the long axis of the cantilever is oriented along the [110] direction. There are four possible equivalent orientations of SiVs - [111], [$\bar{1}\bar{1}$1], [1$\bar{1}$1], [$\bar{1}$11] - in a diamond crystal, indicated by the four arrows above the cantilever in Fig. 2.1(b). Since the cantilever primarily achieves uniaxial strain directed along [110], this breaks the equivalence of the four orientations, and leads to two classes indicated by the blue and red colored arrows in Fig. 2.1(b). The blue SiVs, oriented perpendicularly to the cantilever long-axis, predominantly experience uniaxial strain along their internal y-axis (see inset of Fig. 2.1(b)). On the other hand, the red SiVs are not orthogonal to the cantilever long-axis, and experience a non-trivial strain tensor, which includes significant strain along their internal z-axis. For simplicity, we refer to blue SiVs as 'transverse-orientation' SiVs, and red SiVs as 'axial-orientation' SiVs. This nomenclature is used with the understanding that it is specific to the situation of predominantly [110] uniaxial strain applied with our cantilevers.

Two distinct strain-tuning behaviors correlated with SiV orientation are observed as shown in Fig. 2.2. Orientation of SiVs in the cantilever is inferred from polarization-dependence of their optical transitions at zero strain.[53] With gradually increasing strain, transverse-orientation SiVs show an increasing separation between the A and D transitions with relatively small shifts in the B and C transitions as seen in Fig. 2.2(a). This behavior has been observed on a previous experiment with an ensemble of SiVs.[88] On the other hand, axial-orientation SiVs show a more complex tuning behavior in which all transitions shift as seen in Fig. 2.2(b).

In the context of photon-mediated entanglement of emitters, typically, photons emitted in the C line, the brightest and narrowest linewidth transition are of interest[56]. Upon comparing Figs. 2.2(a) and (b), we note that this transition is significantly more responsive for axial-orientation SiVs. Particularly in Fig. 2.2(b), we achieve tuning of the C transition wavelength by 0.3 nm (150 GHz), approximately 10 times the typical inhomogene-

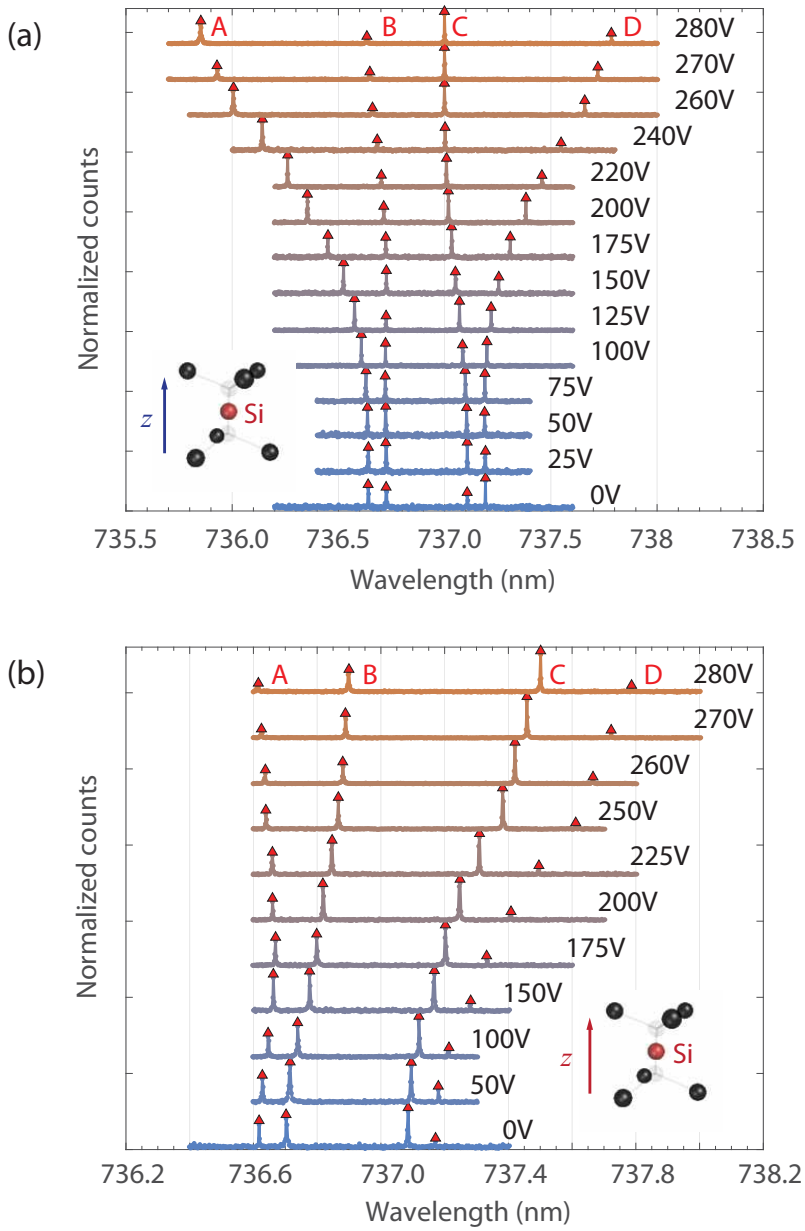

Figure 2.2: Tuning of optical transitions of (a) transverse-orientation SiV (blue in Fig. 1(b)), and (b) axial orientation SiV (red in Fig. 1(b)). Voltage applied to the device is indicated next to each spectrum.

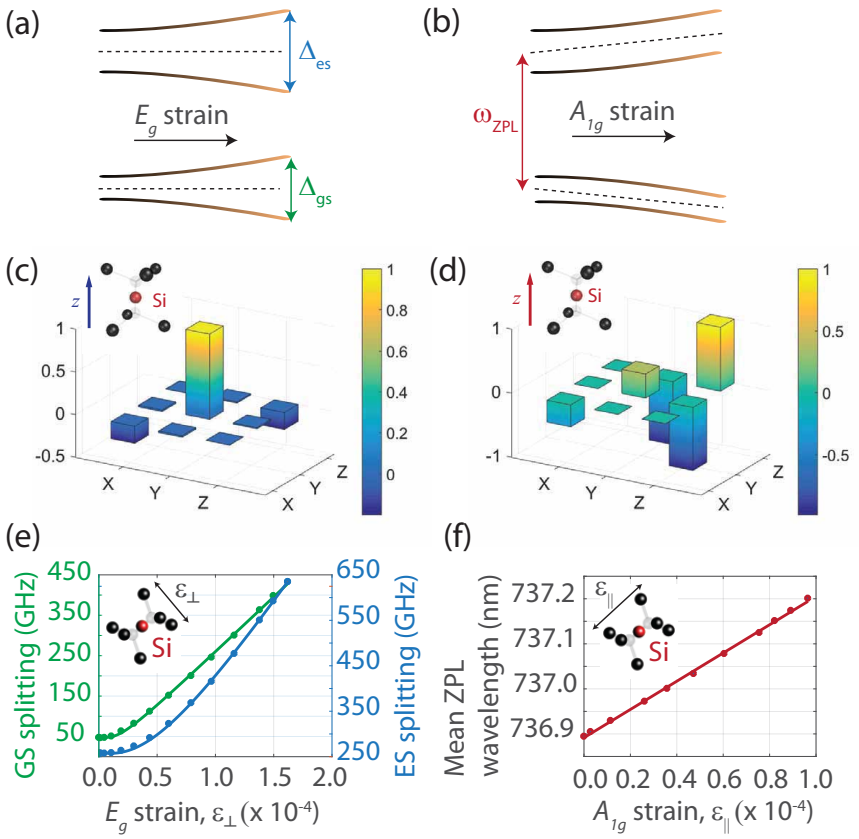

Figure 2.3: (a) Dominant effect of E_g-strain on the electronic levels of the SiV. (b) Dominant effect of A_{1g}-strain on the electronic levels of the SiV. (c) Normalized strain-tensor components experienced by transverse-orientation SiV (red in Fig. 1(b)), and (d) axial orientation SiV (blue in Fig. 1(b)) in the SiV co-ordinate frame upon deflection of the cantilever. (e) Variation in orbital splittings within GS (green dots) and ES (blue dots) upon application of E_g-strain. The x-axis refers to the magnitude of E_g-strain, which is approximately given by $|\epsilon_{xx} - \epsilon_{yy}|$ for our device. Data points are extracted from the optical spectra in Fig. 2(a). Solid curves are fits to theory in text. (f) Tuning of mean optical wavelength with A_{1g} strain due to the uniaxial component ϵ_{zz}. Data points are extracted from the optical spectra in Fig. 2(b). Solid line is a linear fit as predicted by theory in text. Appendix B.2 details the fitting procedure used in panels (e) and (f).

ity in optical transition frequencies of SiV centers in bulk diamond[51,93], and 5 times that of the typical inhomogeneity in nanofabricated structures (Fig. 3.2). Thus, NEMS-based strain control can be used to deterministically tune multiple on-chip or distant emitters to a set optical wavelength. Integration of this NEMS-based strain-tuning with existing diamond nanophotonic devices is particularly appealing. Besides static tuning of emitters, dynamic control of the voltage applied to the NEMS can be used to counteract slow spectral diffusion, and stabilize optical transition frequencies[94]. Both these ideas are essential for the observation of quantum interference between two SiVs in Chapter 3.

2.3 Effect of strain on electronic levels

Following previous work on point defects,[53,80,95] we employ group theory to explain the effect of strain on the SiV electronic levels, and extract the susceptibilities for various strain components. In this section, we describe the strain Hamiltonian of the SiV center, and summarize the physical effects of various modes of deformation on the orbital wavefunctions. A more detailed group-theoretic discussion of the results in this section is provided in Appendix B.1 and in Ref.[53]. Based on the symmetries of the orbital wavefunctions, it can be shown that the effects of strain on the GS (e_g) and ES (e_u) manifolds are independent and identical in form. For either manifold, the strain Hamiltonian in the basis of $\{|e_x\downarrow\rangle, |e_x\uparrow\rangle, |e_y\downarrow\rangle, |e_y\uparrow\rangle\}$ states (pure orbitals unmixed by SO coupling as defined in Ref.[53]) is given by

$$\mathbb{H}^{\text{strain}} = \begin{bmatrix} \epsilon_{A_{1g}} - \epsilon_{E_{gx}} & \epsilon_{E_{gy}} \\ \epsilon_{E_{gy}} & \epsilon_{A_{1g}} + \epsilon_{E_{gx}} \end{bmatrix} \otimes \mathbb{I}_2 \tag{2.1}$$

The spin part of the wavefunction is associated with an identity matrix in Eq. (2.1) because lattice deformation predominantly perturbs the Coulomb energy of the orbitals, which is independent of the spin character. Each ϵ_r is a linear combination of strain components ϵ_{ij}, and corresponds to specific symmetries indicated by the subscript r.

$$\begin{aligned} \epsilon_{A_{1g}} &= t_\perp(\epsilon_{xx} + \epsilon_{yy}) + t_\parallel \epsilon_{zz} \\ \epsilon_{E_{gx}} &= d(\epsilon_{xx} - \epsilon_{yy}) + f\epsilon_{zx} \\ \epsilon_{E_{gy}} &= -2d\epsilon_{xy} + f\epsilon_{yz} \end{aligned} \tag{2.2}$$

Here $t_\perp, t_\parallel, d, f$ are the four strain-susceptibility parameters that completely describe the strain-response of the $\{|e_x\rangle, |e_y\rangle\}$ states. These parameters have different numerical values in the GS and ES manifolds. From the Hamiltonian 2.1, we see that E_{gx} and E_{gy} strain

cause mixing and relative shifts between orbitals, and modify the orbital splittings within the GS and ES manifolds as depicted in Fig. 2.3(a). On the other hand, A_{1g} strain leads to a uniform or common-mode shift of the GS and ES manifolds, and only shifts the mean ZPL frequency as depicted in Fig. 2.3(b).

By decomposing the strain applied in our experiment into A_{1g} and E_g components, we can confirm the observations on tuning of transverse- and axial-orientation SiVs in Fig. 2.2. Strain tensors for transverse- and axial-orientations of emitters obtained from finite element method (FEM) simulations are plotted in Figs. 2.3(c), (d) respectively. As expected from the cantilever geometry in Fig. 2.1(a), transverse-orientation SiVs predominantly experience ϵ_{yy} and hence an E_g deformation. The E_g-strain response predicted in Fig. 2.3(a) leads to the strain-tuning of mainly A and D transitions seen in Fig. 2.2(a). This mode of strain is also responsible for the resonant interaction of GS and ES orbitals with phonons, which will be the topic of Chapter 4. On the other hand, axial-orientation SiVs experience both ϵ_{zz} and ϵ_{yz} as shown in Fig. 2.3(d), which leads to simultaneous E_g and A_{1g} deformations. Indeed, a combination of the strain responses in Figs. 2.3(a), (b) qualitatively explains the strain-tuning behavior of the transitions in Fig. 2.2(b).

2.4 Estimation of strain susceptibilities

We now quantitatively fit the results in Fig. 2.2 with the above strain response model. Adding SO coupling ($\mathbb{H}^{\mathrm{SO}} = -\lambda_{\mathrm{SO}} L_z S_z$) to the strain Hamiltonian in Eq. 2.1, we get the following total Hamiltonian in the $\{|e_x\downarrow\rangle, |e_x\uparrow\rangle, |e_y\downarrow\rangle, |e_y\uparrow\rangle\}$ basis.[53]

$$\mathbb{H}^{\mathrm{total}} = \begin{bmatrix} \epsilon_{A_{1g}} - \epsilon_{E_{gx}} & 0 & \epsilon_{E_{gy}} - i\lambda_{\mathrm{SO}}/2 & 0 \\ 0 & \epsilon_{A_{1g}} - \epsilon_{E_{gx}} & 0 & \epsilon_{E_{gy}} + i\lambda_{\mathrm{SO}}/2 \\ \epsilon_{E_{gy}} + i\lambda_{\mathrm{SO}}/2 & 0 & \epsilon_{A_{1g}} + \epsilon_{E_{gx}} & 0 \\ 0 & \epsilon_{E_{gy}} - i\lambda_{\mathrm{SO}}/2 & 0 & \epsilon_{A_{1g}} + \epsilon_{E_{gx}} \end{bmatrix} \tag{2.3}$$

Here, $\lambda_{\rm SO}$ is the SO coupling strength within each manifold: 46 GHz for the GS, and 255 GHz for the ES. Diagonalization of this Hamiltonian gives two distinct eigenvalues

$$\begin{aligned} E_1 &= \alpha - \frac{1}{2}\sqrt{\lambda_{\rm SO}^2 + 4(\epsilon_{E_{gx}}^2 + \epsilon_{E_{gy}}^2)} \\ E_2 &= \alpha + \frac{1}{2}\sqrt{\lambda_{\rm SO}^2 + 4(\epsilon_{E_{gx}}^2 + \epsilon_{E_{gy}}^2)} \end{aligned} \tag{2.4}$$

Each of these corresponds to doubly spin-degenerate eigenstates in the absence of an external magnetic field. Noting that Eqs. (2.4) are valid within both GS and ES manifolds, but with different strain susceptibilities, we obtain the following quantities that can be directly extracted from the optical spectra in Fig. 2.2.

$$\Delta_{\rm ZPL} = \Delta_{\rm ZPL,0} + \left(t_{\parallel,\rm es} - t_{\parallel,\rm gs}\right)\epsilon_{zz} + \left(t_{\perp,\rm es} - t_{\perp,\rm gs}\right)(\epsilon_{xx} + \epsilon_{yy}) \tag{2.5}$$

$$\Delta_{\rm gs} = \sqrt{\lambda_{\rm SO,gs}^2 + 4\left[d_{\rm gs}(\epsilon_{xx} - \epsilon_{yy}) + f_{\rm gs}\epsilon_{yz}\right]^2 + 4\left[-2d_{\rm gs}\epsilon_{xy} + f_{\rm gs}\epsilon_{zx}\right]^2} \tag{2.6}$$

$$\Delta_{\rm es} = \sqrt{\lambda_{\rm SO,es}^2 + 4\left[d_{\rm es}(\epsilon_{xx} - \epsilon_{yy}) + f_{\rm es}\epsilon_{yz}\right]^2 + 4\left[-2d_{\rm es}\epsilon_{xy} + f_{\rm es}\epsilon_{zx}\right]^2} \tag{2.7}$$

The quantities on the left hand side, $\Delta_{\rm ZPL}$ the mean ZPL frequency, and $\Delta_{\rm gs}$, $\Delta_{\rm es}$ the GS and ES orbital splittings are written as a function of strain. The subscripts 'gs' and 'es' for the various strain susceptibility parameters refer to the values of the respective parameters in the GS and ES manifolds respectively. $\Delta_{\rm ZPL,0}$ is the mean ZPL frequency at zero strain. Extracting all three frequencies in Eqs. (2.5-2.7) as a function of strain from the optical spectra measured in Fig. 2.2, we fit them to the above model in Figs. 2.3(e), (f), and estimate the strain-susceptibilities. The fitting procedure described in detail in Appendix B.2 gives us

$$
\begin{aligned}
\left(t_{\parallel,\mathrm{es}} - t_{\parallel,\mathrm{gs}}\right) &= -1.7 \pm 0.1\,\mathrm{PHz/strain} \\
\left(t_{\perp,\mathrm{es}} - t_{\perp,\mathrm{gs}}\right) &= 0.078 \pm 0.009\,\mathrm{PHz/strain} \\
d_{\mathrm{gs}} &= 1.3 \pm 0.1\,\mathrm{PHz/strain} \\
d_{\mathrm{es}} &= 1.8 \pm 0.2\,\mathrm{PHz/strain} \\
f_{\mathrm{gs}} &= -1.7 \pm 0.1\,\mathrm{PHz/strain} \\
f_{\mathrm{es}} &= -3.4 \pm 0.3\,\mathrm{PHz/strain}
\end{aligned} \tag{2.8}
$$

We will continue our study of the SiV strain response by considering the case with a nonzero magnetic field in Chapter 5. The following two chapters will apply the tools developed so far to tune SiV centers on a chip into optical resonance and to control the phonon-limited spin coherence of SiV centers at 4 K.

Chapter 3

Quantum interference between strain tuned silicon vacancy centers

Photon-mediated coupling between distant matter qubits[96,97,98] may enable secure communication over long distances, the implementation of distributed quantum computing schemes, and the exploration of new regimes of many-body quantum dynamics[5,9]. Solid-state quantum emitters coupled to nanophotonic devices represent a promising approach towards these goals, as they combine strong light-matter interaction and high photon collection efficiencies[16,99,100]. However, nanostructured environments introduce mismatch and diffusion in optical transition frequencies of emitters, making reliable photon-mediated entanglement generation infeasible[100]. In this chapter, we address this long-standing challenge by employing silicon-vacancy (SiV) color centers embedded in nanophotonic waveguides with the electromechanical strain control demonstrated in Chapter 2. Strain tuning enables control and stabilization of optical resonance between two SiV centers on the hour timescale. Using this platform, we observe the signature of an entangled, superradiant state arising from quantum interference between two spatially separated emitters in a waveguide. This demonstration and the developed platform constitute a crucial step towards a scalable quantum network with solid state quantum emitters.

3.1 Introduction

Solid-state emitters with inversion symmetry[53] are promising for use in optical quantum networks due to their ability to be integrated into nanophotonic devices[17,56,61,93]. These emitters have suppressed static electric dipole moments, decreasing the susceptibility of their optical transition frequencies to fluctuations of electric fields that occur near device surfaces[53]. This fundamental property has been leveraged most notably with the negatively charged silicon-vacancy center in diamond (SiV) to achieve emitter-photon interaction with cooperativity greater than 20 in nanophotonic cavities[17]. The platform developed around this color center also provides other essential components for quantum networking, such as a long-lived quantum memory[61] and efficient photon collection[19]. Nevertheless, in terms of advancing towards multi-qubit networks, even inversion-symmetric emitters present challenges when incorporated into nanophotonic devices. They exhibit a significant inhomogeneous distribution of their optical transition frequencies as well as residual instability in the form of spectral diffusion[93]. Demonstrating full control of their spectral behavior is necessary to generate mutually indistinguishable photons, the key ingredient for long distance entanglement[101]. Because these emitters cannot be spectrally tuned using electric fields, the established tuning mechanism for solid-state emitters[100,102], previous experiments involving indistinguishable photon generation from such defects have relied on Raman[56,103] and magnetic field[17] tuning. However, these techniques constrain either the spin or optical degree of freedom of the color center and are challenging to implement in the multi-qubit regime. The suitability of the strain tuning approach shown in Chapter 2 for photon mediated entanglement of multiple emitters remains an open question. In this work, we show that strain control can be used to manipulate the optical resonances of solid-state emitters and generate quantum interference between them. The demonstrated integration of strain control with nanophotonic devices represents a key step towards the realization of scalable quantum networks.

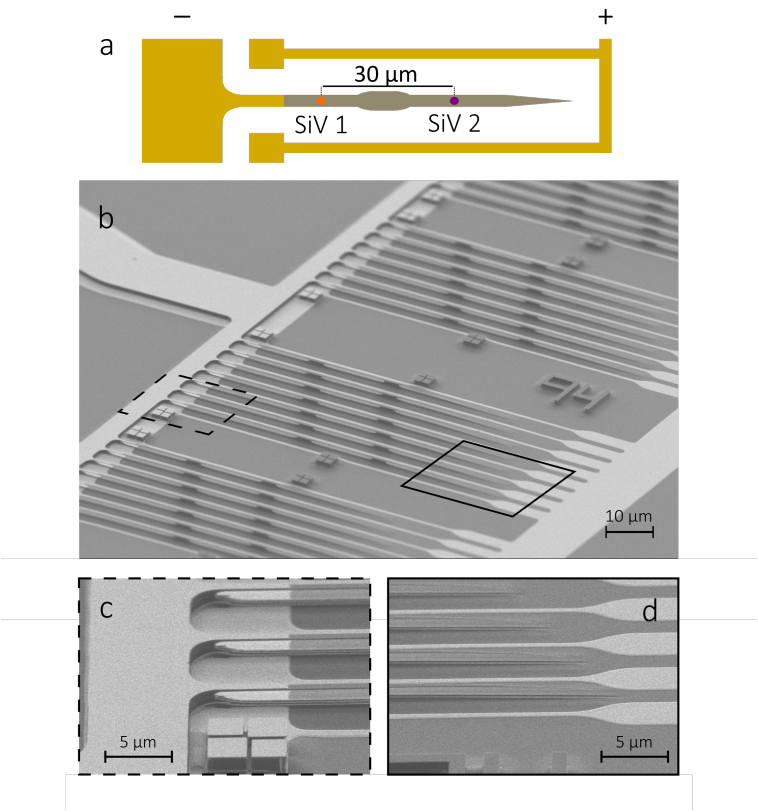

Figure 3.1: Schematic of diamond nanophotonics device. a) Diamond waveguides (gray) are implanted with color centers (purple and orange) at desired locations on the device. Electrodes (gold) are used to define a capacitor between plates located on the device (negative terminal) and below the device (positive terminal). Applying bias voltage between the plates causes the deflection of the doubly clamped cantilever. This tunes color centers between the plates and the first clamp (orange spot) without perturbing color centers beyond the clamp (purple spot). b) Scanning electron micrograph (SEM) of the photonic devices. c) Capacitor plates located on and below the devices. d) Diamond tapers used to extract photons from waveguides. This enables the extraction efficiency of more than 85% from the diamond waveguide into the fiber.

3.2 Waveguides with strain control

Our devices, presented in Figure 3.1, consist of triangular cross-section waveguides fabricated from single crystal diamond[41,92]. Each of these waveguides is connected to a support structure on one end (Figure 3.1b). The other end is tapered to allow for collection of photons from the waveguide into an optical fiber with better than 85% efficiency[19] (Figure 3.1c). In order to embed SiV centers within diamond nanophotonic devices, we adapt a masked implantation technique previously used for bulk substrates[12]. After the creation of SiV centers, gold electrodes are patterned onto the devices such that metallized parts of the waveguide act as one plate of a capacitor, with the other plate located on the dia-

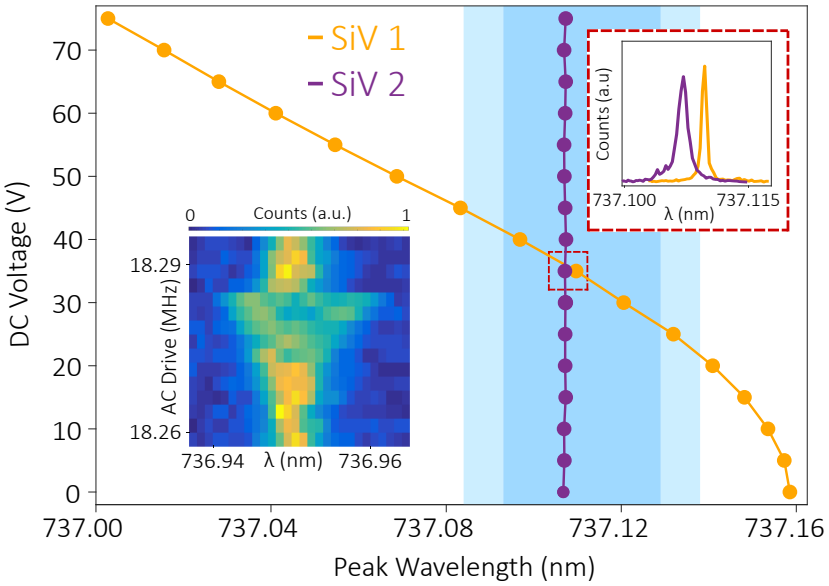

Figure 3.2: Characterization of DC and AC voltage response of the devices. Voltage bias is applied to the capacitor plates, resulting in strain fields that tune the optical transitions of SiV1 in the deflected portion of the device (orange) compared to the optical transitions of SiV2 in the stationary regions (purple). The tuning range of the SiV color center greatly exceeds the inhomogeneous distribution for 50% (75%) of SiV color centers observed in this experiment shown in dark (light) blue shading. The red inset shows the photoluminescence excitation spectra of two color centers at a voltage near the overlap. The blue inset shows the AC response of the cantilever system, measured by observing SiV optical transitions while modulating the AC driving frequency. Driving the cantilever resonance with its mechanical mode results in linewidth broadening of the color center optical transitions.

mond substrate (Figure 3.1b). Applying a voltage difference to these plates generates a force that deflects a portion of the waveguide, applying electrically controllable strain to the embedded SiV centers. This strain field perturbs the diamond lattice around the SiV and tunes the frequency of the optical transitions as discussed in Chapter 2.

Our experiments are carried in a closed cycle helium cryostat with optical access and fiber coupling capabilities (Appendix I). We measure the strain response of two SiV centers 30 µm apart within the same diamond device by resonantly exciting their optical transitions and collecting their phonon sideband emission at 4 K (Figure 3.2). The difference in the position of SiV centers in the device accounts for the difference in their response to the applied voltage, allowing us to overlap their optical transitions (Figure 3.2, red inset). The waveguide supports (Figure 3.1a, rounded gray region) between the SiV centers acts

as a mechanical clamp preventing strain from propagating and impacting spectral behavior of color centers in the portion of the waveguide beyond the clamp. We observe a tuning range of over 80 GHz, a factor of 3 larger than the total inhomogeneous distribution of the SiV optical transitions measured in these devices (Figure 3.2, blue shaded region). This is sufficient range to completely eliminate the effects of static strain variations on SiV optical transitions.

To determine the bandwidth of our electromechanical actuation scheme, we investigate an SiV color center's spectral response to AC mechanical driving of the nanophotonic structure (Figure 3.2, blue inset). We apply a DC bias combined with a variable-frequency RF signal to the gold electrodes and monitor the SiV optical transition. When the RF drive frequency matches one of the nanobeam's mechanical modes, we observe linewidth broadening of the SiV coupled to this mechanical mode due to the resonant amplification of the driving signal as seen with the NV spin in Chapter 1. Using this technique, we observe and drive modes with mechanical frequencies of up to 100 MHz. Optimizing the device design could enable the electromechanical driving of vibrational modes with GHz frequencies which are resonant with SiV spin transitions.

The high bandwidth of our electromechanical actuation scheme is sufficient to suppress spectral diffusion exhibited by the SiV center[93]. Monitoring an SiV center's optical transition over the course of five hours, we observe spectral diffusion that is an order of magnitude larger than its single-scan linewidth of around 300 MHz (Figure 3.3a). Using a pulsed feedback scheme that applies a voltage adjustment every 20 seconds we reduce the total summed linewidth by almost an order of magnitude on a timescale of several hours (Figure 3.3b). The efficacy of this feedback scheme is limited by the long duration of the laser scan used to capture the full extent of the spectral diffusion. More sophisticated feedback schemes may be employed in the future to ensure better locking of the SiV optical transition to the target frequency.

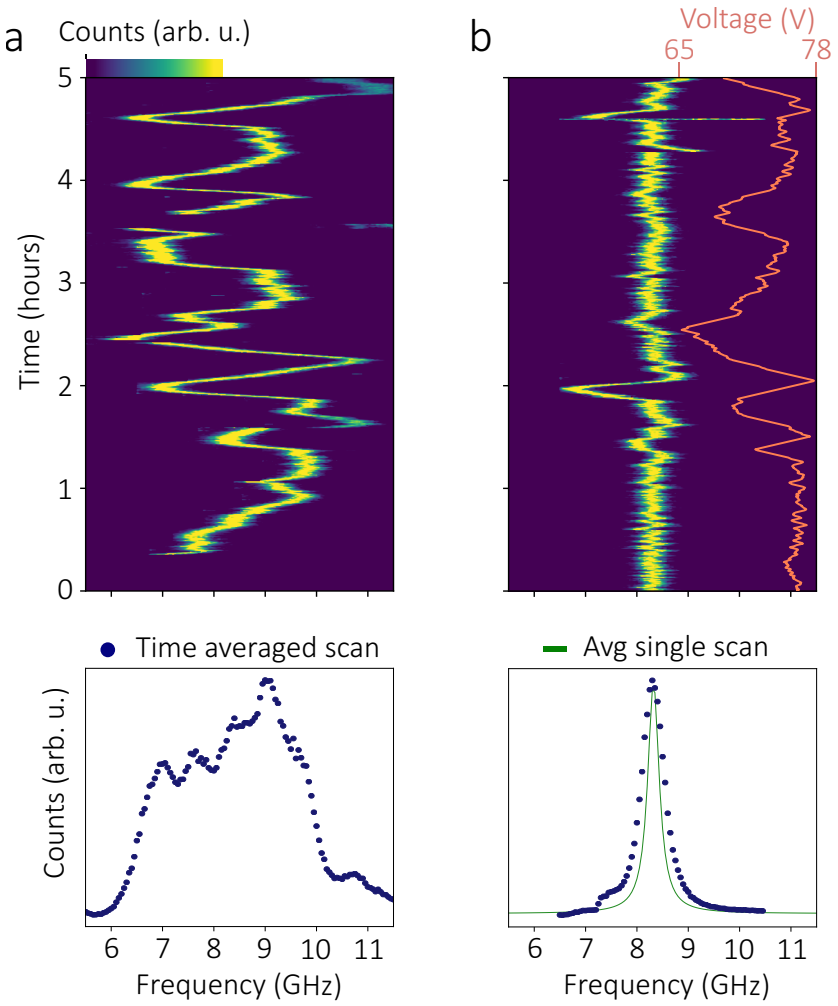

Figure 3.3: Reduction of spectral diffusion using nanomechanical strain. a) Top: Spectral diffusion of SiV center optical transition, measured over a 5-hour period. Bottom: Time-averaged spectrum over the same period. b) Top: Measurement of the SiV spectral diffusion with 20 second pulsed feedback over a 5-hour period. Bottom: Time-averaged spectra over a 5-hour period (blue dots) show the reduction of total linewidth down to 500 MHz. The average of single-scan SiV linewidths is 350 MHz (green line).

3.3 Observation of quantum interference

With the optical transitions of the SiV centers tuned and stabilized, we proceed to generate probabilistic entanglement between two color centers. We begin by using strain control to set the optical transition frequencies between the lower branch of the ground state ($|c\rangle$) and the excited state ($|e\rangle$) of two emitters at the target detuning (Δ) by applying the appropriate voltage (Figure 3.4a). The transitions between the upper branch of the ground state ($|u\rangle$) and the excited state ($|e\rangle$) of the two emitters are then continuously excited using two separate lasers (Figure 3.4a). Finally, the photons emitted into the diamond waveguide are collected through a tapered fiber interface and filtered using a high finesse Fabry-Perot filter (see Appendix I) in order to separate the desired optical transition from the excitation laser[56].

We characterize our setup by measuring the second order correlation function between photons from a single excited SiV center (Figure 3.4c, left panel). We observe the suppression of photon coincidences with $g^{(2)}_{single}(0) = 0.13(4)$, a quantity raised above its ideal value of 0 by dark counts of the photon detectors. Next, we simultaneously excite both SiV centers and measure their photon correlation function. When two excited SiV centers are spectrally detuned ($\Delta \neq 0$), their emitted photons are distinguishable and the detection of the first photon projects the system into the statistical mixture of the $|ce\rangle$ and $|ec\rangle$ states (Figure 3.4b, blue path)[56]. In this case, the zero-time-delay photon correlation function reaches $g^{(2)}_{dist}(0) = 0.50(7)$ (Figure 3.4c, left panel).

When the two SiV optical transitions are tuned into resonance ($\Delta = 0$), detection of the first emitted photon from a pair of excited SiV color centers projects the system into an entangled, bright state (Figure 3.4b, red path). This state is identified by the superradiant emission of a second photon at twice the rate expected from the distinguishable case[56,104]. We confirm the generation of an entangled state by observing a superradiant peak in the photon correlation function (Figure 3.4c, right panel) with $g^{(2)}_{ind}(0) = 0.88(8)$. Experimental results are in good agreement with a simulated model of our system (Figure 3.4c, red

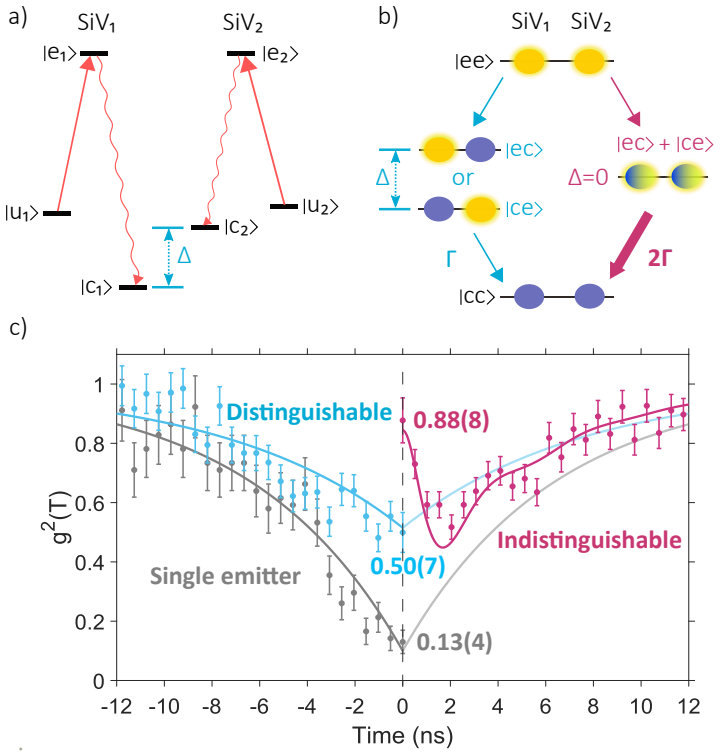

Figure 3.4: Observation of the superradiant entangled state using strain control. a) Level structure for two SiV centers. Strain tuning of one SiV color center changes the detuning (Δ) between their $|e\rangle$ to $|c\rangle$ transitions. Separate lasers are applied to excite the $|u\rangle$ to $|e\rangle$ transition of each emitter. b) A single photon emitted from the two excited emitters with distinguishable transitions ($\Delta \neq 0$) projects the system to a statistical mixture of $|ec\rangle$ and $|ce\rangle$ states (blue decay path). When the emitters are indistinguishable ($\Delta = 0$), the emission of one photon projects the system into a superradiant bright state (purple decay path) that decays at a rate two times faster than that of the statistical mixture. c) The second order photon correlation function is measured for a single emitter (left panel, gray data points) and for two spectrally distinguishable emitters (left panel, blue data points). Measured $g^{(2)}(0)$ is 0.13(4) and 0.50(7) for the single emitter and distinguishable cases, respectively. Exponential curves fit to the data are plotted and mirrored onto the right half of plot (gray and blue lines). For two emitters tuned into resonance, we observe the generation of a superradiant entangled state, signified by the peak in the photon correlation (right panel, purple data points). Data is overlaid with a simulated model with a single fit parameter. For indistinguishable emitters, we measure $g^{(2)}(0) = 0.88(8)$, limited primarily by detector jitter.

curve) which uses only a single fitting parameter, the phonon-induced mixing rate between the $|u\rangle$ and $|c\rangle$ ground states[105] (see[106] for detailed description of the model). Using the height of the superradiant peak and the value of the $g^{(2)}_{single}$, we calculate a lower bound on the conditional bright state fidelity to be 0.8(1), indicating the observation of an entangled state[56].

In particular, the $g^{(2)}$ data presented in the right panel of Figure 3.4 can be understood as consisting of two parts. First, the "dip" with a decay timescale of about 10 ns occurs because photons collected in this experiment can only be generated from the $|e\rangle$ state, and the detection of a photon leads to projection of the system into the $|c\rangle$ state. The timescale of the dip then corresponds to the average amount of time between the emitter arriving in the $|c\rangle$ state and it being excited to the $|e\rangle$ state. This timescale is primarily set by the ground state mixing rate between $|c\rangle$ and $|u\rangle$ states in our experiment , but in cases of low laser driving power can also be broadened by the slow Rabi driving between the $|e\rangle$ and $|u\rangle$ states. The second feature is the superradiant peak. Theoretically, the width of this peak should be set to roughly 1 ns (half of the excited state lifetime), as superradiant effects should dominate at this timescale. In reality, both the electronic jitter and the laser power impact the measured width. The total electronic jitter measured in our detection electronics is 350 ps, a timescale comparable to the anticipated peak timescale of 1 ns, leading to broadening of the measured feature. Fast laser driving could also reduce the timescale of the peak by providing another driven decay channel (stimulated emission) from the bright state. The oscillations in the $g^{(2)}$ for indistinguishable emitters result from a combination of small mismatch between emitter optical transitions and Rabi driving between the $|u\rangle$ and $|e\rangle$ states in line with the theory.

3.4 Outlook

In conclusion, we show a scalable approach to generating quantum interference between solid state emitters in nanophotonic devices using strain. Using strain control, we realize a reduction of spectral diffusion by almost an order of magnitude over a broad bandwidth and achieve a spectral tuning range exceeding 150 pm, several times greater than the SiV inhomogeneous distribution inside nanophotonic devices. This approach can be directly adapted to other quantum emitters such as quantum dots, as well as other inversion-symmetric color centers in diamond[107,108,109]. Furthermore, high frequency strain control inside a nanophotonic cavity can lead to a photon or phonon mediated gate between quantum memories[17,18,110]. Our platform fulfills the requirements for an ideal quantum network node and paves the way for realization of large-scale quantum networks.

Chapter 4

Strain control of spin coherence in the silicon vacancy center

For quantum bits in the solid state, decoherence from thermal vibrations of the surrounding lattice can typically only be suppressed by lowering the temperature of operation. In this chapter, we use the strain tuning platform developed in Chapter 2 to mitigate the effect of thermal phonons on the silicon-vacancy (SiV^-) electronic spin without changing the system temperature. By controlling the strain environment of the color center, we tune its electronic levels to probe, control, and eventually suppress the interaction of its spin with the thermal bath.

4.1 Introduction

Phonon-driven processes are responsible for relaxation and decoherence processes in a variety of solid state emitters that can serve as optically accessible quantum memories[59,111,112,113,107,114]. In particular, for emitters with spin-orbit coupling, such processes can demand operation at sub-Kelvin temperatures[61,91,99], or the use of magnetic fields of several Tesla[115] to achieve long spin relaxation and coherence times. This requires cryogenic setups that are significantly more complex than common helium-4 cryostats employed to obtain coherent

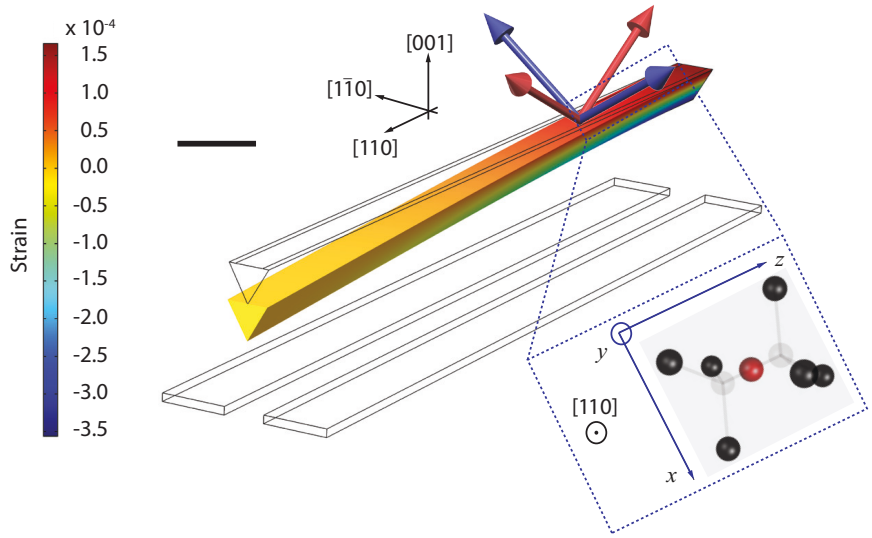

Figure 4.1: Simulation of the displacement of the cantilever due to the application of a DC voltage of 200 V between the top and bottom electrodes. The component of the strain tensor along the long axis of the cantilever is displayed using the color scale. Scale bar corresponds to 2. Crystal axes of diamond are indicated in relation to the geometry of the cantilever. Arrows on top of the cantilever indicate the highest symmetry axes of four possible SiV^- orientations, and their color indicates separation into two distinct classes upon application of strain. SiVs studied in this work are shown by blue arrows are oriented along $[1\bar{1}1]$, $[\bar{1}11]$ directions, are orthogonal to the cantilever long-axis, and experience strain predominantly in the plane normal to their highest symmetry axis. Inset shows the molecular structure of such a transverse orientation SiV along with its internal axes, when viewed in the plane normal to the $[110]$ axis.

optical photons from solid-state emitters.

Our approach to mitigate phonon-induced decoherence takes advantage of the fact that the large electron-phonon coupling responsible for decoherence fundamentally arises from a high susceptibility of the electronic orbitals to lattice strain as characterized in Chapter 2. Through strain control, we increase the energy scale for phonon absorption by the emitter to far above the thermal energy ($k_B T \approx 0.3\,\text{meV}$ at the experimental temperature, $T = 4\,\text{K}$). The resulting depletion of thermal phonons seen by the SiV^- leads to an improvement in its spin coherence time.

4.2 Controlling electron-phonon processes

The strain profile from the NEMS device used in Chapter 2 can be calculated numerically via a finite-element-method (FEM) simulation, as shown in Fig. 4.1. Of the two possible

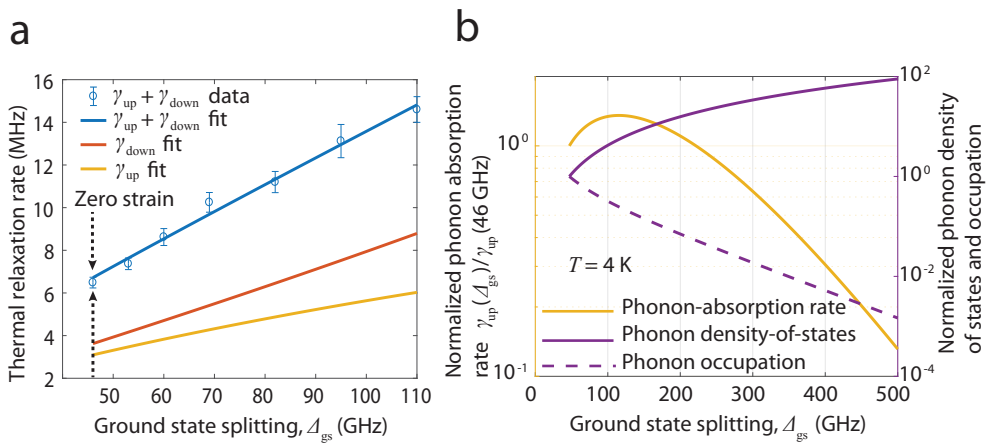

Figure 4.2: Strain-tuning of the SiV$^-$ energy levels. (a) Thermal relaxation rates between GS orbital branches vs. their energy splitting. Error bars represent standard deviation of the estimated rate, and are under 5% for all data points. Fit to model in Appendix E.1 allows extraction of the phonon-absorption rate γ_{up} and phonon-emission rate γ_{down}. (b) Calculated phonon-absorption rate $\gamma_{\mathrm{up}}(\Delta_{\mathrm{gs}})$ (solid yellow line) as a function of GS-orbital splitting Δ_{gs} at temperature $T = 4$ K. Left y-axis indicates the magnitude of this rate normalized to the value at zero strain, $\gamma_{\mathrm{up}}(46\ \mathrm{GHz})$. Right y-axis indicates the two competing factors whose product determines γ_{up}: the phonon density of states (normalized to its value at zero strain), shown with the solid violet line, and the thermal occupation of acoustic modes shown with the dashed violet line.

orientations of SiV$^-$ centers in our device, we address those with transverse orientation (labelled blue, and shown in detail in inset of Fig. 4.1c), which predominantly experience strain in the plane normal to their highest symmetry axis i.e. E_g strain. Upon deflecting the cantilever, the GS and ES splittings of this SiV as increase as shown in Fig. 2.3 due to E_g strain mixing orbitals within the GS and ES manifolds. As a consequence of this mixing interaction, phonons with nonzero E_g strain components can induce resonant transitions between these orbitals.

With our device we can tune the splitting of the orbitals in the GS manifold from 46 GHz to typically up to 500 GHz, and in the best case, up to 1.2 THz (see Appendix D.1). Given the enormous range of control over the GS orbital splitting, we can probe the interaction between the color center and phonons of different frequencies. This is achieved by measuring the thermal relaxation rate between the orbitals with a time-resolved pump-probe technique (Fig. 4.2b) discussed in Appendix D.3. Measurements are performed in the frequency range $\Delta_{\mathrm{gs}} = 46$ GHz to 110 GHz where this technique can be applied. The total

relaxation rate is a sum of the rates of phonon absorption, γ_{up}, and emission, γ_{down} (shown by the dashed and solid squiggly arrows respectively in Fig. 4.3a), which can be individually extracted using the theory described in Appendix E.1. Over the range of Δ_{gs} measured, phonon processes in both directions are observed to accelerate with increasing orbital splitting. This is because the number of acoustic modes resonant with the GS splitting, i.e. the phonon density of states (DOS) at Δ_{gs}, increases with the dependence Δ_{gs}^{n} (n depends on the geometry of material seen by resonant phonons, see Appendix E). However, if the orbital splitting is increased far above 120 GHz (at temperature $T = 4\,\mathrm{K}$) as plotted in Fig. 4.2c, the phonon absorption rate (γ_{up}) is theoretically expected to reverse its initial trend. In this regime, the polynomial increase in phonon DOS is outweighed by the exponential decrease in thermal phonon occupation ($\sim \exp(-h\Delta_{\mathrm{gs}}/k_{\mathrm{B}}T)$)[59], and consequently γ_{up} is rapidly quenched.

4.3 Strain-enhanced spin T_2^* and T_1

In the presence of magnetic field, the SiV^- electronic levels further split into spin sublevels and provide an optically accessible spin qubit as shown in Fig. 4.3a[51,60,58,116]. When a thermal phonon randomly excites the SiV center from the qubit manifold to the upper orbital branch, as shown by the dotted squiggly arrows in Fig. 4.3(a), the energy of the qubit suddenly changes by an amount $\sim h\Delta_{\mathrm{gs}}$. After some time in the upper branch, the system randomly relaxes back to the lower manifold through spontaneous emission of a phonon as shown by the solid squiggly arrows in Fig. 4.3(a). In this process, the spin projection is conserved, since phonons predominantly flip only the orbital character. However, a random phase is acquired between the $\downarrow$ and $\uparrow$ projections of the qubit due to phonon absorption and emission, as well as faster precession in the upper manifold. The qubit dephasing rate is thus determined by the upward phonon transition rate γ_{up}. A suppression of phonon absorption at high strain can therefore improve the spin coherence of the emit-

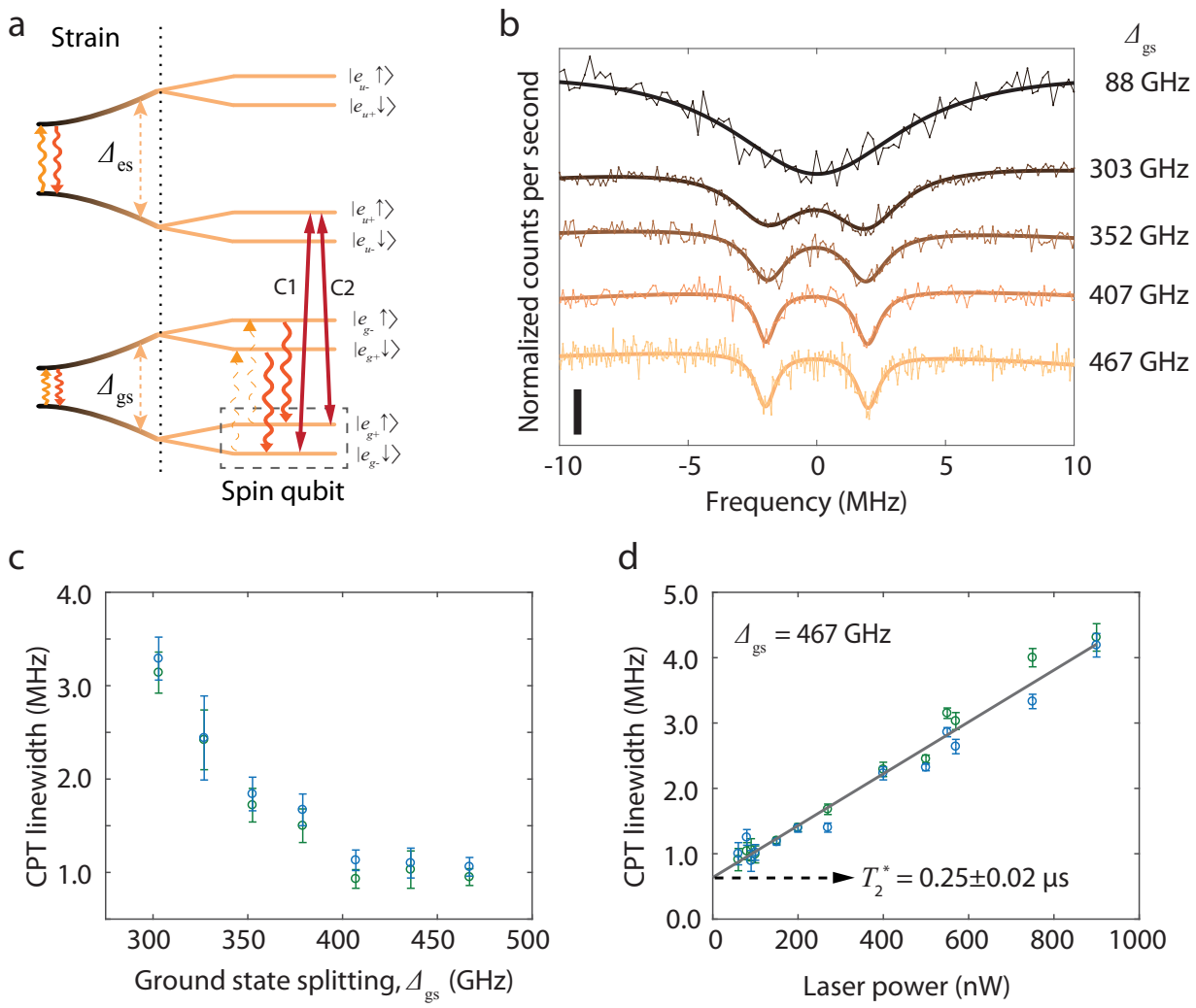

Figure 4.3: Spin coherence measurements. (a) SiV$^-$ level structure in the presence of strain and external magnetic field. A qubit is defined with levels $|e_{g-}\downarrow\rangle$ and $|e_{g+}\uparrow\rangle$ on the lower spin-orbit branch of the GS. This qubit can be polarized, and prepared optically using the Λ-scheme provided by transitions C1 and C2. Phonon transitions within ground- and excited-state manifolds are also indicated. The upward phonon transition (phonon absorption process) can be suppressed at high strain, thereby mitigating the effect of phonons on the coherence of the spin qubit. (b) Coherent population trapping (CPT) spectra probing the spin transition at increasing values of the GS orbital splitting Δ_{gs} from top to bottom. Scale bar in bottom left represents a fluorescence signal contrast of 10%. Measurements are carried till the noise in the fluorescence signal is below 1.5%. Bold solid curves are Lorentzian fits. Optical power is adjusted in each measurement to minimize power-broadening. (c) Linewidth of CPT dips as a function of GS orbital splitting Δ_{gs} indicating improvement in spin coherence with increasing strain. Error bars represent standard deviation of the estimated linewidths from the Lorentzian fits. (d) Power dependence of CPT-linewidth at the highest strain condition (Δ_{gs}= 467 GHz). Data points are estimated linewidths from CPT measurements, and the solid curve is a linear fit, which reveals linewidth of 0.64 ± 0.06 MHz corresponding to $T_2^* = 0.25 \pm 0.02\mu$s.

ter.

We use coherent population trapping (CPT) to measure the spin coherence at high strain. Through simultaneous resonant laser excitation of the optical transitions labeled C1 and C2, we pump the SiV^- into a dark state, a coherent superposition of the qubit levels $|e_{g-} \downarrow \rangle$, $|e_{g+} \uparrow\rangle$ [58,116]. When the two-photon detuning is scanned, preparation of the dark state results in a fluorescence dip, whose linewidth is determined by the optical driving and spin dephasing rates. At low laser powers, the linewidth is limited by spin dephasing, which is dominated by phonon-mediated transitions within the GS manifold [59]. In Fig. 4.3b, as the dark resonance narrows down due to prolonged spin coherence with increasing strain, we reveal a fine structure not visible before. Further measurements in Appendix F suggest that the presence of two resonances is due to interaction of the SiV^- electron spin with a neighbouring spin such as a ^{13}C nuclear spin. This indicates the possibility of achieving a local register of qubits as has been demonstrated with NV centers [82]. Fig. 4.3c shows the decreasing linewidths of the CPT resonances with increasing GS orbital splitting, indicating an improved spin coherence time. Beyond a GS splitting of $\sim$400 GHz, the linewidths saturate at $\sim$1 MHz. At the highest strain condition, we perform a power dependent CPT measurement to eliminate the contribution of power broadening, and extract a spin coherence time of $T_2^* = 0.25 \pm 0.02$ (compared with other CPT-based measurements which reported $T_2^* = 40$ ns without strain control [58,116]). This saturation of T_2^* suggests the mitigation of the primary dephasing source, single-phonon transitions between the GS orbitals, and the emergence of a secondary dephasing mechanism such as slowly varying magnetic fields from naturally abundant (1.1%) ^{13}C nuclear spins in diamond. We note that our longest $T_2^* = 0.25 \pm 0.02$ is on par with that of the NV^- center without dynamical decoupling [117,118], and of low-strain SiV^- centers operated at a much lower temperature of 100 mK [61], the conventional approach to suppress phonon-mediated dephasing.

Population decay or longitudinal relaxation of the qubit is significantly slower than coherence decay and is driven by spin-flipping phonon transitions shown by the red arrows

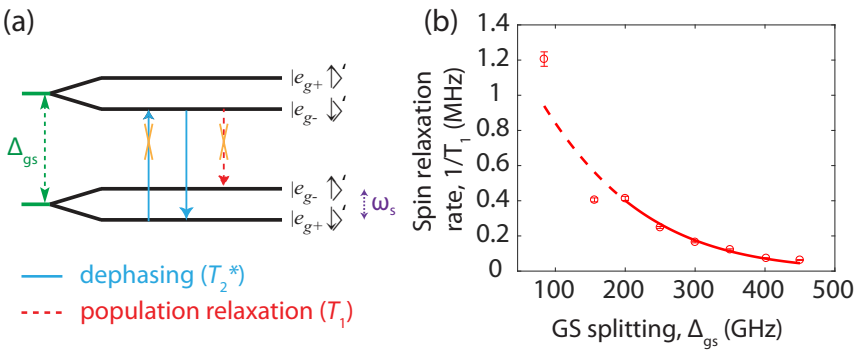

Figure 4.4: (a) Illustration of dephasing and population decay processes for the SiV spin. Blue arrows show spin-conserving transitions responsible for dephasing. Red arrow shows a spin-flipping transition driving decay from $|e_{g+}\downarrow\rangle'$ to $|e_{g-}\uparrow\rangle'$. Processes suppressed at high strain are crossed out. (b) Reduction in spin relaxation rate $(1/T_1)$ with increasing GS splitting $\Delta_{\rm gs}$ as extracted from pump-probe measurements. Solid line is a fit to the resonant two-phonon relaxation model in Appendix E.2 for $\Delta_{\rm gs}$ above 200 GHz where this model is valid. Dotted line is an extrapolation of the fit into the low strain regime.

in Fig. 4.4a, which occur with a small probability due to perturbative mixing of spin projections. A detailed analysis of various decay channels is presented in Appendix E.2. At high strain, it can be shown that the decay rate is approximately $4\left(d_{g,\rm flip}/d_g\right)^2\gamma_{\rm up}$, where $d_{g,\rm flip}$ is the strain susceptibility for a spin-flipping transition such as $|e_{g+}\downarrow\rangle' \rightarrow |e_{g+}\uparrow\rangle'$. Thus it is a fraction of the spin-conserving transition rate $\gamma_{\rm up}$, which determines the qubit decoherence. The factor $d_{g,\rm flip}/d_g$ scales as $\sim 1/\Delta_{\rm gs}$ according to first order perturbation theory. As a result, we expect exponential decrease in the population decay rate similar to the decrease in decoherence, but with a different polynomial pre-factor. Fig. 4.4b shows this decreasing trend with increasing $\Delta_{\rm gs}$ fit to a two-phonon relaxation model. As strain is increased, spin T_1 increases six-fold to a value of 2.5 μs at the highest GS splitting of 450 GHz.

4.4 Outlook

As a next step to the demonstrations in this chapter, we can further improve the spin coherence at high strain by cancelling the effect of slowly varying non-Markovian noise from the environment[61] using dynamical decoupling techniques that are well-studied with other spin systems[82,119,120]. Our strain engineering approach can be applied to overcome phonon-

induced decoherence in other emitters such as emerging inversion-symmetric centers in diamond[107,108,109], Kramers rare earth ions[114,99,115], and in general, systems with spin-orbit coupling in their ground state. If active tuning is not required, high strain necessary to quench phonon processes can be achieved simply by deposition of a thin film[121], which passively stresses the underlying crystal. Finally, the limiting effects of thermal phonons on the SiV qubit prompt investigation into whether these interactions can be engineered to be coherent, and this will be the topic of the following chapters.

Chapter 5

Tailoring the silicon vacancy for strong electron-phonon coupling

A natural extension of our results in Chapters 2 and 4 is coherent coupling of the SiV spin to a well-defined mechanical mode, which will enable the use of phonons as quantum resource. In particular, we can combine the large strain susceptibility of the SiV with mechanical resonators of dimensions close to the phonon wavelength[84] to obtain orders of magnitude larger spin-phonon interaction strengths compared with previous works[68,66,67,122,29,31], leading to strong spin-phonon coupling. In this regime, one can realise phonon-mediated two-qubit gates[123] analogous to those implemented with trapped ions[124], and achieve quantum non-linearities required to deterministically generate single phonons and non-classical mechanical states[125,126,127,25,26], a long sought-after goal since phonons can be used to interface spins with other quantum systems[11].

In this chapter, we continue with the strain dependent spectroscopy experiments from Chapter 2, this time in the presence of a magnetic field. The results of these measurements give us insight into how the SiV can be tailored for strong coupling to a well-defined mechanical mode using the right combination of external strain and magnetic fields.

5.1 Strain response of optical transitions in a magnetic field

In Chapter 4, we saw that static E_g-strain in the SiV environment can significantly impact spin coherence and relaxation rates by modifying the orbital splitting in the GS. In this section, we discuss effects that arise in the presence of a magnetic field due to competition between SO coupling and E_g-strain. Particularly, we notice tuning in the spin transition frequency, ω_s by a large amount (a few GHz) at a fixed external magnetic field by simply controlling local strain. At the same time, we discuss how the magnitude of local strain strongly determines the ability to couple or control the SiV qubit with external fields such as AC strain or microwaves at frequency ω_s, and resonant laser-fields in a Λ-scheme.

The strain-response of the SiV qubit is measured by monitoring the four Zeeman-split optical lines arising from the C transition as shown schematically in Fig. 5.1(a). In Fig. 5.1(b), we apply a fixed magnetic field B =0.17 T aligned along the vertical [001] axis with a permanent magnet placed underneath the sample, and gradually increase the GS splitting of a transverse-orientation SiV by applying strain. With increasing strain, each of the four Zeeman-split optical transitions moves outwards from the position of the unsplit C transition at zero magnetic field. In particular, the spin-conserving inner transitions C2 and C3 overlap at zero strain, but become more resolvable with increasing strain. Thus, all-optical control of the spin[91] relying on simultaneous excitation of a pair of transitions C1 and C3 (or C2 and C4) forming a Λ-scheme requires the presence of some local strain. The strain-tuning behavior of Zeeman split optical transitions can be theoretically calculated by diagonalizing the GS and ES Hamiltonians in the presence of a magnetic field. Upon adding Zeeman terms to the Hamiltonian in equation F.5, and switching to the basis

of SO eigenstates $\{e_{g-}\downarrow, e_{g+}\uparrow, e_{g+}\downarrow, e_{g-}\uparrow\}$, we obtain

$$\mathbb{H}^{\text{total}} = \begin{bmatrix} -\lambda_{\text{SO}}/2 - \gamma_L B_z - \gamma_s B_z & 0 & \epsilon_{E_{gx}} & \gamma_s B_x \\ 0 & -\lambda_{\text{SO}}/2 + \gamma_L B_z + \gamma_s B_z & \gamma_s B_x & \epsilon_{E_{gx}} \\ \epsilon_{E_{gx}} & \gamma_s B_x & \lambda_{\text{SO}}/2 + \gamma_L B_z - \gamma_s B_z & 0 \\ \gamma_s B_x & \epsilon_{E_{gx}} & 0 & \lambda_{\text{SO}}/2 - \gamma_L B_z + \gamma_s B_z \end{bmatrix} \tag{5.1}$$

Here we have discarded the A_{1g} and E_{gy} strain terms, since the transverse-orientation SiVs in our experiments experience predominantly E_{gx} strain. We have also assumed that the transverse component of the magnetic field is entirely along the x-axis of the SiV. The gyromagnetic ratios are $\gamma_s = 14$ GHz/T, $\gamma_L = 0.1(14)$ GHz/T, where the pre-factor of 0.1 is a quenching factor for the orbital angular momentum.[53] The result of our calculation is shown in Fig. 5.1(c). In the low strain regime indicated by the region with the shaded gradient, we reproduce the experimental behavior in Fig. 5.1(b), and obtain good quantitative agreement with the variation in the spin transition frequency ω_s in Fig. 5.1(d).

Physically, this behavior of the spin transitions arises as strain and SO coupling compete to determine the orbital wavefunctions. From the Hamiltonian in equation 5.1, we can see that the eigenstates begin as SO eigenstates $\{e_{g-}\downarrow, e_{g+}\uparrow, e_{g+}\downarrow, e_{g-}\uparrow\}$ at zero strain, and end up as the pure orbitals $\{e_{gx}\downarrow, e_{gx}\uparrow, e_{gy}\downarrow, e_{gy}\uparrow\}$ at high strain ($\epsilon_{E_{gx}} \gg \lambda_{\text{SO}}/2$). At zero strain, the effective magnetic field from SO coupling quantizes the electron spin along the $z-$axis. In this condition, the off-axis B-field does not affect the spin transition frequency ω_s to first order, so $\omega_s \sim 2(\gamma_s + \gamma_L)B_z = 3.1$ GHz. As the strain $\epsilon_{E_{gx}}$ is increased far above the SO coupling λ_{SO} and the eigenstates approach the pure orbitals, the spin quantization axis approaches the direction of the external magnetic field, and ω_s approaches $2\gamma_s B = 4.8$ GHz. Since SO coupling in the ES is stronger, this limit is attained at higher values of strain than in the GS as shown by the dashed line in Fig. 5.1(d). In the limit of very high strain, the transitions C2 and C3 also become strictly spin-conserving, and optical pumping-based initialization and readout of the qubit[60,128]

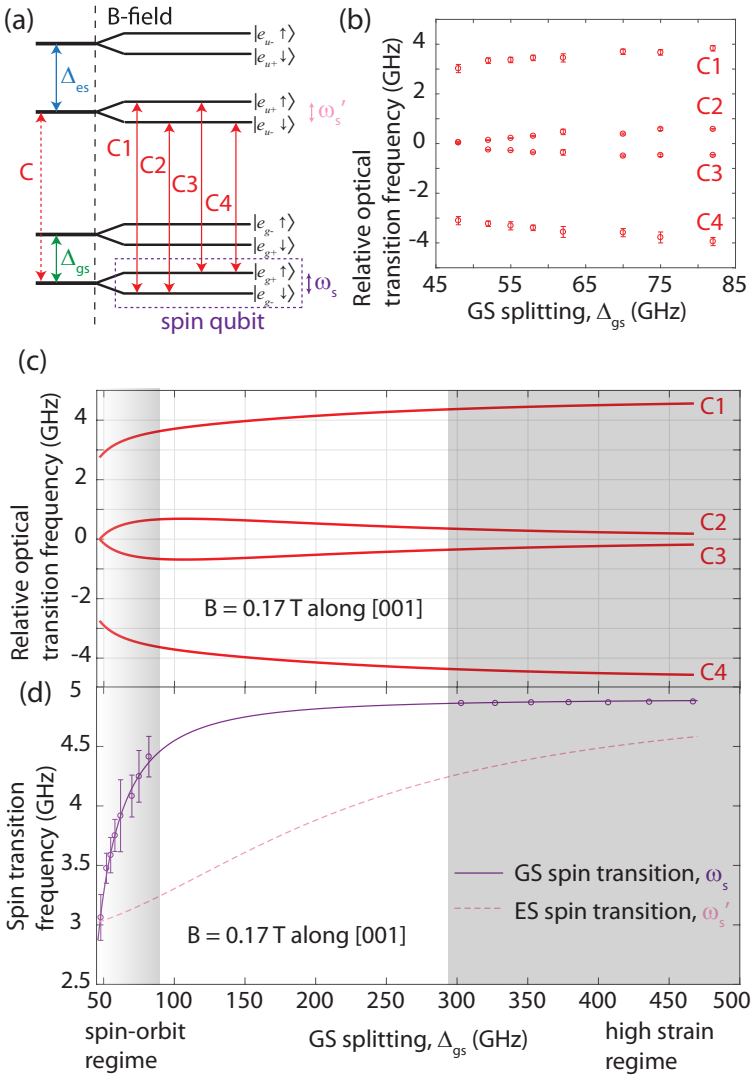

Figure 5.1: (a) Splitting of the C transition into the four transitions C1, C2, C3, and C4 in the presence of a magnetic field. Spin transition frequencies on the lower orbital branches of the GS and ES are ω_s, ω_s' respectively. (b) Response of transitions C1, C2, C3, and C4 upon tuning GS splitting $\Delta_{\rm gs}$ with E_g-strain. (c) Calculated response of optical transitions C1, C2, C3, and C4 to E_g-strain in presence of 0.17 T B-field aligned along the [001] direction. Shaded regions on the left and right ends indicate the regimes in which the GS orbitals are determined by SO coupling and strain respectively. (d) Strain response of spin transition frequencies upon tuning of ground state orbital splitting $\Delta_{\rm gs}$ with E_g-strain. SO regime data points are extracted from the optical spectra in Fig. 5.1(b). High strain regime data points are obtained from CPT measurements on the SiV studied in Fig. 4.3 (error bars for these points are smaller than data markers). Solid (dashed) line is calculated spin transition frequency on the lower orbital branch of GS (ES) from 5.1(c).

are no longer possible. Instead, initialization by measurement and single-shot readout[61] of the spin through resonant excitation of one of these spin-cycling transitions can be implemented, as long as these transitions remain optically resolvable from each other. Once local strain is even further increased to the point where SO coupling is merely perturbative, the difference in GS and ES spin transition frequencies becomes vanishingly small, eventually leading to overlapping C2 and C3 optical transitions as depicted on the right hand side of Fig. 5.1(c). For instance, for the magnetic field of 0.17 T used in these experiments, these transitions will become separated by their linewidth (∼200 MHz) at a ground state splitting of 700 GHz. If the local strain is increased beyond this limit, all-optical control and single-shot readout of the qubit[61] will become impossible unless higher magnetic field is applied to increase the separation between these transitions.

5.2 A GHz frequency qubit with high strain susceptibility

The rapid variation of the spin transition frequency ω_s in the low-strain regime of Fig. 5.1(d) provides the first hint that the qubit formed by the two lowest spin-orbit states can be very sensitive to oscillating strain generated by coherent phonons. The interaction terms due to strain and the off-axis magnetic field predicted by the Hamiltonian in equation 5.1 are depicted visually in Fig. 5.2(a). In particular, at zero strain, the presence of the off-axis magnetic field perturbs the eigenstates of the qubit to first order as

$$|e_{g-}\downarrow\rangle' \approx |e_{g-}\downarrow\rangle + \frac{\gamma_s B_x}{\lambda_{\mathrm{SO,gs}}}|e_{g-}\uparrow\rangle \tag{5.2}$$

$$|e_{g+}\uparrow\rangle' \approx |e_{g+}\uparrow\rangle + \frac{\gamma_s B_x}{\lambda_{\mathrm{SO,gs}}}|e_{g+}\downarrow\rangle \tag{5.3}$$

This perturbative mixing with opposite spin-character can now allow resonant AC strain at frequency ω_s to drive transitions between the qubit levels. For a small amplitude of

such AC strain $\epsilon^{AC}_{E_{gx}}$, we can calculate the strain susceptibility of the spin transition d_{spin} in terms of the GS orbital strain susceptibility d_g in Eq. 2.8.

$$d_{\text{spin}} = \frac{\langle e_{g-} \downarrow' | \mathbb{H}^{\text{strain}} | e_{g+} \uparrow' \rangle}{\epsilon^{AC}_{E_{gx}}} d_{\text{gs}} = \frac{2\gamma_s B_x}{\lambda_{\text{SO,gs}}} d_{\text{gs}} \tag{5.4}$$

Since d_g is very large ($\sim$1 PHz/strain), even with the presence of the pre-factor $\gamma_s B_x/\lambda_{\text{SO,gs}}$, the qubit levels themselves can have a relatively large strain-response. For the present case of B=0.17 T along the [001] axis, we get $d_{\text{spin}}/d_{\text{gs}} = 0.085$ yielding $d_{\text{spin}} \sim 100$ THz/strain. An exact calculation of d_{spin} for arbitrary local static strain using the Hamiltonian in equation 5.1 is shown in Fig. 5.2(b). As static strain in the SiV environment is increased far above the SO coupling, the AC strain susceptibility approaches zero. Thus we can conclude that coupling the SiV qubit levels to resonant AC strain requires (i) low static strain $\epsilon_{E_g} \ll \lambda_{\text{SO,gs}}/2$ and (ii) a non-zero off-axis magnetic field B_x. The qubit levels can also dispersively couple to off-resonant AC strain with a different susceptibility t_{spin}, and this is discussed in Appendix H.1. In Appendix H.2, we discuss how static strain is essential for a nonzero response of the qubit levels to resonant microwave magnetic fields.

5.3 A coherent spin-phonon interface

Our results on the strain response of the electronic and spin levels of the SiV indicate the potential of this color center as a spin-phonon interface. The diamond NV center spin, the most investigated candidate in this direction has an intrinsically weak strain susceptibility ($\sim$ 10 GHz/strain) since the qubit levels are defined within the same orbital in the GS configuration of the defect as discussed in Chapter 1. While using distinct orbitals in the ES can provide much larger strain susceptibility ($\sim$ 1 PHz/strain)[86,129], such schemes will be limited by fast dephasing due to spontaneous emission and spectral diffusion. In comparison, the SiV center provides distinct orbital branches within the GS itself. Further, the presence of SO coupling dictates that the qubit levels $|e_{g-} \downarrow\rangle, |e_{g+} \uparrow\rangle$ correspond to dif-

ferent orbitals. As a result, one achieves the ideal combination of high strain susceptibility and low qubit dephasing rate.

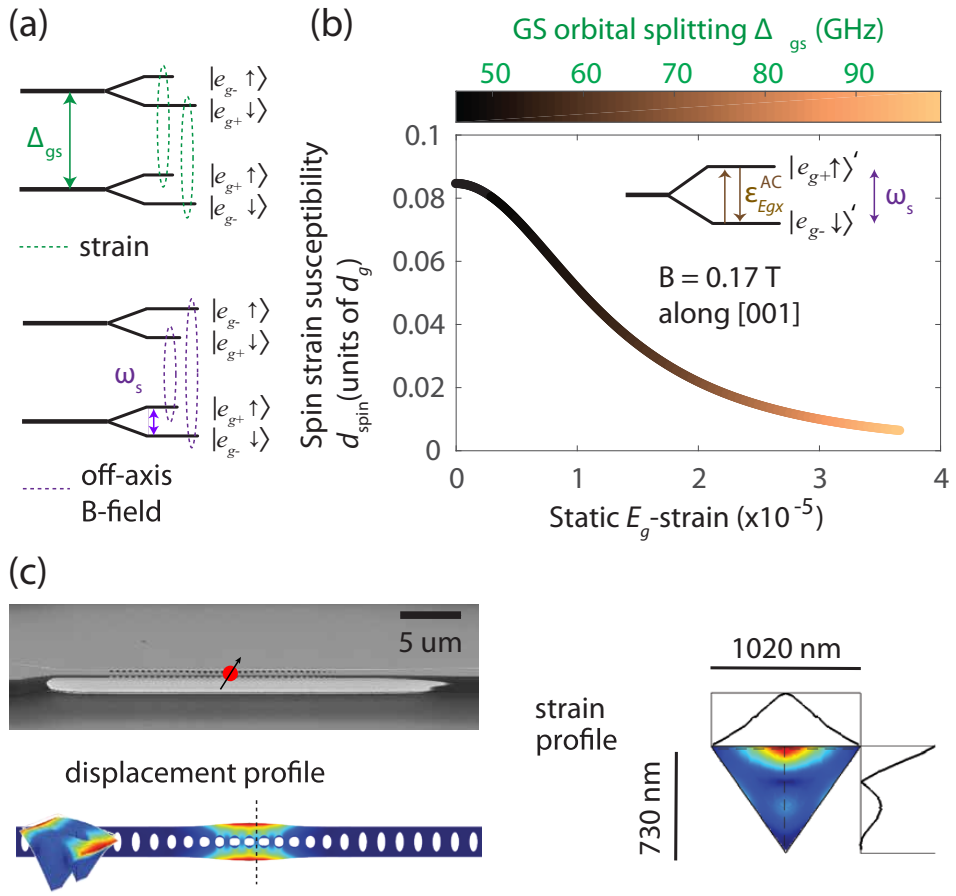

Figure 5.2: (a) Illustration of mixing terms introduced by E_g-strain and an off-axis magnetic field in the GS manifold. (b) Calculated susceptibility of the qubit for interaction with AC E_g-strain resonant with the transition frequency ω_s (interaction shown in inset). This AC strain susceptibility is maximum at zero strain for the pure SO eigenstates. At high strain, it falls off as $1/\Delta_{\rm gs}$. Color variation along the curve shows the GS splitting $\Delta_{\rm gs}$ corresponding to the value of static E_g-strain at the SiV. Both the static and AC strain are assumed to be entirely in the E_{gx} component. (c) SEM image of an optomechanical crystal nanobeam cavity[84] along with an FEM simulation of its 5 GHz flapping resonance. Displacement profile and a cross-sectional strain profile of the mode are shown with arbitrary normalization.

The effects of various modes of strain and the rich electronic structure of the SiV allow a variety of spin-phonon coupling schemes. Here, we focus on direct coupling of the spin transition to a mechanical resonator at frequency ω_s enabled by E_g-strain response of the spin discussed in the previous section. An alternative approach utilizing propagating phonons of frequency $\sim \lambda_{\rm SO}$ coupled to the GS orbital transition is discussed in Chapter 7. Our scheme would require diamond mechanical resonators of frequency $\omega_s \sim$ few

GHz, which have already been realized in both optomechanical[84,130] and electromechanical platforms[69,70,131,132]. Fig. 5.2(c) shows the strain profile resulting from GHz frequency mechanical modes in an optomechanical crystal cavity. Since this structure achieves three-dimensional confinement of phonons on the scale of the acoustic wavelength, it provides large per-phonon strain. For an SiV located ∼20 nm below the top surface, when a magnetic field $B = 0.3$ T is applied along the [001] direction, the qubit levels are resonant with the 5 GHz flapping mode, and has a single-phonon coupling rate $g \sim 0.8$ MHz. In order to achieve this maximal value of g, SiV centers can be generated in the high strain region of the resonator by previously demonstrated targeted ion implantation techniques[56,13,133].

At mK temperatures, given the low SiV spin dephasing rate $\gamma_s \sim 100$ Hz[61], even modest mechanical quality-factors $Q_m \sim 10^3$ are sufficient to achieve strong spin-phonon coupling. In fact, recent results from GHz frequency silicon phononic crystal resonators at mK temperatures show Q-factors in the tens of billions corresponding to damping rates ∼0.1 Hz and dephasing rates κ ∼10 KHz[24]. An SiV center located in such a cavity will be deep in the strong coupling regime with g exceeding both spin and mechanical dephasing processes by several orders of magnitude. At 4 K, despite the higher spin dephasing rate $\gamma_s \sim 4$ MHz[116,58] and thermal occupation of mechanical modes $n_{th} \sim 20$, spin-phonon cooperativity ~ 1 can be achieved with Q-factors of order $Q_m \sim 10^5$ which we will demonstrate in Chapter 6. We note that this form of spin-phonon coupling can also be implemented in other resonator designs such as surface acoustic wave cavities[131,132,134], wherein piezoelectric materials are used to transduce the mechanical motion with microwave electrical signals instead of optical fields.

Chapter 6

Diamond phononic crystals at cryogenic temperatures

In this chapter, we discuss phononic crystal resonators in diamond towards realizing a coherent spin-phonon interface with the SiV center. We present optomechanical crystal (OMC) cavities in diamond[84] that localize highly confined, coupled optical and mechanical modes. These devices were developed following pioneering demonstrations in silicon[135] motivated by the presence of color centers that could act as acoustic two level systems. In our experiments, the optical cavity allows sensitive transduction of mechanical motion and determination of the mechanical frequency before searching for signatures of resonant electron-phonon coupling between the SiV and the mechanical mode. The results at this point are somewhat preliminary. We mainly show high Q-factor GHz frequency mechanical modes in these structures, sufficient to achieve co-operativity $\sim$1 at 4 K and $\gg$1 at 100 mK. We also discuss 4 K measurements that would allow characterization of the resonant single phonon coupling rate g to the SiV qubit.

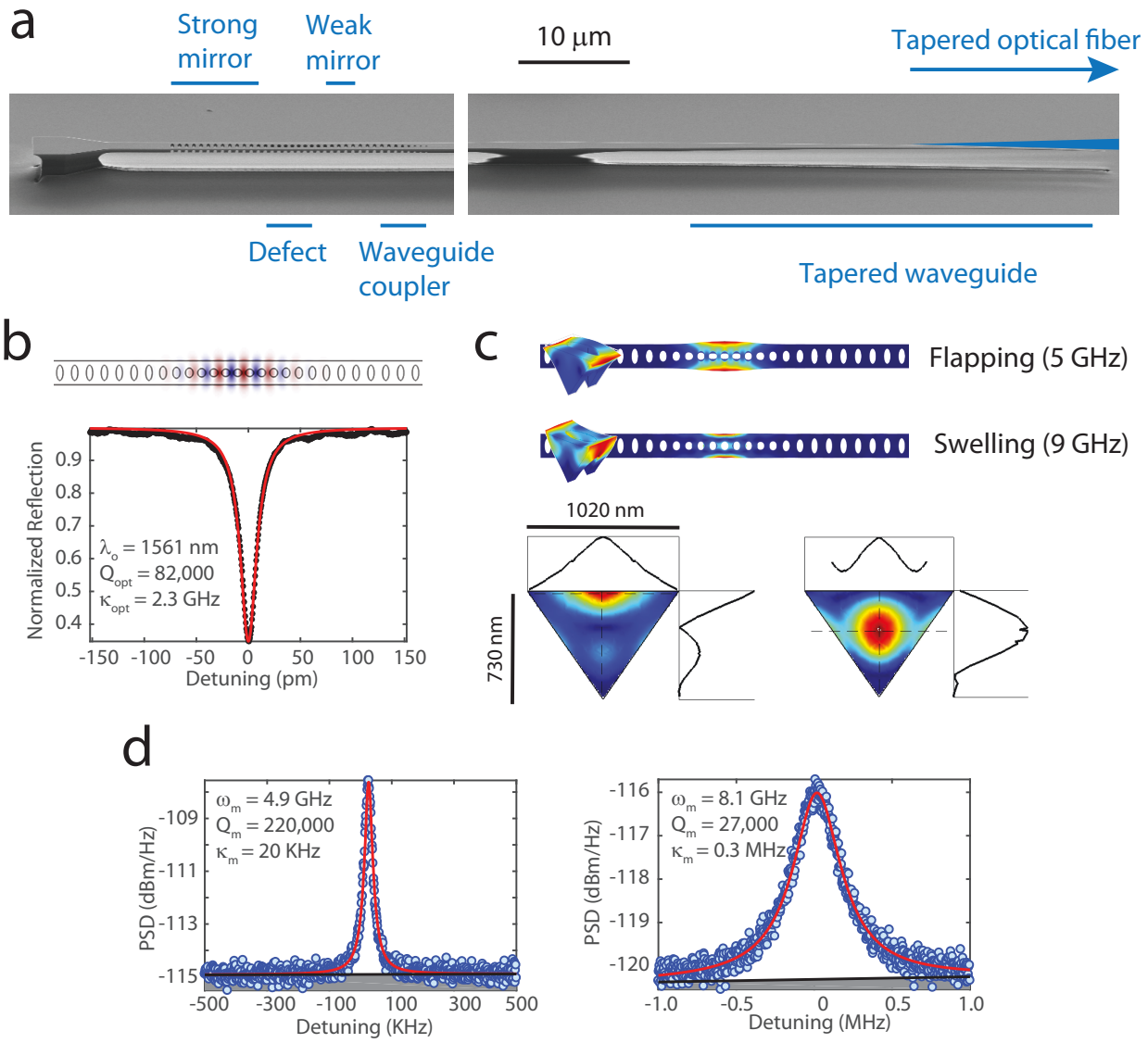

Figure 6.1: OMC spectra at 4 K(a) SEM images of OMC device showing various sections relevant to the photonic design of the device. (b) Optical reflection spectrum showing the high Q-factor fundamental TE mode of the device in the telecom C band. FEM calculation of the electric field intensity corresponding to this mode is sown (c) FEM simulation results of two even symmetry mechanical modes with large optomechanical coupling, the flapping and swelling modes. Top panels show displacement profiles and bottom panels show strain profile through a vertical cross-section of the device (d) Power spectral densities of thermal motion of flapping mode (left) and swelling mode (right panel) transduced by the optical cavity

6.1 Optomechanical crystal cavities

The 1D OMC devices (Figure 6.1a) used in our experiments are designed to co-localize an optical mode at telecom wavelengths (Figure 6.1b) and GHz frequency acoustic modes (Figure 6.1c). They were fabricated by Faraday cage angled etching developed previously[41]. Detailed discussion of the optical and acoustic band structure of triangular cross section OMCs is provided in[84]. In addition, the device shown in Figure 6.1a has a 1D phononic bandgap mirror section on the left hand side with a bandgap for all acoustic polarizations at 5 GHz. This section is included to reduce damping of the flapping mode shown in Figure 6.1c due to leakage of acoustic energy into the bulk through propagating modes of the OMC at 5 GHz. While these propagating modes are, by design, orthogonal to the defect mode, they may weakly couple due to fabrication-induced disorder that breaks the symmetry properties of the device[24,136]. The devices are designed to be optically probed in reflection mode with a large number of photonic crystal periods forming a strong mirror on the reflective end (left hand side of Figure 6.1a) and a smaller number of periods forming a weaker mirror on the transmissive end (right hand side of Figure 6.1a). The transmissive end also has a section of tapered holes to adiabatically transfer the cavity mode into a waveguide mode with low scattering loss. The diamond waveguide is then gradually tapered to a point over a length of tens of microns to form a coupling section for a tapered optical fiber which is parked on this section during measurements[19]. This is similar to the fiber coupling approach used in Chapter 3 to collect SiV fluorescence with the minor difference that we use a single mode optical fiber at telecom wavelengths instead. The experiments are carried in a closed cycle helium cryostat at 4K (Appendix I.1).

Our devices feature high Q-factor optical modes (Figure 6.1c) that place us in the resolved sideband regime of cavity optomechanics. We observe two high Q mechanical modes of the structure (Figure 6.1d) by probing the RF power spectrum of light reflected off the cavity, when the laser is optimally blue detuned from the optical resonance at a detuning corresponding to these modes. In these measurements, the laser power is kept sufficiently

low to avoid linewidth narrowing of the mechanical mode from optomechanical backaction[20]. The modes correspond to the flapping and swelling modes of the structure at ∼5 GHz and ∼8 GHz respectively shown in shown in Figure 6.1c, close to the design values in FEM simulations. The Q-factor of the flapping mode in particular is comparable to state-of-the-art silicon OMCs at 4 K[137]. The cross-sectional strain profiles in the center of the resonator for both modes are shown in Fig. 6.1c. Using the off-axis magnetic field coupling scheme outlined in Chapter 5, we estimate that a resonant single phonon coupling rate g of 0.8 MHz and 1.9 MHz can be achieved with these modes. This requires B-fields of 0.31 T and 0.47 T respctively aligned along the [001] crystal axis tune the lowest two spin-orbit ground states of the SiV into resonance with these modes. For the purpose of these estimates, it is also assumed that the SiV experiences zero static strain and is situated at a depth of 50 nm from the surface for the flapping mode, and at the strain maximum in the device center for the swelling mode. The presence of static strain will reduce the coupling rate g according to the scaling of the strain susceptibility shown in Figure 5.2b.

6.2 SiV centers in optomechanical crystals

More recently, we have fabricated OMCs with rectangular cross-section via isotropic etching of diamond (Fig. 6.2a)[43,138]. Prior to device patterning, we implant silicon ions through apertures patterned at locations corresponding to the two central fins of the cavity where the strain from the ∼9 GHz breathing mode of the structure[135] is maximum (Fig. 6.2b). The masked implantation procedure followed is similar to the one used in Chapter 3 with the difference that we implant before device patterning to avoid reduction in mechanical Q-factors from high temperature annealing employed to generate SiV centers. In our devices, we observe breathing modes with Q-factors in the few ten thousands as seen in Fig. 6.2c. The order of magnitude reduction in mechanical Q factor compared to the angle etched devices in Fig. 6.1 is most likely due to imperfect etching on the underside of the

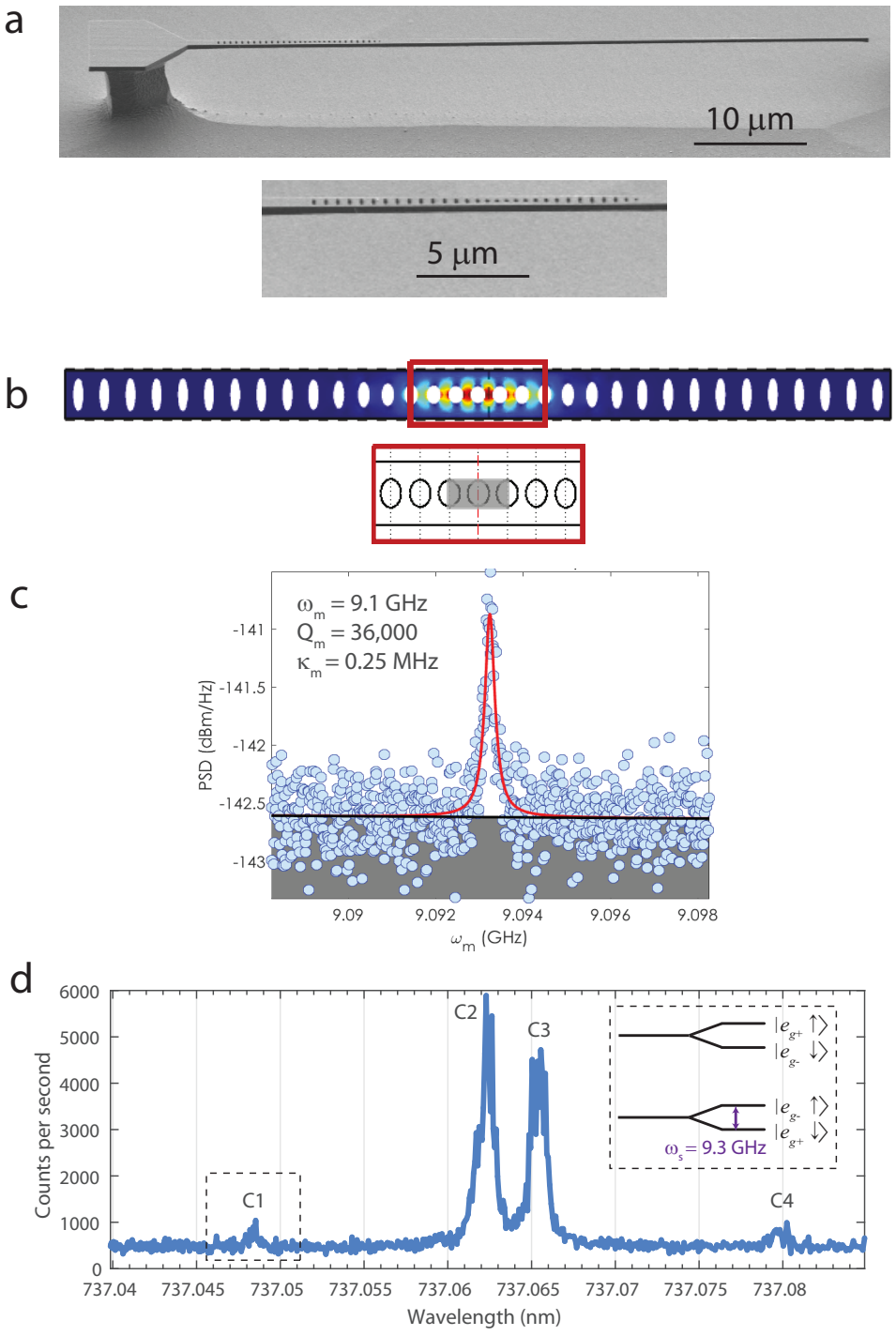

Figure 6.2: Isotropically etched OMCs (a) SEM image showing rectangular cross section OMCs (b) Spatial dsitribution of strain for the 9 GHz breathing mode. Zoom-in showing illustration of aperture for ion implantation (grey region) (c) Power spectrum of the 9 GHz breathing mode taken at 4 K (d) Resonant excitation spectrum of the C transitions of an SiV in the device with magnetic field tuned such that ω_s=9.3/,GHz

beams, which could induce scattering into propagating modes of the device. These results correspond to the first iteration of devices from the isotropic etch, and we are optimistic that Q-factors can be improved over subsequent runs through optimization of the etch parameters. The spin-phonon coupling rate g is expected to be of the same order of magnitude as in the triangular cross section beams, but robust to variations in SiV depth since the breathing mode has a strain profile that is invariant along the vertical direction (into the page in Fig. 6.2b). Fig. 6.2d shows the C transitions of an SiV in this device with its qubit frequency tuned close to the mechanical frequency. We now list measurements that could be performed at 4 K to infer the spin-phonon coupling rate g.

Detection of the mechanical mode in SiV fluorescence: The presence of a mechanical resonator close to the qubit frequency ω_s introduces a single phonon relaxation mechanism resonantly enhanced by the mechanical mode. This process, analogous to Purcell enhancement in optics, can be much faster than the usual two phonon process involving the upper orbital branch described in Chapter 4. Specifically, we expect the modified relaxation rate

$$\Gamma_s' = \Gamma_s + n_{\text{th}} g^2 \frac{\gamma}{\gamma^2/4 + (\omega_s - \omega_m)^2} \tag{6.1}$$

Here Γ_s is the bare relaxation rate of the SiV spin, $\sim$0.4 MHz for a low strain SiV at 4 K with magnetic field aligned along the [001] crystal axis[60] and γ is the spin dephasing rate. When the spin and mechanical mode are exactly in resonance, the resonator-induced thermalization is $4n_{\text{th}}g^2/\gamma \sim 25\Gamma_s$ assuming $g \sim 1$ MHz. Note that the bandwidth for resonator enhanced thermalization is determined by $\gamma \gg \kappa$. This should lead to a substantial enhancement in the resonance fluorescence off one of the optical transitions eg. C1 as the qubit frequency ω_s is swept across the mechanical resonance ω_m. In Appendix I.4, we show an attempt at this measurement.

EIT in the SiV ODMR spectrum: The most direct estimate of co-operativity could be achieved by inferring the depth of an EIT dip formed in the ODMR spectrum of the qubit transition due to the mechanical mode. The physics of this effect is illustrated in

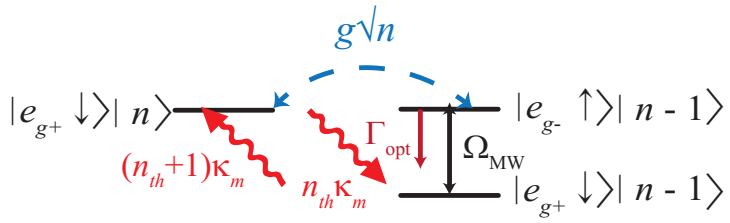

Figure 6.3: Schematic for EIT in an ODMR measurement of the spin-resonator system

Fig. 6.3, wherein a microwave drive Ω_{MW} drives the qubit transition while one of the levels is being read out with a laser at the rate Γ_{opt}. Spin and mechanical excitations are exchanged resonantly at the rate $g\sqrt{n}$. Since the resonator is long-lived compared to the qubit i.e. $\kappa \ll \gamma$, the spin excitation is shelved in the mechanical mode leading to a dip in the ODMR spectrum. This effect is analogous to dipole induced transparency in cavity QED[139] with the interesting difference that the dark state in our case corresponds to the resonator being excited instead of the atom. This occurs due to the parameter ordering $\gamma \gg g \gg \kappa$ i.e. the 'good cavity, bad atom' regime in contrast with the 'good atom, bad cavity' regime in cavity QED. The extent of the dip scales as $1/(1 + 4g^2/\kappa\gamma)$ with the thermal occupation of the mechanical mode n_{th} dropping out since this can be viewed as a classical effect arising from two coupled oscillators[140]. Mathematically, in Fig. 6.3, faster damping $\sim n\kappa$ of the state $|n\rangle$ is compensated for by stronger driving $\sim \sqrt{n}g$ out of it.

Chapter 7

Phonon networks with silicon vacancy centers

In this chapter, we propose and analyze a novel realization of a solid-state quantum network, where SiV centers are coupled via the phonon modes of a quasi-1D diamond waveguide. Quantum states can be encoded in long-lived superpositions of the two lowest spin-orbit states, the same qubit discussed in previous chapters, while a controlled admixing of higher orbital states, which are susceptible to strain, gives rise to a strong and tunable coupling to phonons. As a result, the qubit state can be converted into a propagating phonon wavepacket and be reabsorbed efficiently by a distant SiV. Our analysis shows that high fidelty state transfer can be achieved with realistic experimental parameters. Apart from quantum information processing, this setup constitutes a novel waveguide QED platform, where strong-coupling effects between solid-state defects and individual propagating phonons can be explored at the quantum level.

7.1 Model

We consider a system as depicted in Fig. 7.1, where an array of SiV centers is embedded in a 1D diamond waveguide. In contrast with the direct qubit-phonon coupling discussed in

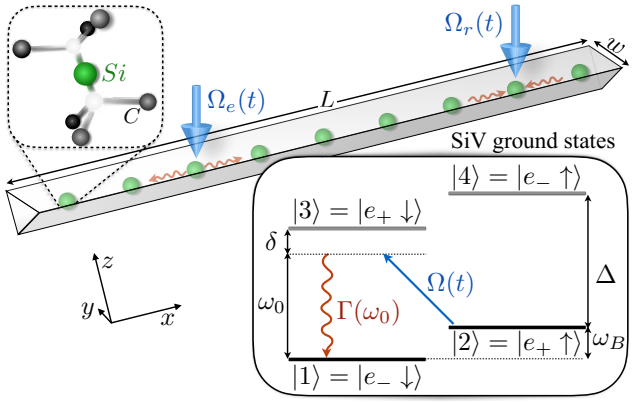

Figure 7.1: An array of SiV defects is embedded in a 1D phonon waveguide. The inset shows the level structure of the electronic ground state of the SiV center. A tunable Raman process involving the excited state $|3\rangle$ is used to coherently convert the population of the stable state $|2\rangle$ into a propagating phonon, which can be reabsorbed by any other selected center along the waveguide.

Chapters 5, 6, here we will study a Raman scheme implemented with a driving field (inset of Fig. 7.1) that will allow us to control the coupling to propagating phonons. With the notation $\{|1\rangle \simeq |e_-, \downarrow\rangle, |2\rangle \simeq |e_+, \uparrow\rangle\}$ and $\{|3\rangle \simeq |e_+, \downarrow\rangle, |4\rangle \simeq |e_-, \uparrow\rangle\}$ for the GS spin-orbit eigenstates separated by $\Delta/2\pi \simeq 46$ GHz[53], we have the following Hamiltonian for a single SiV center in this setting.

$$\begin{aligned} H_{\text{SiV}} &= \omega_B |2\rangle\langle 2| + \Delta |3\rangle\langle 3| + (\Delta + \omega_B)|4\rangle\langle 4| \\ &+ \frac{1}{2}\left[\Omega(t) e^{i[\omega_d t + \theta(t)]} \left(|2\rangle\langle 3| + |1\rangle\langle 4|\right) + \text{H.c.}\right], \end{aligned} \tag{7.1}$$

where a magnetic field $\vec{B} = B_0 \vec{e}_z$ is applied purely along the SiV axis. $\omega_B = \gamma_s B_0$ and γ_s is the spin gyromagnetic ratio. The time-dependent driving field with a tunable Rabi-frequency $\Omega(t)$ and phase $\theta(t)$ couples the lower and upper states of opposite spin. This coupling can be implemented either directly with a microwave field of frequency $\omega_d \sim \Delta$[141], or indirectly via an equivalent optical Raman process. The latter method is already used in experiments to initialize and prepare individual SiV centers in superpositions of $|1\rangle$ and $|2\rangle$[58,142].

For the waveguide, we consider a quasi-1D geometry of width w and length $L \gg w$. In

the frequency range of interest ($\omega/(2\pi) \sim \Delta/2\pi \simeq 46$ GHz), the waveguide supports travelling phonon modes of frequency $\omega_{n,k}$ and mode function $\vec{u}_{n,k}(\vec{r}) \sim \vec{u}^{\perp}_{n,k}(y,z)e^{ikx}$, where k is the wavevector along the waveguide direction, n is the branch index and $\vec{u}^{\perp}_{n,k}(y,z)$ is the transverse profile of the displacement field. The phonons induce transitions between the orbital states $|e_{g\pm}\rangle$, and the Hamiltonian for the whole system reads

$$\begin{aligned} H = &\sum_j H^{(j)}_{\mathrm{SiV}} + \sum_{n,k} \omega_{n,k} a^{\dagger}_{n,k} a_{n,k} \\ &+ \frac{1}{\sqrt{L}} \sum_{j,k,n} \left(g^j_{n,k} J^j_+ a_{n,k} e^{ikx_j} + \mathrm{H.c.} \right). \end{aligned} \tag{7.2}$$

Here j labels the SiV centers located at positions $\vec{r}_j = (x_j, y_j, z_j)$, $J_- = (J_+)^{\dagger} = |1\rangle\langle 3| + |2\rangle\langle 4|$ is the spin-conserving lowering operator and $a_{n,k}$ ($a^{\dagger}_{n,k}$) are the annihilation (creation) operators for the phonon modes. The couplings $g^j_{n,k} \equiv g_{n,k}(y_j, z_j)$ depend on the components of the local strain tensor,
$\epsilon^{ab}_{n,k}(\vec{r}_j) = \frac{1}{2}[\frac{\partial}{\partial x_b} u^a_{n,k}(\vec{r}_j) + \frac{\partial}{\partial x_a} u^b_{n,k}(\vec{r}_j)]$, and can be evaluated for a known transverse mode profile $\vec{u}^{\perp}_n(y,z)$[143,144]. We express the resulting couplings as

$$g^j_{n,k} = d\sqrt{\frac{\hbar k^2}{2\rho A \omega_{n,k}}} \xi_{n,k}(y_j, z_j), \tag{7.3}$$

where $d/2\pi \sim 1$ PHz is the strain sensitivity of the orbital states measured in Chapter 2, ρ the density and A the transverse area of the waveguide. The dimensionless coupling profile $\xi_{n,k}(y,z)$ accounts for the specific strain distribution and $\xi(y,z) = 1$ for a homogeneous compression mode.

7.2 From cavity to waveguide QED

For small structures, $L \sim 10 - 100\,\mu$m, $w \lesssim 200$ nm, and group velocities $v \sim 10^4$ m/s, the individual phonon modes are well separated in frequency, $\Delta\omega/2\pi \gtrsim 50$ MHz, and the SiV

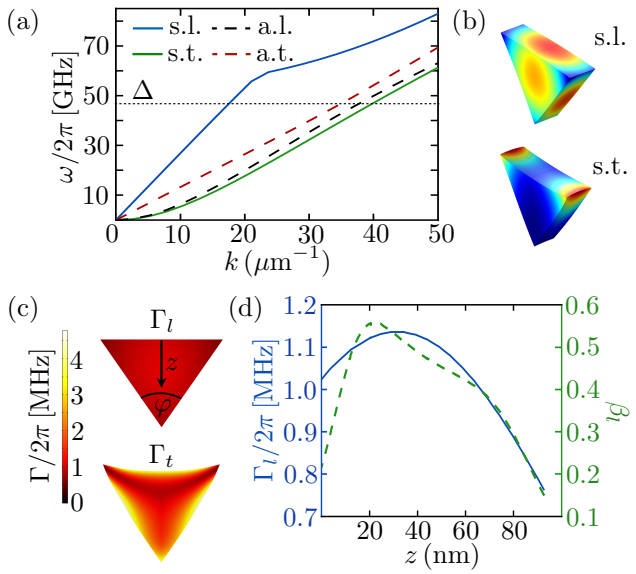

Figure 7.2: Phonon waveguide. (a) Acoustic dispersion relation for a triangular waveguide of width $w = 130$ nm and etch-angle $\varphi = 35^o$. Symmetric (solid lines) and anti-symmetric (dashed lines) branches with respect to the vertical mirror-symmetry plane are shown. (b) Normalized displacement profiles of the symmetric phonons at 46 GHz. (c) The emission rates into the symmetric longitudinal (Γ_l) and transverse (Γ_t) polarization modes at 46 GHz are plotted for different positions of the SiV center within the triangular cross-section. (d) Γ_l and fraction (β_l) of spontaneous emission into the longitudinal branch for different positions of the SiV center along the vertical mirror-symmetry axis. For all results, an orientation of the waveguide along the [110] crystal axis of diamond and SiV centers oriented along $[\bar{1}11]$ and $[1\bar{1}1]$, i.e., orthogonal to the waveguide axis, have been assumed.

centers can be coupled to a single standing-wave mode with a strength $g_L = g_0\sqrt{\lambda/L} \approx 2\pi \times (4-14)$ MHz, where $g_0/2\pi \approx 105$ MHz and $\lambda \approx 200$ nm is the phonon wavelength. The system dynamics is then governed by a Jaynes-Cummings-type interaction between phonons and orbital states. In the strong coupling regime, $g_L > \kappa = \Delta/Q$, which is reached for moderate mechanical quality factors of $Q > 10^4$, a coherent exchange of phonons and defect excitations becomes possible. For longer waveguides, the coupling to the quasi-continuum of phonon modes is characterized by the resulting decay rate $\Gamma_j(\Delta) = \sum_n \Gamma_{j,n}(\Delta)$ for states $|3\rangle$ and $|4\rangle$, where

$$\Gamma_{j,n}(\omega) = \lim_{L\to\infty} \frac{2\pi}{L} \sum_k |g^j_{n,k}|^2 \delta(\omega - \omega_{n,k}). \tag{7.4}$$

For a single compression mode with $\vec{u}^{\perp}(y,z) \sim \vec{x}$ and a linear dispersion $\omega_k = vk$, we obtain $\Gamma(\omega) = d^2\hbar\omega/(\rho A v^3)$, which results in a characteristic phonon emission rate of $\Gamma(\Delta)/2\pi \sim 1$ MHz[145].

Figure 7.2 summarizes the simulated acoustic dispersion relations and the resulting decay rates for a triangular cross-section waveguide[46] of width $w = 130$ nm. The SiV centers couple primarily to a longitudinal (l) compression and a transverse (t) flexural mode with group velocities $v_l = 1.71 \times 10^4$ m/s and $v_t = 0.73 \times 10^4$ m/s, respectively. The coupling to the other two branches of odd symmetry can be neglected for defects near the center of the waveguide. Fig. 7.2(c) and (d) show that the rates $\Gamma_{l,t}$ are quite insensitive to the exact location of the SiV center. However, the fraction of phonons emitted into a specific branch, $\beta_n = \Gamma_n/\Gamma$, is significantly below unity as emission is split between a pair of modes. In optical waveguides[146], a value of $\beta < 1$ usually arises from the emission of photons into non-guided modes, which are irreversibly lost. For a phonon waveguide this is not the case, but the multi-branch nature of the waveguide must be fully taken into account. In all examples below we assume $\beta_l = \beta_t = 0.5$, which is most relevant for SiV defects located near the center of the beam.

7.3 Generation of a coherent phonon wavepacket

We are interested in the transfer of a qubit state, encoded into the stable states $|1\rangle$ and $|2\rangle$, between an arbitrary pair of emitting (e) and receiving (r) defects in the waveguide,

$$(\alpha|1\rangle_e + \beta|2\rangle_e)|1\rangle_r \rightarrow |1\rangle_e(\alpha|1\rangle_r + \beta|2\rangle_r). \tag{7.5}$$

As shown in Fig. 7.1, this can be achieved by inducing a Raman transition via state $|3\rangle_e$ to convert the population in state $|2\rangle_e$ into a propagating phonon and by reverting the process at the receiving center. For low enough temperatures, $T \ll \hbar\Delta/k_B \approx 2.2$ K, such that all phonon modes are initially in the vacuum state, this scenario is described by the following ansatz for the wavefunction $|\psi(t)\rangle = [\alpha 1 + \beta C^\dagger(t)]|\bar{1}, 0\rangle$, where $|\bar{1}, 0\rangle$ is the ground state with all SiV centers in state $|1\rangle$. $C^\dagger(t)$ written out below is the creation operator for a single excitation distributed between the SiV centers and the phonon modes.

$$C^\dagger(t) = \sum_{j=e,r} \left[c_j(t)e^{-i\omega_B t}|2\rangle_j\langle 1| + b_j(t)e^{-i\omega_0 t}|3\rangle_j\langle 1| + \sum_{n,k} c_{n,k}(t)e^{-i\omega_0 t}a^\dagger_{n,k}\right] \tag{7.6}$$

The central phonon frequency $\omega_0 = \Delta_j + \delta_j$ is assumed to be fixed by compensating small inhomogeneities in the Δ_j by the detunings $\delta_j = \omega_d^j - (\Delta_j - \omega_B^j)$.

By adiabatically eliminating the fast decaying amplitudes b_j, we derive effective equations of motion for the slowly varying amplitudes $c_i(t)$. From this derivation, detailed in[144], we obtain for each qubit amplitude

$$\dot{c}_j(t) = -\frac{\gamma_j(t)}{2}c_j(t) - \sum_n \sqrt{\frac{\gamma_{j,n}(t)}{2}}e^{-i\theta_j(t)}\Phi^{\text{in}}_{j,n}(t), \tag{7.7}$$

where $\gamma_j(t) = \sum_n \gamma_{j,n}(t)$ is the effective decay rate of state $|2\rangle_j$ and

$$\gamma_{j,n}(t) = \frac{\Omega_j^2(t)}{4\delta_j^2 + \Gamma_j^2(\omega_0)}\Gamma_{j,n}(\omega_0). \tag{7.8}$$

Assuming $0 \leq \Omega(t)/2\pi < 70$ MHz and $\delta/2\pi = 100$ MHz, this rate can be tuned between $\gamma_j = 0$ and a maximal value of $\gamma_{\max}/2\pi \approx 250$ kHz, which is still fast compared to the expected bare dephasing times $T_2^* = 10 - 100\,\mu$s of the qubit state [61]. At the same time, the large detuning $\delta \gg \Gamma(\Delta)$ ensures that any residual scattering of phonons from an undriven defect is strongly suppressed.

The last term in Eq. (7.7), where $\Phi_{j,n}^{\text{in}} = \Phi_{j,n}^{\text{in,L}} + \Phi_{j,n}^{\text{in,R}}$, describes the coupling of an SiV center to the left- (L) and right- (R) incoming fields $\Phi_{j,n}^{\text{in,R/L}}$, which themselves are related to the corresponding outgoing fields by[147]

$$\Phi_{j,n}^{\text{out,R/L}}(t) = \Phi_{j,n}^{\text{in,R/L}}(t) + \sqrt{\frac{\gamma_{j,n}(t)}{2}} c_j(t) e^{i\theta_j(t)}. \tag{7.9}$$

Together with Eq. (7.7), these input-output relations specify the local dynamics at each node and must be supplemented by a set of propagation relations for all fields [cf. Fig. 7.3(a)]. As an example, for $x_r > x_e$, the right propagating fields obey $\Phi_{r,n}^{\text{in,R}}(t) = \Phi_{e,n}^{\text{out,R}}(t - \tau_{er}^n) e^{i\phi_{er}^n}$, where $\tau_{er}^n = (x_r - x_e)/v_n$ and $\phi_{er}^n = k_n(x_r - x_e)$ are the respective propagation times and phases. Reflections at the boundaries lead to a retarded interaction of each center with its own emitted field. For example, $\Phi_{e,n}^{\text{in,R}}(t) = -\sqrt{R_n}\Phi_{e,n}^{\text{out,L}}(t - \tau_e^n) e^{i\phi_e^n}$, where $\tau_e^n = 2x_e/v_n$ and $\phi_e^n = 2k_n x_e$, and the reflectivity $R_n \leq 1$ has been introduced to model losses. The combined set of time-nonlocal equations for the SiV amplitudes can be solved numerically for given positions x_j and pulses $\gamma_{j,n}(t)$. Since any deterministic phase acquired during the protocol can be undone by a local qubit rotation, we identify $\mathcal{F}(t) = |c_r(t)|^2$ with the fidelity of the transfer, which exceeds the classical bound for $\mathcal{F} > 2/3$[148].

7.4 Quantum state transfer

In Fig. 7.3(b) we first consider constant rates $\gamma_{j,n}(t) = \gamma_{\max}/2$, in which case a state transfer is achieved over multiple round-trips of the emitted wave-packet. For $L \sim 100\,\mu$m, the round-trip times $2L/v_n$ are still short compared to $\gamma_{\max}^{-1}$ and we recover the standing-wave

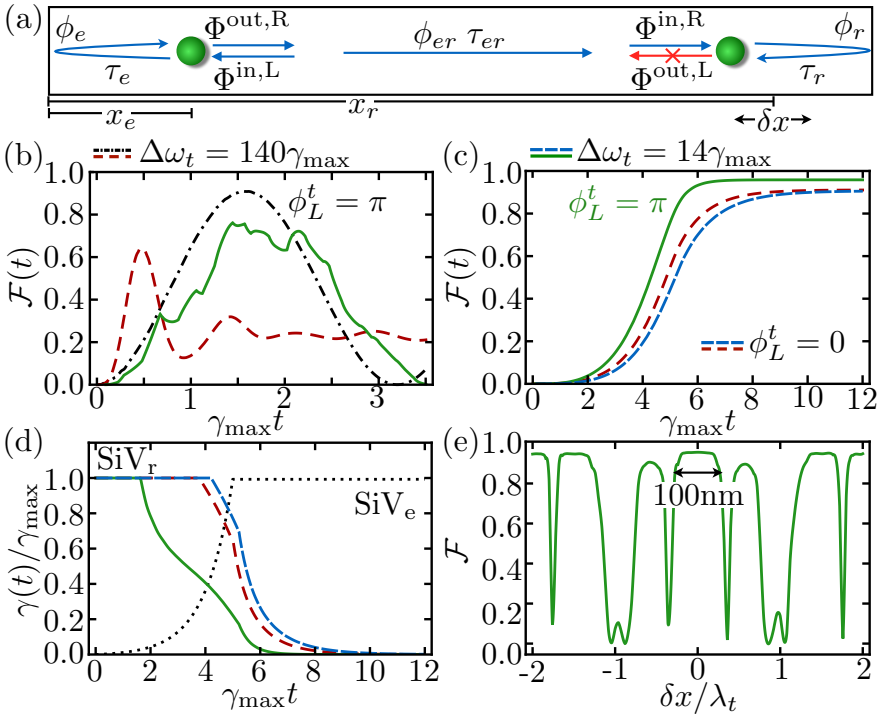

Figure 7.3: State transfer protocol. (a) Schematics showing the relevant fields, retardation times and propagation phases. (b) State transfer fidelity for constant rates $\gamma_e(t) = \gamma_r(t) = \gamma_{\rm max}$. The case of a single resonant mode (red dashed line; $\phi_L^t = 0$, $\phi_L^l = \pi$) is compared to the off-resonant case (dot-dashed black line; $\phi_L^t = \phi_L^l = \pi$) for $L \sim 100\,\mu$m ($\Delta\omega_t/\gamma_{\rm max} = 140$). The full green line represents the long-waveguide counterpart of the off-resonant scenario, where $L \sim 1$ mm ($\Delta\omega/\gamma_{\rm max} = 14$). (c)-(d) Protocol using slowly-varying control pulses ($t_p\gamma_{\rm max} = 1$) where $\Phi_{r,t}^{\rm out,L}(t)$ is completely suppressed. The dashed blue line corresponds to the long waveguide counter part of the dashed red line. For (b)-(d), the two defects are equally coupled to both modes, $\phi_e^n = \phi_r^n = \pi$ and $\beta_e^n = \beta_r^n = 0.5$. (e) Plot of the state transfer fidelity for varying positions of the receiving SiV center. For this plot $\phi_L^t = \phi_L^l = \pi$ and a maximal transfer time of $12\gamma_{\rm max}^{-1}$ have been assumed. In all plots, we considered defects near the boundaries where $\tau_e = \tau_r \approx 0$. To illustrate the effect of phonon losses a boundary reflectivity of $R = 0.92$ has been assumed, which corresponds to $Q \approx 5 \times 10^4$ in the cavity limit.

picture with splittings $\Delta\omega_n = \pi v_n/L$ between consecutive k-modes. When only the transverse mode is resonant, [i.e., $\phi_L^t = \phi_e^t + \phi_r^t + 2\phi_{er}^t = 2\pi n$, while $\phi_L^l = (2m+1)\pi$] and for maximal coupling [$\phi_e^l = \phi_r^l = (2m+1)\pi$], we observe damped oscillations with a fast frequency $\tilde{g} = \sqrt{\gamma_{\max}\Delta\omega_t/2\pi} \approx 2\pi \times 1.2$ MHz and decay rate $\kappa = -\frac{\Delta\omega}{\pi}\log R \approx 2\pi \times 0.93$ MHz. This result is expected from a single-mode description of the waveguide[144], and is recovered here as a limiting case of our general framework. The losses from multiple imperfect reflections at the boundaries can be partially suppressed at the expense of a slightly slower transfer by detuning the SiV centers from the closest mode by $\delta_0 > \tilde{g}$. In this case the SiV centers communicate via an exchange of virtual phonons and $\kappa \to \kappa(\tilde{g}/\delta_0)^2$. For a maximal detuning $\delta_0 = \Delta\omega_t/2$, the transfer fidelity scales approximately as $\mathcal{F} \simeq R - \pi^2/(8T_2^*\gamma_{\max})$[110]. For $T_2^* \approx 100\mu$s and $R > 0.99$, which can be achieved, for example, by phononic Bragg mirrors[84], gate fidelities of $\mathcal{F} \gtrsim 0.99$ are possible.

As illustrated by the solid line in Fig. 7.3(b), the simple cavity picture fails for longer waveguides, where multi-mode and propagation effects become non-negligible. In Fig. 7.3(c) we illustrate a more general and more robust protocol, where the phonons ideally travel the waveguide only once. Here, the emission is gradually turned on with a fixed pulse $\gamma_e(t)/\gamma_{\max} = \min\{1, e^{(t-5t_p)/t_p}\}$, while $\gamma_r(t)$ and $\theta_r(t)$ are constructed numerically by minimizing at every time step the back-reflected transverse field $|\Phi_{r,t}^{\mathrm{out,L}}|$. For slow pulses, $\gamma_{\max}t_p \gg 1$, a perfect destructive interference between the field reflected from the boundary and the field emitted by the receiving center can be achieved, i.e., $\Phi_{r,t}^{\mathrm{in,L}}(t) + \sqrt{\gamma_{r,t}(t)/2}c_r(t)e^{i\theta_r(t)} = 0$. For a single branch ($\beta_t = 1$) this results in a complete suppression of the signal traveling back to the emitting center so that for $R = 1$ and negligible retardation effects, a perfect state transfer can be implemented[98,149,150,151]. Fig. 7.3(c) shows that this approach also leads to high transfer fidelities under more general conditions, where all propagation effects are taken into account and multiple independent channels participate in the transfer. Importantly, since there are no resonances building up, this strategy is independent of L and can be applied for short and long waveguides equally well.

In the examples shown in Fig. 7.3(b)-(d), the SiV centers are placed at positions near the ends of the waveguide, where the effective emission rate $\tilde{\gamma}_{j,n}(t) = 2\gamma_{j,n}(t)\sin^2(\phi_j^n/2)$ [152] into both modes is maximal. Fig. 7.3(e) shows the achievable transfer fidelities when the position of the receiving center is varied over several wavelengths. We observe plateaus of high fidelity extending over $\sim$ 100 nm, interrupted by a few sharp dips arising from a complete destructive interference, i.e. $\phi_r \approx \pi$. This position insensitivity, even in a multi-channel scenario, can be understood from a more detailed inspection of the outgoing fields $\Phi_{r,l}^{\mathrm{out,L}}$ [144] and makes the transfer protocol consistent with uncertainties of $\delta x < 50$ nm achieved with state-of-the-art implantation techniques[13].

7.5 Conclusion

We have shown how an efficient coupling between individual SiV centers and propagating phonons in a diamond waveguide can be used to realize a chip scale quantum network. By employing direct spin-phonon couplings in the presence of a transverse magnetic field as discussed in Chapter 5 or defect-phonon interactions in other materials[33,125,153], many of the described techniques could also be adapted for lower phonon frequencies $\sim 5 - 10$ GHz, where advanced dispersion engineering techniques for phonons using phononic crystals are readily available. The use of phononic crystals in particular allows for single mode waveguides[154]. Control of phonon emission and absorption in this case could be achieved through local bias magnetic fields which tune the spins selectively in and out of resonance with a phononic band edge[155]. When combined with local control operations involving adjacent nuclear spins as quantum memories[156,157], the set of all these techniques provides a realistic approach for a scalable quantum information processing platform with spins in solids.

Appendix A

NV cantilever sample fabrication

Single crystal electronic grade bulk diamond chips (4mm x 4mm) from Element Six Ltd are implanted with ^{14}N ions at an implantation energy of 75 keV, and a dose of 6×10^{11} /cm^2. This yields an expected depth of 94 ± 19 nm calculated using software from Stopping and Range of Ions in Matter (SRIM). Subsequently, NVs are created by annealing the samples in high vacuum ($< 5 \times 10^{-7}$ torr). The temperature ramp sequence described in[74] is followed with a final temperature of 1200^{o}C, which is maintained for 2 hours. After the anneal, the samples are cleaned in a 1:1:1 boiling mixture of sulfuric, nitric and perchloric acids to remove a few nm of graphite generated on the surface from the anneal. Cantilevers are then patterned using e-beam lithography, and etched using reactive ion beam angled etching[92]. Post-fabrication, we repeat the tri-acid cleaning treatment to partially repair etch-induced damage, and perform a piranha clean to ensure a predominantly oxygen terminated diamond surface (diagnosed by X-ray photoelectron spectroscopy (XPS)), which is beneficial for NV photostability[74,75].

Appendix B

Silicon vacancy center: strain response theory

B.1 Group theoretical description of strain response

The response of the electronic levels of trigonal point-defects in cubic crystals to lattice deformations was treated theoretically by Hughes and Runciman[95]. A solution of this problem for the specific case of the SiV has been previously carried out using group theory[53] with some errors. Here, we reconcile these two treatments, and present a model for the response of the SiV electronic levels to strain (and stress). In what follows, we use x, y, z to refer to the internal basis of the SiV (see inset of Fig. 2.1(b). eg. for a [111] oriented SiV, we have $x : [\bar{1}\bar{1}2], y : [\bar{1}10], z : [111]$), and X, Y, Z to refer to the axes of the diamond crystal, i.e. $X : [100], Y : [010], Z : [001]$. We use σ and ϵ for the stress and strain tensors in the SiV basis, and $\bar{\sigma}$ and $\bar{\epsilon}$ to refer to them in the crystal basis. We also neglect the spin character of the states involved, since we are only concerned with changes to the Coulomb energy of the orbitals.

When the applied stress is small, in the Born-Oppenheimer approximation, the effect of lattice deformation is linear in the strain components and is captured by a Hamiltonian of

the form[95] -

$$\mathbb{H}^{\text{strain}} = \sum_{ij} V_{ij}\epsilon_{ij} \tag{B.1}$$

Here i, j are indices for the co-ordinate axes. V_{ij} are operators corresponding to particular stress components, and act on the SiV electronic levels. Group theory can be used to rewrite this Hamiltonian in terms of basis-independent linear combinations of strain components adapted to the symmetries of the SiV center. Each of these combinations can be viewed as a particular 'mode' of deformation, and the effect of each mode on the orbital wavefunctions, each with its own symmetries can be deduced using group theory. More technically, such deformation modes are obtained by projecting the strain tensor onto the irreducible representations of D_{3d}, the point group of the SiV center.[95] This transformation gives

$$\mathbb{H}^{\text{strain}} = \sum_{r} V_r\epsilon_r \tag{B.2}$$

where r runs over the irreducible representations. Deducing the operators V_r simply requires computing the direct products of irreducible representations.[53] It can be shown that strain and stress tensors transform as the irreducible representation, $A_{1g} + E_g$[53] which has even parity about the inversion center of the SiV. Since the ground states of the SiV transform as E_g (even), and the excited states transform as E_u (odd), lattice deformations do not couple the ground and excited states with each other to first order. As a result, we can describe the response of the ground and excited state manifolds independently. In particular, $\mathbb{H}^{\text{strain}}$ is identical in form for both manifolds, but will involve different numerical values of strain-response coefficients. Therefore, we drop the subscripts g and u used to refer to the ground and excited states, and simply work in the doubly-degenerate basis $\{|e_x\rangle, |e_y\rangle\}$. The interaction Hamiltonian can be shown to comprise three deformation

modes -

$$\mathbb{H}^{\text{strain}} = \alpha \begin{bmatrix} 1 & 0 \\ 0 & 1 \end{bmatrix} + \beta \begin{bmatrix} -1 & 0 \\ 0 & 1 \end{bmatrix} + \gamma \begin{bmatrix} 0 & 1 \\ 1 & 0 \end{bmatrix} \tag{B.3}$$

The components α, β, γ corresponding to ϵ_r in Eq.B.2 are given by the following linear combinations[95]

$$\begin{aligned} \alpha &= \mathscr{A}_1(\bar{\epsilon}_{XX} + \bar{\epsilon}_{YY} + \bar{\epsilon}_{ZZ}) + 2\mathscr{A}_2(\bar{\epsilon}_{YZ} + \bar{\epsilon}_{ZX} + \bar{\epsilon}_{XY}) \\ \beta &= \mathscr{B}(2\bar{\epsilon}_{ZZ} - \bar{\epsilon}_{XX} - \bar{\epsilon}_{YY}) + \mathscr{C}(2\bar{\epsilon}_{XY} - \bar{\epsilon}_{YZ} - \bar{\epsilon}_{ZX}) \\ \gamma &= \sqrt{3}\mathscr{B}(\bar{\epsilon}_{XX} - \bar{\epsilon}_{YY}) + \sqrt{3}\mathscr{C}(\bar{\epsilon}_{YZ} - \bar{\epsilon}_{ZX}) \end{aligned}$$

The coefficients $\mathscr{A}_1, \mathscr{A}_2, \mathscr{B}, \mathscr{C}$ completely determine the strain-response of the $\{|e_x\rangle, |e_y\rangle\}$ manifold. It can be shown that α transforms as A_{1g}, and $\{\beta, \gamma\}$ transform as $\{E_{gx}, E_{gy}\}$.

To gain more physical intuition for these three deformation modes, we can write α, β, γ in the SiV basis using the unitary transformation $R = R_z(45°)R_y(54.7°)$, where $R_z(\theta)$, and $R_y(\phi)$ correspond to rotations by θ and ϕ about the z- and y-axes respectively. Upon transformation, we get

$$\begin{aligned} \alpha &= t_\perp(\epsilon_{xx} + \epsilon_{yy}) + t_\parallel \epsilon_{zz} \equiv \epsilon_{A_{1g}} \\ \beta &= d(\epsilon_{xx} - \epsilon_{yy}) + f\epsilon_{zx} \equiv \epsilon_{E_{gx}} \\ \gamma &= -2d\epsilon_{xy} + f\epsilon_{yz} \equiv \epsilon_{E_{gy}} \end{aligned} \tag{B.4}$$

Here $t_\perp, t_\parallel, d, f$ are the four strain-susceptibility parameters. They are related to the original stress-response coefficients of Hughes and Runciman[95] according to the expressions in Table B.1. Further, to explicitly indicate the symmetries of these deformation

Table B.1: Various strain-modes, and their susceptibilities in terms of the Hughes-Runciman stress-response coefficients[95]. The constants c_{ij} are the elastic modulus components of diamond - c_{11}=1075 GPa, c_{12}=149 GPa, c_{44}=567 GPa[158].

Strain term	Susceptibility	Relation to Hughes-Runciman coefficients
$\epsilon_{xx}+\epsilon_{yy}$	$t_\perp$	$(c_{11}+2c_{12})A_1 - c_{44}A_2$
ϵ_{zz}	$t_\parallel$	$(c_{11}+2c_{12})A_1 + 2c_{44}A_2$
$\epsilon_{xx}-\epsilon_{yy}$	d	$(c_{11}-c_{12})B + c_{44}C$
ϵ_{xy}	$-2d$	
ϵ_{zx}	f	$\sqrt{2}\,(c_{44}C - 2(c_{11}-c_{12})B)$
ϵ_{yz}	f	

modes, we hereafter switch to the notation $\epsilon_{A_{1g}}$ for α, $\epsilon_{E_{gx}}$ for β, and $\epsilon_{E_{gy}}$ for γ in line with the description in Eq. (B.2).

At this juncture, we contrast Eqs. (B.4) with the recent results in Ref.[53] (Eqs. 2.80-2.82). Our analysis predicts a non-zero response to uniaxial strain along the high symmetry axis ϵ_{zz} in A_{1g} deformation, and to the shear strains ϵ_{zx} and ϵ_{yz} in E_g deformations. The origin of nonzero response to ϵ_{zz} in particular is discussed in the next section.

B.2 Extraction of strain susceptibilities

To extract all the values $\{t_\perp, t_\parallel, d, f\}$ for both ground and excited state manifolds, in principle, strain needs to be applied at least in three different directions for a given SiV. This procedure gives a set of overdetermined equations in these parameters.[95] However, the devices in this study can only induce two types of strain profiles as shown in Fig. 2.3(c) and (d). In particular, for a given SiV in either the 'axial' or the 'transverse' class, the relative ratio between strain-tensor components remains constant when voltage applied to the cantilever is swept. This condition makes it difficult to estimate the relative contributions of $t_\parallel$ and $t_\perp$ to $\epsilon_{A_{1g}}$, and of d and f to ϵ_{E_g}.

To get around this issue, we follow an approximate approach. From Fig. 2.3(d), we observe that in the case of an axial SiV, $\epsilon_{zz} \gg (\epsilon_{xx}+\epsilon_{yy})$ is always true. Therefore, we can use the response of the axial SiV in Fig. 2.2(b) to approximately estimate $\left(t_{\parallel,\mathrm{es}} - t_{\parallel,\mathrm{gs}}\right)$

by neglecting $(\epsilon_{xx} + \epsilon_{yy})$ in Eq. (2.5). Fig. 2.3(f) plots the mean ZPL frequency of the axial SiV in Fig. 2.2(b) vs. ϵ_{zz} estimated from FEM simulation. The slope of the linear fit yields $\left(t_{\parallel,\mathrm{es}} - t_{\parallel,\mathrm{gs}}\right)$.

$$\left(t_{\parallel,\mathrm{es}} - t_{\parallel,\mathrm{gs}}\right) = -1.7 \pm 0.1\,\mathrm{PHz/strain} \tag{B.5}$$

Likewise, in the case of the transverse SiV in Fig. 2.3(c), we can conclude that $|\epsilon_{xx} - \epsilon_{yy}| \gg \max\{\epsilon_{zx}, \epsilon_{yz}, \epsilon_{xy}\}$. With this class of SiVs, we can approximately estimate $\{d_{\mathrm{gs}}, d_{\mathrm{es}}\}$ by neglecting $\{\epsilon_{zx}, \epsilon_{yz}, \epsilon_{xy}\}$ in Eqs. (2.6,2.7). The significant strain term then is $|\epsilon_{xx} - \epsilon_{yy}|$. Fig. 2.3(e) fits the GS and ES splittings of the transverse SiV in Fig. 2.2(a) vs. $|\epsilon_{xx} - \epsilon_{yy}|$ estimated from FEM simulation. Fitting yields

$$d_{\mathrm{gs}} = 1.3 \pm 0.1, \qquad d_{\mathrm{es}} = 1.8 \pm 0.2 \qquad \mathrm{PHz/strain} \tag{B.6}$$

Once we extract $\left(t_{\parallel,\mathrm{es}} - t_{\parallel,\mathrm{gs}}\right)$ from an axial SiV, we can use this value to further extract $(t_{\perp,\mathrm{es}} - t_{\perp,\mathrm{gs}})$ by fitting Eq. (2.5) to the tuning behavior of the mean ZPL frequency of the transverse SiV. This procedure yields

$$(t_{\perp,\mathrm{es}} - t_{\perp,\mathrm{gs}}) = 0.078 \pm 0.009\,\mathrm{PHz/strain} \tag{B.7}$$

We immediately note that $\left(t_{\parallel,\mathrm{es}} - t_{\parallel,\mathrm{gs}}\right)$ is more than an order of magnitude larger than $(t_{\perp,\mathrm{es}} - t_{\perp,\mathrm{gs}})$. This implies that ϵ_{zz} tunes the mean ZPL frequency much more effectively than $(\epsilon_{xx} + \epsilon_{yy})$. This can be intuitively explained by examining the spatial profile of the GS and ES orbitals (Table 2.7 of Ref.[53]). Since the GS and ES correspond to even (g) and odd (u) eigenstates of SiV's D_{3d} point symmetry group respectively, the charge density distributions of the orbitals e_{gx}, e_{ux} (and e_{gy}, e_{uy}) are similar in any transverse plane normal to the z-axis. As a result, we would expect that the common mode energy shift resulting from the strain-mode $\epsilon_{xx} + \epsilon_{yy}$ is very similar for the GS and ES manifolds, i.e. $t_{\perp,\mathrm{gs}} \approx t_{\perp,\mathrm{es}}$. On the other hand, the energy shift from ϵ_{zz} is expected to have opposite

signs for the GS and ES manifolds due to the change in wavefunction parity along the z-axis.

As the last step, we estimate the values $f_{\rm gs}, f_{\rm es}$. This is done by substituting the fitted values of $d_{\rm gs}$ and $d_{\rm es}$ from Eq. (B.6) in Eqs. (2.6,2.7), which then become single variable expressions in $f_{\rm gs}, f_{\rm es}$ respectively. The resulting expressions can be fit to the response of the axial orientation SiV, which experiences significant ϵ_{yz} (see Fig. 2.3(d)). This gives

$$f_{\rm gs} = -1.7 \pm 0.1, \qquad f_{\rm es} = -3.4 \pm 0.3 \qquad \text{PHz/strain} \tag{B.8}$$

The above error bars for the strain susceptibility parameters are a sum of standard deviations from the fit procedure and from straggle in the SiV implantation depth (10% from SRIM calculations). We note that additional error might arise due to the fact that the device geometry cannot be replicated exactly in FEM simulations for strain estimation.

Appendix C

SiV cantilever sample fabrication and device design

C.1 Fabrication

The diamond NEMS (nano-electro-mechanical system) device used in Chapters 2, 4, 5 was fabricated in three steps in the following order: (i) fabrication of bare diamond cantilevers, (ii) creation of silicon vacancy color centers, and (iii) deposition of electrodes. We use commercially available, $\langle 100 \rangle$-cut, ultra-high purity, single-crystal diamond (type IIa, nitrogen concentration less than 5 ppb) synthesized by chemical vapor deposition (CVD)[159].

Cantilevers are fabricated in two steps. First, diamond with patterned electron-beam resist is etched vertically with oxygen plasma[39]. These vertically-etched structures are then made free-standing by etching the sample at a tilted angle. Specifically, we employ an oxygen-plasma assisted ion-milling process in which the sample is mounted at an angle that is manually adjustable within a few degrees of precision. An illustration of this process, and the resulting suspended structure is schematically shown in Fig. C.1(a).The etching occurs over a period of a few hours, during which the stage is rotated constantly. Further discussion of these techniques can be found in[41,92].

After cantilever fabrication, silicon ions (Si^+) are implanted at target spots on the cantilevers using a custom focused-ion-beam (FIB) system at Sandia National Labs. The spot size of the ion-beam on the sample is 40 nm, and is expected to determine the lateral precision of the implantation procedure. The beam energy is chosen to be 75 keV, which is predicted to yield a mean implantation depth of 50 nm with a straggle of 10 nm according to Stopping and Range of Ions in Matter simulations. Further details of the FIB implantation procedure can be found in[13,56]. After FIB implantation, the sample is subjected to a tri-acid clean (1:1:1 sulfuric, perchloric, and nitric acids), and a three-step high-temperature high-vacuum annealing procedure[74,93] in an alumina tube furnace. The annealing sequence followed comprises steps at 400°C (1.5°C per minute ramp, 8 hour dwell time), 800°C (0.5°C per minute ramp, 12 hour dwell time), and 1100°C (0.5°C per minute ramp, 2 hour dwell time). During the entire procedure, the pressure is maintained below 5×10^{-7} torr. Annealing generates a small amount of graphite on the diamond surface, which is subsequently etched away by a tri-acid clean. Following this step, we perform a cleaning in piranha solution to ensure a high level of oxygen-termination at the diamond surface. With regards to conversion efficiency, we implant approximately 50 Si^+ ions per target spot on the sample, and typically generate 1-3 SiVs at each spot after annealing.

Subsequently, electrode patterns are made by a conventional bi-layer PMMA process followed by metal evaporation. Since the distance between the top surface of the cantilever and the bottom substrate is approximately 4 μm, bi-layer PMMA is spun multiple times until the cantilevers are buried completely. Patterns are written by electron-beam lithography, and metals are evaporated to define the electrodes. Detailed fabrication steps are schematically shown in Fig. C.1(b). Here, the triangle represents the cantilever, and the pedestal to the right of the triangle is the location of the bonding pad for electrical contact. The bi-layer PMMA process is repeated twice - first, to define the bonding pad, and second, to define the electrode pattern near the cantilever. This is because, we use a 200 nm thick gold layer for the bonding pad, but only a 10 nm thick tantalum (Ta) layer

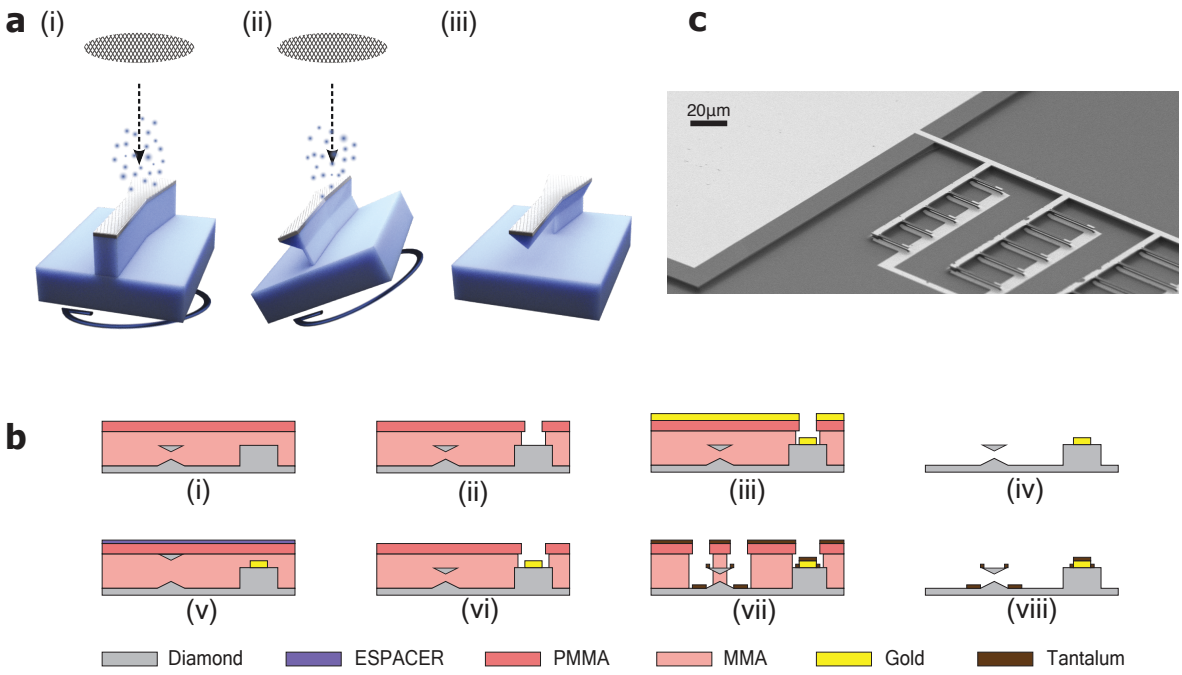

Figure C.1: (a) Schematic of oxygen-plasma assisted ion-milling process for angled-etching of diamond cantilevers. The ion beam is directed at the diamond sample, with a vertically-etched device pattern. The tilted stage is continuously rotated during the etching process. After the cantilevers are freely standing, the etch-mask is stripped. (b) Fabrication process for the placement of electrodes. First, the coarsely aligned bonding pad is defined with a bi-layer PMMA process followed by gold evaporation. Then the same process is repeated to define tantalum electrodes near cantilevers, but with better alignment precision. Conductive layer (ESPACER 300Z) on top of the cantilever is helpful for precise alignment. (c) SEM image of the complete chip showing connection between the bonding pad and electrodes on top of the cantilevers.

for the cantilever electrodes. Fig. C.1(c) shows the scheme to connect electrodes on top of the cantilevers to the bonding pad on the diamond pedestal. Electrodes on the substrate below the cantilevers are connected to a second bonding pad (not shown in the figure) that is directly on the surface of the diamond.

We now discuss the choice of 10 nm tantalum film for our cantilever electrodes. For five different metals we have tested as a cantilever electrode material (aluminium, chromium, copper, titanium and tantalum), our device always shows a continuous, non-zero leakage-current upon applying voltage. While the exact reasons for this leakage-current on our sample, in particular, are unknown, there have been numerous studies on the surface conductivity of diamond under various conditions[160]. For aluminium, chromium, copper and titanium, this leakage current destroys the electrode when a high voltage (in the few hun-

dred volts range) is applied. The destruction of electrodes appeared to be the result of melting or bursting of the thin metal film, likely caused by Joule heating[161]. Tantalum is one of the metals with the highest melting and evaporation points among those available for e-beam evaporation. We find that devices with tantalum electrodes are robust enough to operate at very high applied voltage (∼600 V across an electrode gap of approximately 4 μm, which corresponds to an electric-field of 1.5 MV/cm). The thickness of tantalum is kept below 10 nm in order to avoid thin film-induced stress in the cantilever, which leads to pre-strained SiV centers.

C.2 Device design

An important figure of merit for our NEMS device is the maximum achievable strain at the location of SiV. In this section, we discuss two key design aspects that need to be considered towards this goal: (i) 'pull-in instability', and (ii) practical limits for high voltage operation.

Pull-in instability is a well-known phenomenon for an electrostatic actuator made with a parallel plate capacitor as shown in Fig. C.2(a). In these devices, voltage is applied to induce an electrostatic force between two plates, where either one or both of them are free to move. Upon applying a voltage, the capacitor deforms until it reaches equilibrium, when there is a balance between the electrostatic force, and the restoring force exerted by the elasticity of the material. The net force acting on the free top plate in Fig. C.2(a) can be modeled as

$$F(x,V) = -\frac{\partial U(x,V)}{\partial x} = \frac{1}{2}\varepsilon A\frac{V^2}{(d-x)^2} - kx \tag{C.1}$$

where x is the displacement of the plate, $U(x,V)$ is the potential energy and ε is the permittivity of the material between the two plates. A is the area of the capacitor, V is the voltage applied, d is the distance between the two plates at 0 V, and k is the spring

constant, respectively. By integrating equation (C.1), we can calculate $U(x, V)$ at various voltages as shown in Fig. C.2(b). The local minimum in the potential represents a condition of stable equilibrium. As the voltage is increased, the local minimum shifts towards the bottom plate, indicating that the top plate gets displaced downwards, thereby reducing the capacitor gap. When the voltage changes from $3V_0$ to $4V_0$ in the Fig. C.2(b), the stable local minimum disappears. This occurs, when the top plate is displaced by about one-third of the initial gap between the two plates, i.e. when $x = d/3$. At this point, the system reaches a condition in which the top plate snaps down to the bottom plate. Our device is a slight variation of this conceptual model, and hence, the maximum deflection of our cantilever will be limited by pull-in instability (but not at exactly $x = d/3$).

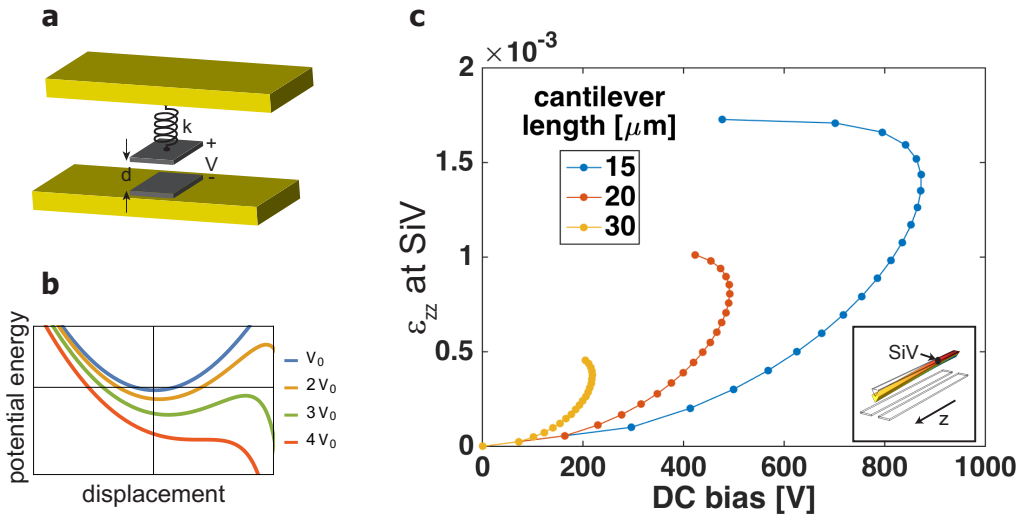

Figure C.2: (a) Illustration of a parallel plate capacitor with one freely movable plate (top), and one fixed plate (bottom). The top electrode can be actuated by applying a voltage. (b) Potential energy of the system in (a) with the different voltages. The stable minimum in the potential disappears, when the system reaches the condition of pull-in instability at a voltage of $4V_o$. (c) FEM simulation of the strain-component along the long-axis of the cantilever (most dominant strain-tensor component) near the clamp of the cantilever (inset). Turnaround points in the graph represent pull-in instabilities.

A 3D finite element method (FEM) calculation can be used to simulate pull-in instability accurately for complex structures[162]. Typically, a simulation can be run by setting a particular voltage on the electrode, and solving for the resultant deformation of the structure, thereby arriving at the strain profile inside the cantilever. One can also run the in-

verse of this procedure. By setting a target displacement of the cantilever tip, the voltage required to achieve this displacement can be calculated. Such an inverse calculation can help arrive at the condition for pull-in instability. Fig. C.2(c) shows the results of a simulation run so as to solve this inverse problem. Strain at the SiV location is plotted as a function of the voltage for different cantilever lengths. Turnaround points represent the pull-in instability condition at which both the displacement of the cantilever-tip and the applied voltage reach the maximum value possible before the cantilever snaps down. Fig. C.2(c) provides two important conclusions: First, for a given voltage, longer cantilevers provide larger strain for a given voltage, because they have a smaller spring constant. Second, the maximum attainable strain is higher for shorter cantilevers, because they reach the pull-in instability condition at a higher voltage. Therefore, shorter devices are preferred to generate high strain, when arbitrarily high voltage can be applied.

In practice, however, there are mechanisms that limit the maximum possible voltage e.g. Townsend breakdown, field emission and surface current[163,164,165], all of which can be significant depending on experimental conditions. With the fabrication method described in Section C.1, our devices could be operated safely up to voltage as high as 600 V under high vacuum ($\sim 10^{-7}$ torr) at cryogenic temperature (4 K). Given that the minimum electrode gap is 4 μm, this condition corresponds to an electric field of approximately 1.5 MV/cm. Experiments described in Section D.4 are carried out in a helium closed-cycle cryostat with the sample surrounded by helium exchange gas at a pressure of 1 mbar. Under these conditions, we observed safe operation up to 500 V. The maximum voltage in this setup is thought to be limited by dielectric breakdown of helium gas.

Considering all the design limitations discussed above, we chose cantilevers of width 1.2-1.3 μm and length 25-30 μm for the experiments in this work.

Appendix D

Silicon vacancy strain tuning: experimental methods

D.1 Strain-dependent photoluminescence measurements

The sample is cooled down to a nominal temperature of 6 K inside a Janis ST-500 continuous helium-flow cryostat. The cryostat is mounted under a home-built scanning confocal microscope with a 0.9 NA 100×, 1 mm working distance objective (Olympus MPLFLN 100X) housed inside the cryostat. SiV centers are identified via non-resonant excitation with a 703 nm laser diode (Thorlabs LP705-SF15), and collection of zero-phonon-line (ZPL) fluorescence in a narrow bandwidth of 10 nm around 737 nm. For resonant photoluminescence excitation (PLE) of ZPL transitions, we use a tunable continuous-wave Ti-sapphire laser (M-Squared Solstis), and collect the resulting fluorescence in the phonon-sideband (above 750 nm). Mode-hop-free tuning of the laser is achieved over the scan range of interest by using feedback from a wavemeter (High Finesse WS7). A CW 532 nm laser is periodically pulsed using an acousto-optic modulator (Crystal Technology 3080) to maintain the negative charge state of SiV(-) centers[56]. Collected fluorescence (gated off during

green excitation) is sent to an avalanche-photodiode to measure the photon-count rate. DC voltage for cantilever-deflection is supplied from a Stanford Research Systems PS300 high-voltage source. As an added precautionary measure, the weak leakage-current in the circuit (typically below 100 nA) discussed in Section C.2 is monitored via a Keithley 2400 source-meter. Strain-response measurements involve taking resonant excitation spectra as the voltage applied to the device is steadily increased. Strain corresponding to the applied voltage is estimated through finite element method (FEM) simulations as described in Appendix C.

D.2 High strain SiV centers

With our device we can tune the splitting of the orbitals in the GS manifold from 46 GHz to typically up to 500 GHz. In the best case, we reach 1.2 THz by generating uniaxial strain of $\sim 10^{-3}$ in a cantilever at a voltage of 600 V. Example spectra showing extreme strain-tuning into the THz regime are shown in Figure D.1. At high strain, as $\Delta_{\text{gs}} \gg k_B T \sim$80 GHz at T=4 K, population in the upper branch of the ground-state manifold decreases exponentially, while the population in the lower branch correspondingly increases to near-unity. As a result, with increasing strain, the B and D transitions become weaker in intensity, and eventually vanish. Simultaneously, the linewidth of the A transition increases owing to increasingly rapid phono emission in the excited state from the upper branch to the lower branch. On the other hand, as the C transition connects the lower branches in ground and excited states, its linewidth is not affected as strongly by phonon-mediated processes, and is measured to be relatively unchanged with strain (See Appendix G). The C transition also becomes brighter at high-strain due to near-unity population in the lower ground state branch.

While the high-strain spectra only reveal A and C transitions, the difference in their frequencies gives us the excited-state splitting Δ_{es} exactly. Since the same strain-components

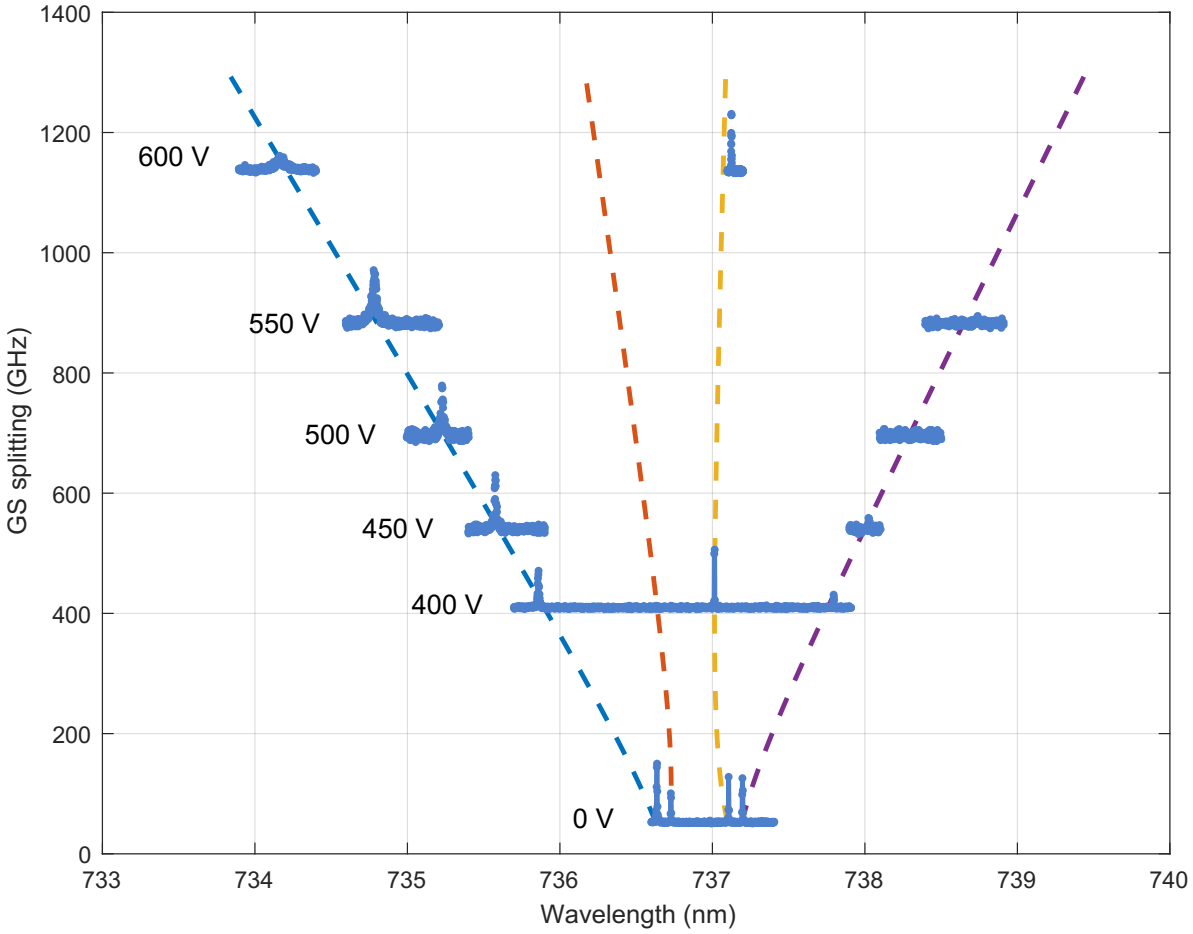

Figure D.1: Tuning of PLE spectrum of a transverse SiV subject to high strain. Voltage applied to the device is indicated next to each spectrum. y-axis shows ground-state splitting Δ_{gs} corresponding to the spectrum estimated using the procedure detailed in the text. Dashed lines correspond to modeled strain-response of the four optical transitions.

are responsible for increasing $\Delta_{\rm gs}$ and $\Delta_{\rm es}$, we can use the strain-susceptibilities in Chapter 2 to estimate $\Delta_{\rm gs}$. Using this procedure, for the highest strain condition in Figure D.1, we infer $\Delta_{\rm gs} = 1.2\,\mathrm{THz}$.

D.3 Orbital thermalization measurements

We use time resolved pump-probe fluorescence to characterize the phonon processes in the GS. In this method, two consecutive laser pulses resonant with the D transition are used to, first initialise GS orbital population in the lower branch, and after a set delay τ, read-out population in the upper branch. A schematic of the pulse sequence, and an example of a resulting fluorescence time-trace are shown in Fig. D.2. By repeating this sequence for steadily increasing pump-probe delay τ, we measure the rate at which the GS population relaxes towards thermal equilibrium due to resonant phonons.

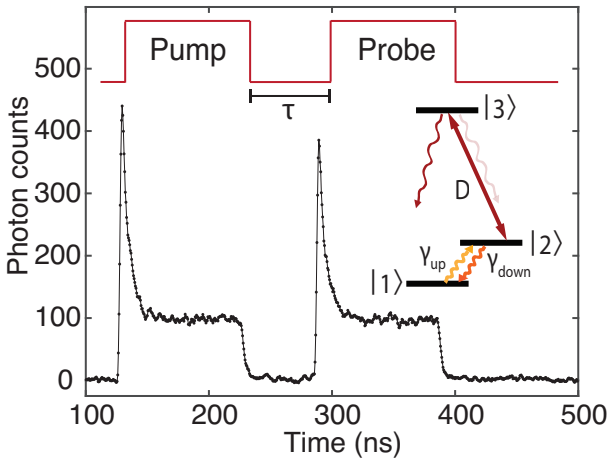

Figure D.2: Time-resolved fluorescence signal in pump-probe measurement for a delay $\tau = 50$ ns between the two laser pulses. The laser is resonant with the D transition, and optically pumps the GS population into the lower spin-orbit branch over a timescale of few ns. After time τ, the fluorescence signal from the probe pulse has a leading edge determined by the population in the upper GS branch. The decay rates between the GS branches - $\gamma_{\rm up}$ due to phonon-absorption, and $\gamma_{\rm down}$ due to phonon-emission - are also shown.

D.3.1 Experimental setup

The pump-probe pulse sequence described above is implemented by pulsing our resonant-excitation laser with a Mach-Zehnder intensity electro-optic modulator (EO Space AZ-AV5-5-PFA-PFA-737) driven by a digital-delay generator with rise- and fall-times of 2 ns (SRS DG645). Over the course of the measurements, the operation point of the intensity electro-optic modulator (EOM) is stabilized against long-term drifts with continuous feedback on the DC-bias voltage. The feedback loop is implemented with a lock-in amplifier (SRS SR830) generating a low-frequency (1 KHz) modulation of the DC-bias voltage. Photon-count pulses from the single-photon-detector are time-tagged on a PicoHarp 300 module triggered by the delay-generator. The laser frequency itself is stabilized by continuous feedback with a wavemeter (High Finesse WS7).

D.3.2 Extraction of thermalization rate

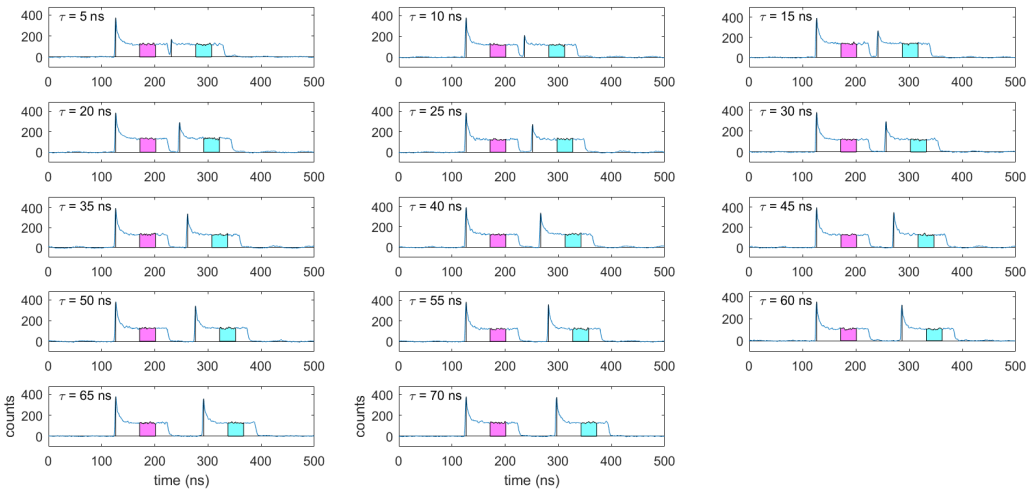

Figure D.3: Fluorescence time-traces for various pump-probe delays between τ=5 ns to 70 ns taken at GS-splitting Δ_{gs}=46 GHz. x-axis is time in ns, and y-axis is photon counts integrated over multiple iterations of the pulse sequence.

Example data from implementing the pulse sequence in Fig. D.2 for various pump-probe delays is shown in Fig. D.3. This data can be interpreted and processed to yield a GS-

population thermalization curve as follows. As shown in Fig. D.4a, the leading edge of the first fluorescence signal corresponds to thermal population $p_{2,th}$ in the upper branch of the GS. Upon switching on the pump pulse, this decays to a residual value $p_{2,opt}$ determined by the competition between the optical pumping rate (above saturation, this is simply the decay rate γ_e from the excited state) and the rates $\gamma_{\text{up}}, \gamma_{\text{down}}$. After time delay τ, the leading edge of the probe fluorescence signal corresponds to partially recovered population $p_2(\tau)$ due to thermalization. We can describe the population recovery in the upper GS branch as

$$(p_2(\tau) - p_{2,th}) = (p_2(\tau) - p_{2,opt}) \exp\left[-\left(\gamma_{\text{up}} + \gamma_{\text{down}}\right) t\right] \tag{D.1}$$

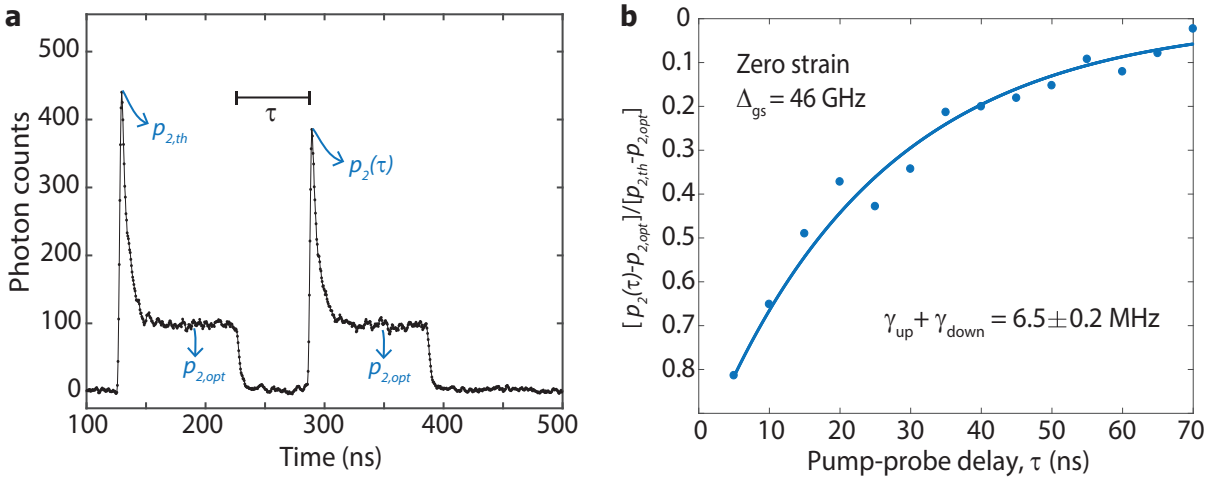

Figure D.4: (a) Fluorescence time-trace for τ=50 ns from Fig. D.3 showing relevant quantities related to the population in the upper GS branch. (b) Thermalization curve constructed by extracting the normalized change in photon-counts for various pump-probe delays τ. Solid line is an exponential fit.

In particular, we calculate the normalized change in photon-counts, $(p_2(\tau) - p_{2,th}) \,/\, (p_2(\tau) - p_{2,opt})$ from each measurement in Fig. D.3, and carry out an exponential fit in Fig. D.4b to extract $(\gamma_{\text{up}} + \gamma_{\text{down}})$. Repeating this experiment for various values of GS-splitting Δ_{gs}, we arrive at Fig. 4.2c.

From the optical-pumping fluorescence signal, we can define a pumping efficiency $\left(1 - \frac{p_{2,opt}}{p_{2,th}}\right)$. This describes the ability of the pump pulse to initialize GS population in the lower GS

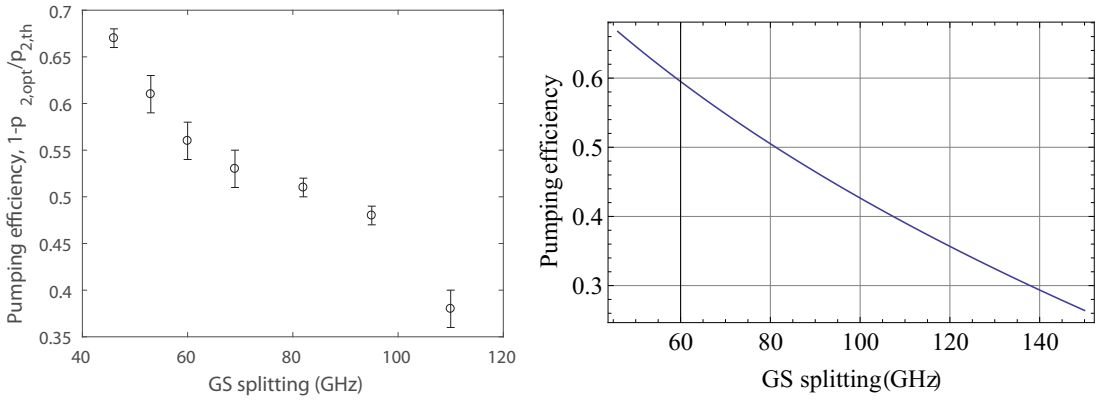

Figure D.5: (a) Experimentally measured optical-pumping efficiency (see text for definition) versus GS-splitting $\Delta_{\rm gs}$. (b) Theoretically estimated optical-pumping efficiency using a three-level rate equations model. We assume optical pumping above saturation, GS thermalization rates, $\gamma_{\rm up}$ and $\gamma_{\rm down}$ to follow the model in Appendix E, excited state decay rate γ_e = 90 MHz, branching ratio into the lower GS branch = 0.5.

branch by acting against the thermalization process. As the GS-splitting $\Delta_{\rm gs}$ is increased, we find that the pumping-efficiency decreases in Fig. D.5. This can be attributed to the downward thermalization rate $\gamma_{\rm down}$ rapidly increasing with $\Delta_{\rm gs}$ as discussed in Appendix E. At large $\Delta_{\rm gs}$, the optical pumping rate, R_{opt}, which is $\sim \gamma_e$, the excited state decay rate cannot substantially outweigh $\gamma_{\rm down}$. As a result, the GS population cannot be optically polarized better than the level dictated by thermal equilibrium. This makes it impractical to measure the thermalization rate beyond a certain $\Delta_{\rm gs}$ using the pump-probe technique. In our experiments, we measure up to $\Delta_{\rm gs}$ = 110 GHz.

D.4 SiV spin measurement techniques

D.4.1 Experimental setup

The sample is cooled down to a temperature of 3.8 K inside a closed cycle liquid helium cryostat (Attodry 1000). It is placed in a dip stick, in which helium gas (pressure $\sim$ 1 mbar) acts as an exchange gas. Two superconducting coils surrounding the sample chamber can be used to apply a magnetic field along two orthogonal axes, up to 8 T vertically and up to 2 T horizontally. DC voltage for cantilever-deflection is supplied by a high-voltage source

(Stanford Research Systems PS310/1250V-25W). As an added precautionary measure described in Section D.1, the weak leakage-current in the circuit (typically below 100 nA) is monitored via a Keithley 2400 source-meter. The optical part of the setup consists of a home-built confocal microscope mounted on top of the cryostat, and a microscope objective (NA = 0.82) inside the sample chamber. The sample is mounted on piezoelectric stages (Attocube ANPx101 and ANPz101) allowing to position the sample with respect to the objective. Non-resonant excitation of SiVs is performed using a diode laser at 660 nm (Laser Quantum Ventus), while resonant excitation is achieved with a tunable diode laser around 737 nm (Toptica DLpro). The frequency of the latter is stabilised through continuous feedback from a wavemeter (High Finesse WSU).

D.4.2 Coherent-population-trapping

For coherent population trapping (CPT), sidebands are generated on the resonant excitation laser using an EOM (Photline NIR-MX800) connected to a tunable microwave source (Rhode&Schwarz SMF 100A). Fluorescence from the emitters is collected through the microscope objective. A 750 nm long-pass filter in the confocal microscope allows collection of the phonon-sideband emission from SiV^- centres, filtering out the laser excitation. This emission is then sent to an avalanche photodiode (APD) (Excellitas). This measurement is repeated for different values of ground state splitting, the results of which constitute Fig. 4.3 of the main text.

D.4.3 Calibration of ground and excited state splittings with applied voltage at high strain

The ground state splitting can be measured directly by considering the energy difference between the C and D transitions. Due to the presence of other SiV^- centres generated at the same spot due to the FIB implantation procedure, measuring this energy difference be-

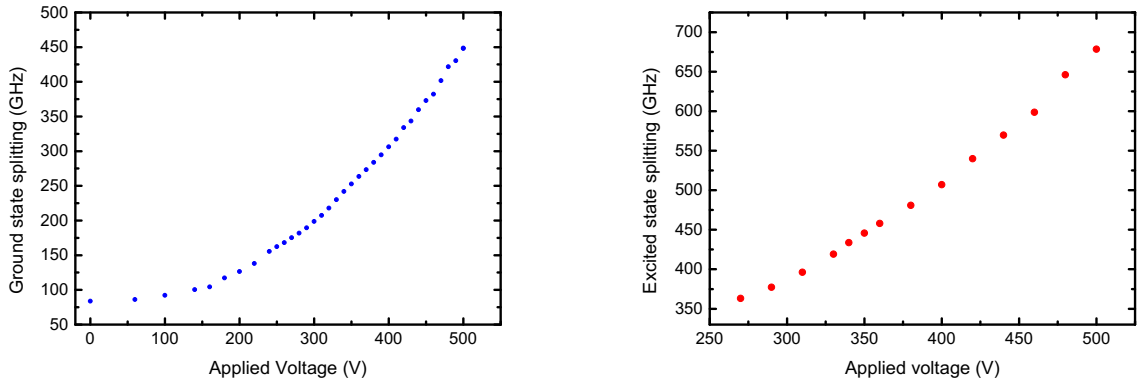

Figure D.6: SiV ground state splitting (left), and excited state splitting (right) measured as a function of voltage applied to the cantilever. Error bars are smaller than the dots and correspond to the standard deviation on the frequency difference between C and D transitions estimated from Lorentzian fits.

tween C and D transitions through non-resonant PL spectra is impractical. At the same time, simultaneous detection of C and D transitions through resonant excitation is not possible at high strain, since the thermal population in upper GS branch becomes negligible as discussed in Section D.1. To overcome this limitation, we resonantly excite transition A of the SiV center being studied, and record the spectrum of transitions C and D on a spectrometer after having filtered out the resonant laser with a monochromator. The spectra are then fitted with two Lorentzian functions to extract the value of the ground state splitting, as shown in Figure D.6. Likewise, the excited state splitting (also shown in the figure) can be derived as the difference between the frequencies of transitions A and C in this measurement.

Appendix E

SiV thermal relaxation models

E.1 Orbital relaxation

E.1.1 Theory

Due to the nature of the strain interaction, phonons that are resonant with the ground state splitting Δ_{gs} can directly drive the orbital transition. The transition rates driven by the continuum of lattice phonon modes can be calculated using Fermi's golden rule[59] to get:

$$\gamma_{\text{up}}(\Delta_{\text{gs}}) = 2\pi\chi\rho\Delta_{\text{gs}}^3 n_{th}(\Delta_{\text{gs}}) \tag{E.1}$$

$$\gamma_{\text{down}}(\Delta_{\text{gs}}) = 2\pi\chi\rho\Delta_{\text{gs}}^3 (n_{th}(\Delta_{\text{gs}}) + 1) \tag{E.2}$$

where ρ is a constant proportional to average speed of sound in bulk, n_{th} is the number of thermal phonons per mode and χ is the interaction frequency for a single phonon. In these expressions, the first term in the product, $2\pi\chi\rho\Delta_{\text{gs}}^3$ corresponds to the mean-squared single-phonon coupling rate multiplied with the DOS at the GS splitting Δ_{gs}, while the second term corresponds to the thermal occupation of each mode. Fig. E.1 shows plots of

the calculated dependence of upward and downward rates on $\Delta_{\rm gs}$ at temperature $T = 4\,\mathrm{K}$. We observe that the upward rate shows a non-monotonic behavior, approaching its maximum value around $h\Delta_{\rm gs} \sim k_B T$. The increasing DOS term dominates in the regime $h\Delta_{\rm gs} < k_B T$, and causes $\gamma_{\rm up}$ to increase. However, when $h\Delta_{\rm gs} \gg k_B T$, the thermal occupation of the modes behaves as $n_{th}(\Delta_{\rm gs}) = \exp\left(-\frac{h\Delta_{\rm gs}}{k_B T}\right)$. This exponential roll-off dominates the polynomially increasing DOS, and causes $\gamma_{\rm up}$ to decrease at higher strain. In contrast, the downward rate monotonically increases with the GS-splitting, because it is dominated by the spontaneous emission rate, which simply scales as the DOS.

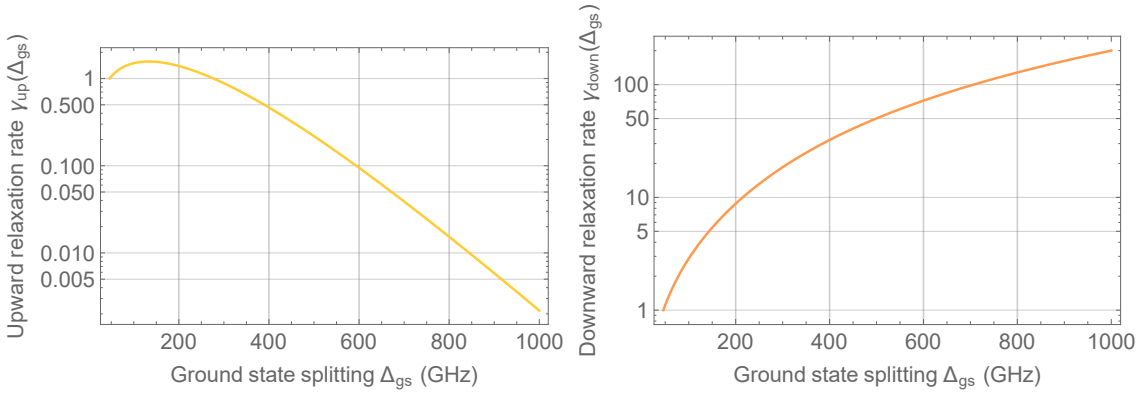

Figure E.1: Variation of the upward (phonon-absorption) and downward (phonon-emission) relaxation rates with GS-splitting $\Delta_{\rm gs}$ at temperature T=4 K. The y-axis is normalized to the zero-strain rates $\gamma_{\rm up}(46\mathrm{GHz})$ and $\gamma_{\rm down}(46\mathrm{GHz})$ in each plot respectively.

E.1.2 Fitting

With the pump-probe technique used in our experiments, we measure the sum of the upward and downward rates, which should have the dependence

$$\gamma_{\rm up}(\Delta_{\rm gs}) + \gamma_{\rm down}(\Delta_{\rm gs}) = A\Delta_{\rm gs}^3(2n_{th}(\Delta_{\rm gs}) + 1) = A\Delta_{\rm gs}^3 \coth\left(\frac{h\Delta_{\rm gs}}{k_B T}\right) \tag{E.3}$$

where A is a constant. Our cantilever has lateral dimensions of order $1\,\mu$m. This is about an order of magnitude larger than half the acoustic wavelength for $\Delta_{\rm gs} = 50\,\mathrm{GHz}$ in diamond, which is $\sim$120 nm. Thus, the cantilever itself is a bulk-like structure for the SiV.

However, as can be observed in the left panel of Fig. E.2 our experimental data shows very poor agreement with the theoretically predicted behavior in equation (E.3).

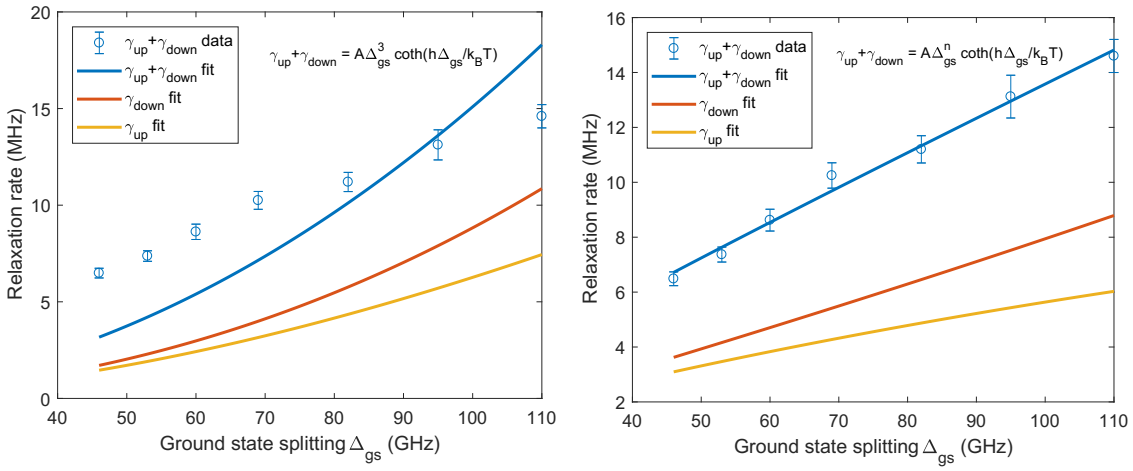

Figure E.2: Fits to experimental measurements of net orbital thermalization rate $\gamma_{\mathrm{up}} + \gamma_{\mathrm{down}}$ (solid blue line) assuming coupling to only bulk acoustic modes (left plot), and unknown DOS behavior (right plot) with varying n. Fit expressions are indicated in top left corner of each plot. Corresponding individual rates γ_{up} and γ_{down} are extracted and plotted after fitting in each case (solid yellow and orange lines). The fit to variable DOS (right plot) yields $n = 1.9 \pm 0.3$.

Instead, when we allow the exponent of the DOS term to be a variable n, we obtain a better fit yielding $n = 1.9 \pm 0.3$. We can arrive at a possible explanation for this discrepancy, if we note that the SiV is situated at a nominal depth of 50 nm, which is sub-wavelength for phonons in the frequency range of Δ_{gs} probed in our experiment. As a result, we can expect appreciable coupling to surface acoustic modes, which are not accounted for in the above derivation. Since the DOS of surface modes scales as Δ_{gs}^2, it appears that the thermalization rate in our experiment is almost entirely determined by surface modes.

E.2 Spin relaxation

E_g-phonons predominantly drive spin-conserving transitions between the GS orbitals of the SiV i.e. between $\{|e_{g-}\downarrow\rangle', |e_{g+}\downarrow\rangle'\}$, and $\{|e_{g+}\uparrow\rangle', |e_{g-}\uparrow\rangle'\}$ respectively. However, in the presence of an off-axis magnetic-field, and non-zero static strain, the eigenstates of the

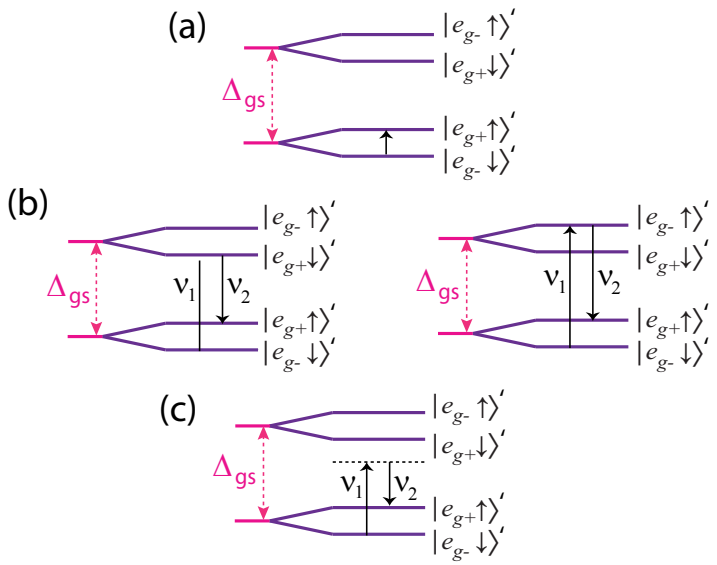

Figure E.3: Various pathways for a phonon-mediated spin-flip (a) Direct relaxation via a single phonon resonant with the $|e_{g-}\downarrow\rangle' \rightarrow |e_{g+}\uparrow\rangle'$ spin-transition. (b) Two possible channels for a resonant two-phonon process involving the upper orbital branch. (c) Off-resonant two-phonon processes.

GS manifold are no longer pure SO or strain eigenstates, and all transitions between the four states within the GS manifold become allowed for E_g-phonons. In this scenario, the various channels for spin-relaxation from $|e_{g-}\downarrow\rangle'$ to $|e_{g+}\uparrow\rangle'$ are:

- Direct single-phonon relaxation: Via a single phonon of frequency ω_s resonant with the spin-transition as shown in Fig. E.3(a)
- Resonant two-phonon relaxation: Via two phonons resonant with a level in the upper orbital branch as an intermediate state as shown in Fig. E.3(b). The spin-flip can be caused by either the emitted phonon (left) or the absorbed phonon (right).
- Off-resonant two-phonon relaxation: Via two phonons with a virtual level as an intermediate state as shown in Fig. E.3(c). The effective driving strength will be reduced from its value in the resonant process by an amount corresponding to the detuning from the upper orbital branch.

Using Fermi's golden rule, the transition rates for these relaxation channels can be calculated. The results are summarized in Table E.1, and are plotted versus GS splitting Δ_{gs}

Table E.1: Summary of spin-relaxation mechanisms. θ is the angle between the applied magnetic field and the z-axis of the SiV. $B_\perp$ is the magnitude of magnetic field in the transverse plane of the SiV.

Mechanism	Rate	Relevant regime	Expected scaling of rate
Single-phonon	$2\pi \left(\frac{d_{\text{spin}}}{d_{\text{gs}}}\right)^2 \chi\rho\omega_s^3 n_{th}(\omega_s)$	$k_BT/h \ll \omega_s$	$B_\perp^2 \Delta_{\text{gs}}^{-2}\omega_s^3 \exp(-h\omega_s/k_BT)$
Resonant two-phonon	$4\left(\frac{d_{\text{gs,flip}}}{d_{\text{gs}}}\right)^2 \gamma_{\text{up}}$	$k_BT/h \sim \Delta_{\text{gs}}$	$\sin^2\theta\Delta_{\text{gs}}[\exp(h\Delta_{\text{gs}}/k_BT)-1]^{-1}$
Off-resonant two-phonon	$\frac{8\pi^7}{945}\left(\frac{d_{\text{gs,flip}}}{d_{\text{gs}}}\right)^2 \chi^2\rho^2\omega_s^2\Delta_{\text{gs}}^{-4}\left(\frac{k_BT}{h}\right)^7$	$k_BT/h \gg \Delta_{\text{gs}}$	$\sin^2\theta\Delta_{\text{gs}}^{-2}\omega_s^2 T^7$

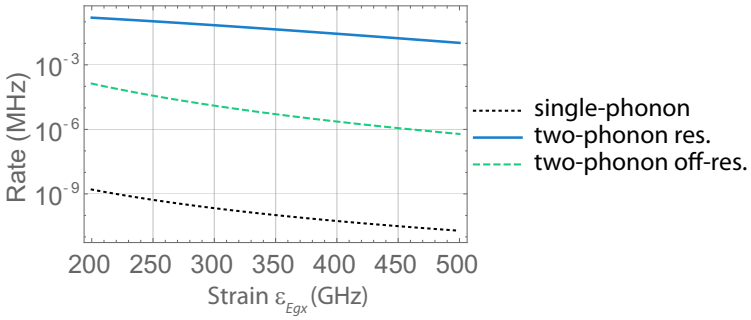

Figure E.4: Rates of all three spin-relaxation mechanisms indicating their magnitudes and scaling with strain β.

in Fig. E.4.

We see that spin relaxation at 4 K is dominated by a two-phonon process involving the upper ground state orbital branches as intermediate states. In literature, this is frequently referred to as an Orbach process.[114] The experimentally observed behavior of spin T_1 in Fig. 4.4b of the main text is well-explained by the scaling of such a process with the GS splitting Δ_{gs} shown in Table E.1. Intuitively, we may understand the dominance of the Orbach process in terms of the phonon DOS $\propto \Delta^n \exp(-h\Delta/k_BT)$ being maximized around the frequency $\Delta \sim k_BT/h$. We can similarly argue that the single and off-resonant two-phonon channels become relevant in other temperature regimes indicated in Table E.1, where the phonon DOS is maximized in a frequency range relevant for those processes.

Appendix F

Investigation of double-dip CPT signal

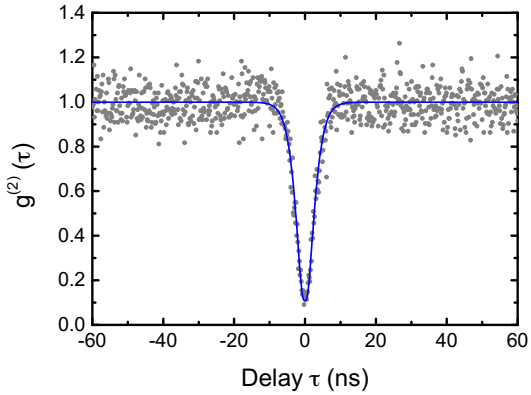

Figure F.1: Second-order correlation measurement of the SiV^- centre investigated. The measured data points are plotted as grey dots. A fit based on a three-level model and accounting for timing jitter is plotted as a blue curve.

We discuss the origin of two dips in the CPT measurements presented in Chapter 4. We first rule out the hypothesis that the two dips in our CPT measurements originate from two different SiV centres. The dips are very similar in width and depth, and their frequency-separation remains constant (4.0 ± 0.1 MHz) over a wide range of applied strain (see Fig. 4.3b of main text). In the event that this is caused by two SiV centers, they are required to have the same fluorescence intensity, and experience exactly the same strain

conditions at any applied voltage, which is very unlikely. In order to categorically establish that we are investigating a single SiV centre, we perform a Hanbury-Brown-Twiss (HBT) experiment on the phonon-sideband fluorescence upon resonant excitation of transition C, and measure the second order correlation function $g^{(2)}$ as shown in Fig. F.1. The $g^{(2)}$ function is fitted using a three-level model convolved with the Gaussian response of the avalanche photodiodes used, which have a timing jitter of 350 ps. At zero time delay, a clear anti-bunching reaching $g^{(2)}(\tau = 0) = 0.12$ indicates that the measured photons originate from a single emitter.

To gain more insight into the origin of the two CPT dips, we perform CPT at varying orientation of the applied magnetic field, while keeping its magnitude (0.2 T) constant. We work in the high-strain regime at a ground state splitting of 467 GHz. In our results, shown in Fig. F.2, we observe that the separation between the two CPT dips displays a periodic variation as the magnetic field is rotated.

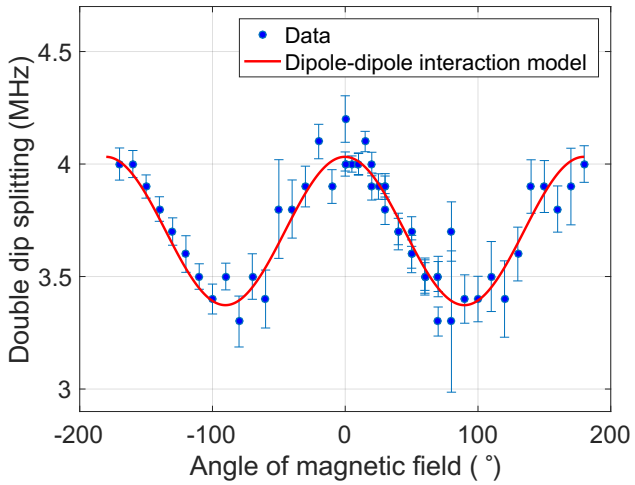

Figure F.2: Dependence of CPT dip separation on magnetic field orientation. The angle plotted on the x-axis is measured with respect to the vertical direction on the sample. 0° corresponds to the $[001]$ axis of diamond, while 90° corresponds to the $[110]$ axis of diamond, along which the cantilever long-axis is aligned. The SiV investigated is a transverse SiV, so its internal Z-axis is either $[1\bar{1}1]$ or $[\bar{1}11]$. Error bars correspond to the standard deviation on the CPT dip frequencies estimated from Lorentzian fits.

Given the similarity of the two dips, a very plausible explanation for the double-dip

structure is the presence of a proximal spin in the environment of the SiV centre being studied. Physically, varying the direction of the applied B-field leads to a variation in the quantization axis of the SiV electron-spin (or semi-classically, the orientation of the electron magnetic moment). Likewise, the quantization axis of the proximal spin has its own variation with the B-field orientation. For instance, if this proximal spin is a nuclear spin, to first order, its orientation simply follows that of the applied B-field. As a result, the dipole-dipole interaction energy of the SiV electron-spin with the neighboring spin varies with B-field orientation, leading to the periodic behavior observed experimentally in Fig. F.2. Below, we describe a semi-classical approach to model the CPT dip separation as a dipole-dipole interaction.

The Hamiltonian for two dipoles with magnetic moments $\boldsymbol{\mu_1}$ and $\boldsymbol{\mu_2}$ is given by

$$\mathbb{H}^{\text{d-d}} = -\frac{\mu_0}{4\pi \left|\mathbf{r}\right|^3} \left(3 \left(\boldsymbol{\mu_1} \cdot \hat{\mathbf{r}}\right) \left(\boldsymbol{\mu_2} \cdot \hat{\mathbf{r}}\right) - \boldsymbol{\mu_1} \cdot \boldsymbol{\mu_2}\right) \tag{F.1}$$

where μ_0 is the vacuum-permeability, $\mathbf{r}$ is the vector from one dipole to the other, and $\hat{\mathbf{r}}$ is given by $\mathbf{r}/\left|\mathbf{r}\right|$. If the two dipoles are spins described by spin angular momentum $\mathbf{S}_1$ and $\mathbf{S}_2$, we can write the interaction Hamiltonian in terms of the spin-operators.

$$\mathbb{H}^{\text{d-d}} = -\frac{\mu_0 \epsilon_{E_{gy}1} \epsilon_{E_{gy}2}}{4\pi \left|\mathbf{r}\right|^3} \left(3 \left(\mathbf{S}_1 \cdot \hat{\mathbf{r}}\right) \left(\mathbf{S}_2 \cdot \hat{\mathbf{r}}\right) - \mathbf{S_1} \cdot \mathbf{S_2}\right) \tag{F.2}$$

where $\epsilon_{E_{gy}i}$ is the gyromagnetic ratio of spin i. Semi-classically, we can treat spin angular momentum as a vector quantity $\mathbf{S} = \frac{\hbar}{2}\left(\langle\sigma_x\rangle, \langle\sigma_y\rangle, \langle\sigma_z\rangle\right)$, where $\sigma_x, \sigma_y, \sigma_z$ are Pauli spin-matrices. This vector describes the mean-orientation of the electron magnetic moment. To calculate the SiV electron-spin orientation under our experimental conditions, the full ground-state Hamiltonian including spin-orbit coupling, external strain, and magnetic field must be diagonalized. The effect of the external magnetic field is described by the Zeeman Hamiltonian below written in the basis $\{|e_X,\uparrow\rangle, |e_X,\downarrow\rangle, |e_Y,\uparrow\rangle, |e_Y,\downarrow\rangle\}$[53],

$$\mathbb{H}^{\text{Zeeman}} = q\epsilon_{E_{gy}L}\hat{L}_z B_z + \epsilon_{E_{gy}S}\hat{\mathbf{S}}\cdot\mathbf{B} = q\epsilon_{E_{gy}L}\begin{bmatrix} 0 & 0 & iB_z & 0 \\ 0 & 0 & 0 & iB_z \\ -iB_z & 0 & 0 & 0 \\ 0 & -iB_z & 0 & 0 \end{bmatrix} + \epsilon_{E_{gy}S}\begin{bmatrix} B_z & B_x - iB_y & 0 & 0 \\ B_x + iB_y & -B_z & 0 & 0 \\ 0 & 0 & B_z & B_x - iB_y \\ 0 & 0 & B_x + iB_y & -B_z \end{bmatrix} \quad \text{(F.3)}$$

where the first and second terms are from the orbital angular momentum, and the spin angular momentum, respectively. $\hat{L}_z$ and $\hat{S}$ are L_z and $\mathbf{S}$ normalized by $\hbar$, respectively. The gyromagnetic ratios for each term are given by $\epsilon_{E_{gy}L} = \mu_B/\hbar$, $\epsilon_{E_{gy}S} = 2\mu_B/\hbar$, where μ_B is the Bohr magneton. q is a quenching factor that is commonly observed in solid-state emitters[53].

The total Hamiltonian $\mathbb{H}^{\text{total}}$ is obtained by adding the spin-orbit Hamiltonian $\mathbb{H}^{\text{SO}}$ and strain Hamiltonian $\mathbb{H}^{\text{strain}}$.

$$\mathbb{H}^{\text{total}} = \mathbb{H}^{\text{SO}} + \mathbb{H}^{\text{strain}} + \mathbb{H}^{\text{Zeeman}} \quad \text{(F.4)}$$

$$\mathbb{H}^{\text{SO}} + \mathbb{H}^{\text{strain}} = \begin{bmatrix} \epsilon_{A_{1g}} - \epsilon_{E_{gx}} & 0 & \epsilon_{E_{gy}} - i\lambda_{SO}/2 & 0 \\ 0 & \epsilon_{A_{1g}} - \epsilon_{E_{gx}} & 0 & \epsilon_{E_{gy}} + i\lambda_{SO}/2 \\ \epsilon_{E_{gy}} + i\lambda_{SO}/2 & 0 & \epsilon_{A_{1g}} + \epsilon_{E_{gx}} & 0 \\ 0 & \epsilon_{E_{gy}} - i\lambda_{SO}/2 & 0 & \epsilon_{A_{1g}} + \epsilon_{E_{gx}} \end{bmatrix} \quad \text{(F.5)}$$

λ_{SO} is the spin-orbit coupling is 46 GHz for the ground state of the SiV and $\epsilon_{A_{1g}}$, $\epsilon_{E_{gx}}$, and $\epsilon_{E_{gy}}$ are strain tensor components obeying the symmetries of the SiV center as defined in Chapter 2. We diagonalize the total Hamiltonian, $\mathbb{H}^{\text{total}}$, and calculate expectation values of the Pauli matrices for the lowest two eigenstates, which comprise the SiV spin-qubit

under investigation. This gives us the mean orientation of the SiV electron-spin, say $\mathbf{S}_1$ for given experimental conditions. To calculate the mean orientation of the proximal spin $\mathbf{S}_2$, we assume it to be either a nuclear spin such as ^{13}C, or an electron spin such as another SiV-center. In the case of a nuclear spin, $\mathbf{S}_2$ is simply given by the direction of the external magnetic field. Once the quantization axes of the two spins are known, we can fit our data to the calculated value of $\mathbb{H}^{\text{d-d}}$ from Eq. F.2 by using the distance between the spins $\mathbf{r}$ as a fit parameter. The result of such a fitting procedure is shown in Fig. F.2. In the case of a nuclear spin, the distance between the two spins $|\mathbf{r}|$ is estimated to be on the order of 1 Å. If the other spin is an electron spin from another SiV centre, it is possible to obtain similar results as in Fig. F.2. However, in this case, the distance between the spins is on the order of tens of nanometres.

Appendix G

Strain and spectral diffusion of the SiV

We discuss the question of whether applying a large amount of strain to the SiV induces extra spectral diffusion. In our experiments in Chapter 4, we do not observe any increase in spectral diffusion at high strain (high voltage). In theory, there are two potential causes of spectral diffusion that might appear at high strain. (i) The applied strain could perturb the inversion symmetry of the SiV-center, and induce a nonzero permanent dipole moment for the electronic levels. (ii) A large DC-electric field at the SiV location arising from the applied voltage could induce a linear Stark shift response to fluctuating electric-fields in the environment of the SiV, thereby increasing spectral diffusion. In our experiments, the amount of spectral diffusion on the timescale of minutes (roughly ± 20 MHz) does not appear to increase from the zero-voltage to the high-voltage condition (Fig. G.1). This is further confirmed by our measurements of the C transition linewidth at various high strain conditions. (Fig. G.2). We do observe a systematic drift in the transition frequency on the timescale of hours, but this slow drift can be easily corrected for by adjusting the resonant laser excitation frequency or alternatively by performing feedback on the DC voltage applied to our device. The latter approach is adopted in the two emitter experiment in

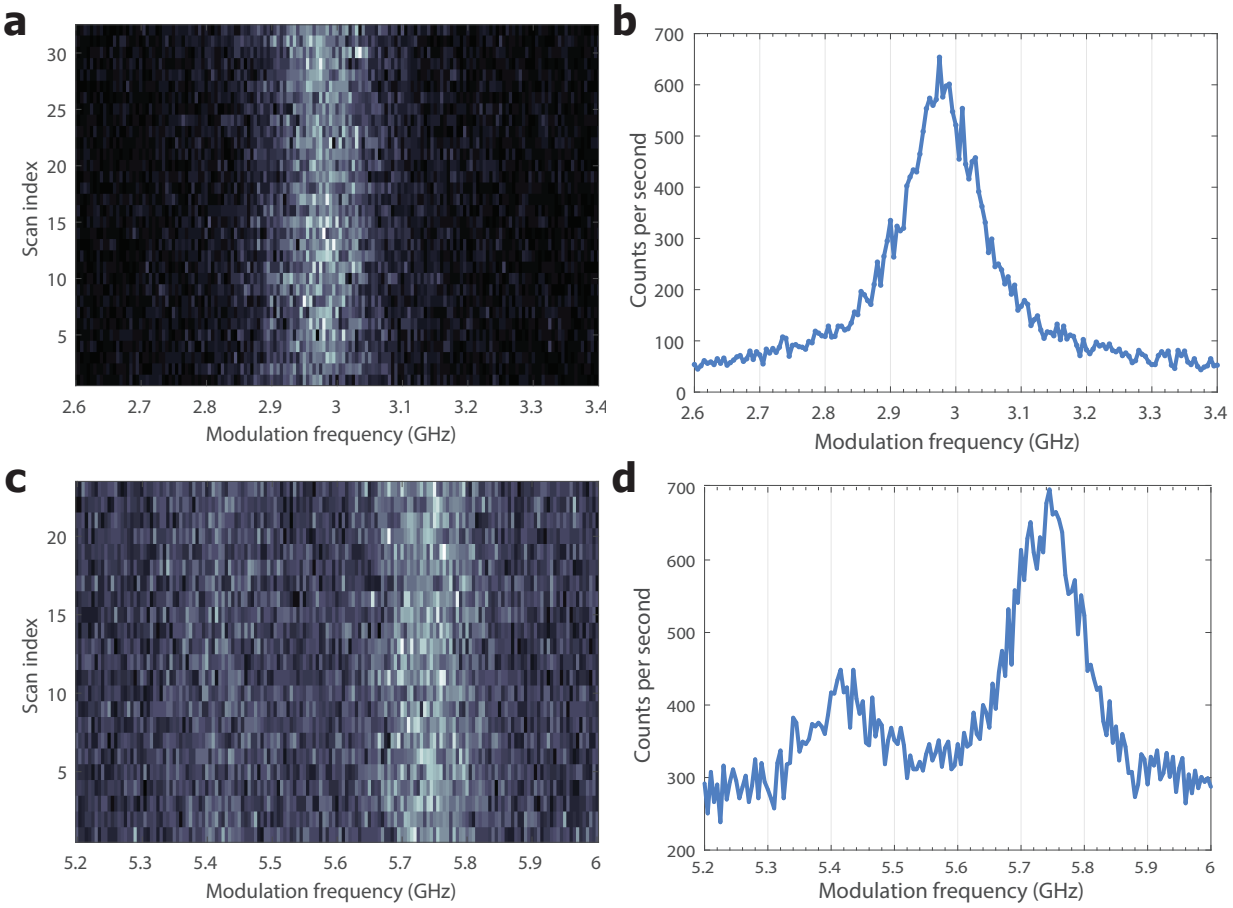

Figure G.1: (a) Continuous monitoring of the resonant excitation spectrum of the C transition at 0 V (ground state splitting of 88 GHz) and 0 T. Each horizontal line corresponds to a single acquisition of the spectrum over a duration of 0.6 s with 5 MHz spectral resolution. (b) Average of the 32 scans in part (a) corresponding to a total acquisition time of 20 s (c) Continuous monitoring of the resonant excitation spectrum of two of the four Zeeman-split C transitions at 400 V (ground state splitting of 303 GHz) and a B-field of 0.2 T. Each horizontal line corresponds to a single acquisition of the spectrum over a duration of 0.6 s with 5 MHz spectral resolution. (d) Average of the 23 scans in part (c) corresponding to a total acquisition time of 14 s.

Chapter 3 to maintain the C transitions of both emitters in resonance.

Over the course of this thesis, measurements were carried out on SiV centers in both bulk diamond and a variety of fabricated nanostructures. We made the general observation that SiVs in bulk diamond experience little to no spectral diffusion consistent with seminal experiments in[166]. However, we do observe spectral diffusion in nanostructures on the timescale of tens of seconds (Figures 3.2, I.5). The magnitude of diffusion increases in severity with reduction in size of the structure, thereby increasing proximity to surfaces. One potential cause for this effect could be the second order response to fluctuating elec-

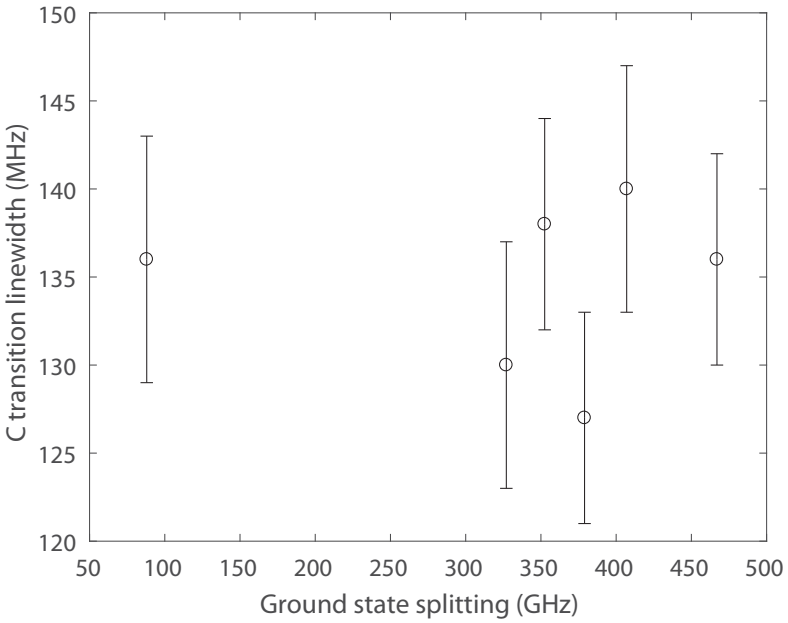

Figure G.2: Linewidth of the C transition measured at various strain conditions over a timescale of few minutes. Error bars are obtained from Lorentzian fits to the spectra.

tric fields determined by the dipole moment between the ground and excited states.

Appendix H

Additional effects of strain on the SiV qubit

H.1 Dispersive strain-coupling

From Eqs. (5.2, 5.3), we concluded that in the the low strain limit, the eigenstates of the SiV qubit $|e_{g-}\downarrow\rangle'$, $|e_{g+}\uparrow\rangle'$ are linearly mixed by E_g-strain, and hence suitable for resonant driving by AC strain at frequency ω_s. This type of mixing also indicates that static E_g-strain would cause a quadratic shift in the spin-transition frequency ω_s. Such a quadratic response to an external field can always generate a linear AC response in the presence of a 'bias' field. Thus in the presence of non-zero static E_g-strain, ω_s must also experience a linear modulation with off-resonant AC strain. This is particularly useful for parametric coupling of the qubit levels to off-resonant mechanical resonators as demonstrated previously with NV centers[66?,81,122]. A calculation of the magnitude of modulation in the spin transition frequency for a given AC strain $\epsilon^{AC}_{E_{gx}}$ yields the susceptibility t_{spin} for dispersive spin-phonon coupling, which can be of the same order of magnitude as d_{spin}.

$$t_{\text{spin}} = \frac{\langle e_{g+}\uparrow' \,|\mathbb{H}^{AC}_{str}|e_{g+}\uparrow'\rangle - \langle e_{g-}\downarrow' \,|\mathbb{H}^{AC}_{str}|e_{g-}\downarrow'\rangle}{\epsilon^{AC}_{E_{gx}}} d_{\text{gs}} \tag{H.1}$$

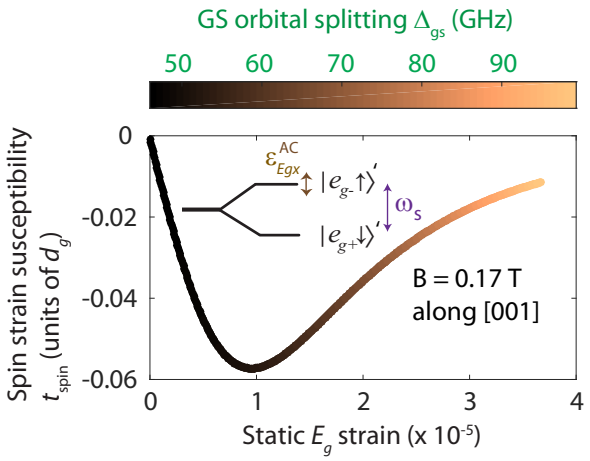

Figure H.1: Calculated susceptibility of the qubit levels for interaction with off-resonant AC E_g-strain that modulates the transition frequency ω_s (interaction shown in inset). Color variation along the curve shows the GS splitting corresponding to the value of static E_g-strain at the SiV. Both the DC and AC strain are assumed to be entirely in the E_{gx}-component.

t_{spin} is calculated as a function of pre-existing static E_g-strain, and plotted in Fig. H.1. Its magnitude is maximized at a moderately strained GS splitting of 50 GHz, and falls off as static strain is further increased. This non-monotonic behavior arises from the fact that t_{spin} is a result of linearizing the quadratic response due to d_{spin}, and therefore scales as the product of d_{spin} and static strain in the environment. Thus there is an optimal static strain condition to maximize t_{spin}.

H.2 Microwave magnetic response

At zero strain, qubit transitions cannot be driven by resonant microwave magnetic fields at frequency ω_s. This is because a magnetic field cannot flip the orbital character of the pure SO eigenstates $|e_{g-}\downarrow\rangle$, $|e_{g+}\uparrow\rangle$ as evinced by the Hamiltonian 5.1. However, just as a transverse magnetic field allows a strain susceptibility for the qubit levels as shown by Eqs. (5.2-5.4), we can argue that the presence of non-zero static strain induces a response to transverse magnetic fields. This is necessary for coherent control of the SiV spin with microwave fields[60,61]. Fig. H.2 shows this effect through a calculation of the effective g-

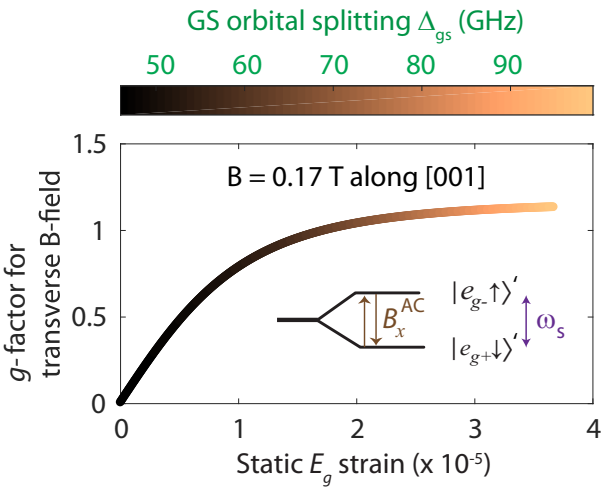

Figure H.2: Variation of g-factor for transverse magnetic field (orthogonal to the SiV internal z-axis) as a function of pre-existing static E_g-strain. Color variation along the curve shows the GS splitting corresponding to the value of static E_g-strain at the SiV. Static magnetic field that splits the spin sublevels is applied along the [001] direction, while microwave magnetic field resonantly driving the spin transition is applied along the SiV x-axis (interaction shown in inset). Static strain is assumed to be entirely of E_{gx}-character.

factor for magnetic field applied in the SiV transverse plane. It is zero at zero strain, and saturates as strain is increased far beyond the SO coupling. In the high strain regime, the system behaves like a free electron spin quantized along [001], the direction of the static magnetic field.

Appendix I

Experimental setup for chapters 3 and 6

I.1 Cryogenic confocal imaging and fiber coupling

The experiments in Chapters 3 and 6 were carried out using a closed-cycle 4K Helium Cryostat (Fusion F2 Montana Instruments) customized to allow for simultaneous confocal imaging and tapred fiber coupling to nanophotonic waveguides (Fig. I.1(a)). The position of the sample and the tapered fiber were controlled independently with two stacks of three piezo-based nanopositioning stages (Attocube: 2x ANP X101 and 1x z102 each) controlled with piezo controllers (ANC 300 and ANC 350 respectively) shown in Fig. I.1(b). A 0.9 NA 100×, 1 mm working distance objective (Olympus MPLFLN 100X) is housed inside the cryostat behind a radiation shield for spectroscopy of color centers (Fig. I.1(c)). For experiments that require a tunable magnetic field, a seventh nanopositioner (Attocube ANP X51) is placed on top of the sample positioners to translate a permanent magnet (K and J magnetics) placed behind the sample.

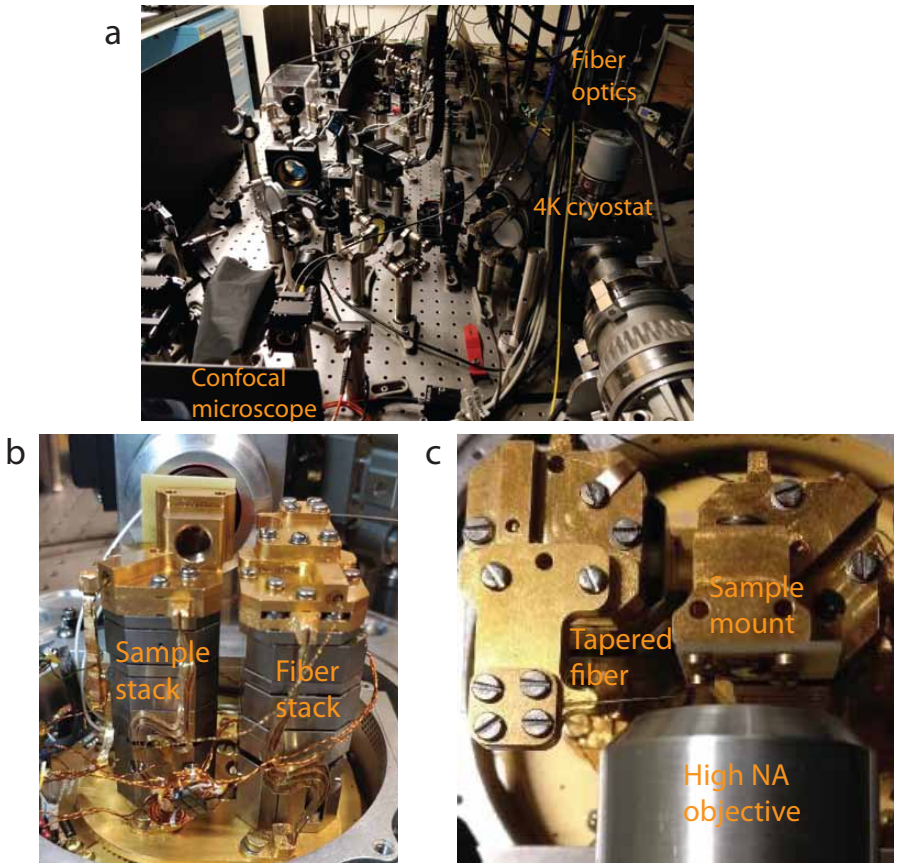

Figure I.1: (a) Photograph of experimental setup showing Montana 4 K cryostat with optics for a confocal microscope and fiber network. (b) Side view of XYZ sample and fiber mounts on two separate XYZ positioners inside the cryostat. (c) Top view showing tapered fiber probe and microscope objective behind a radiation shield.

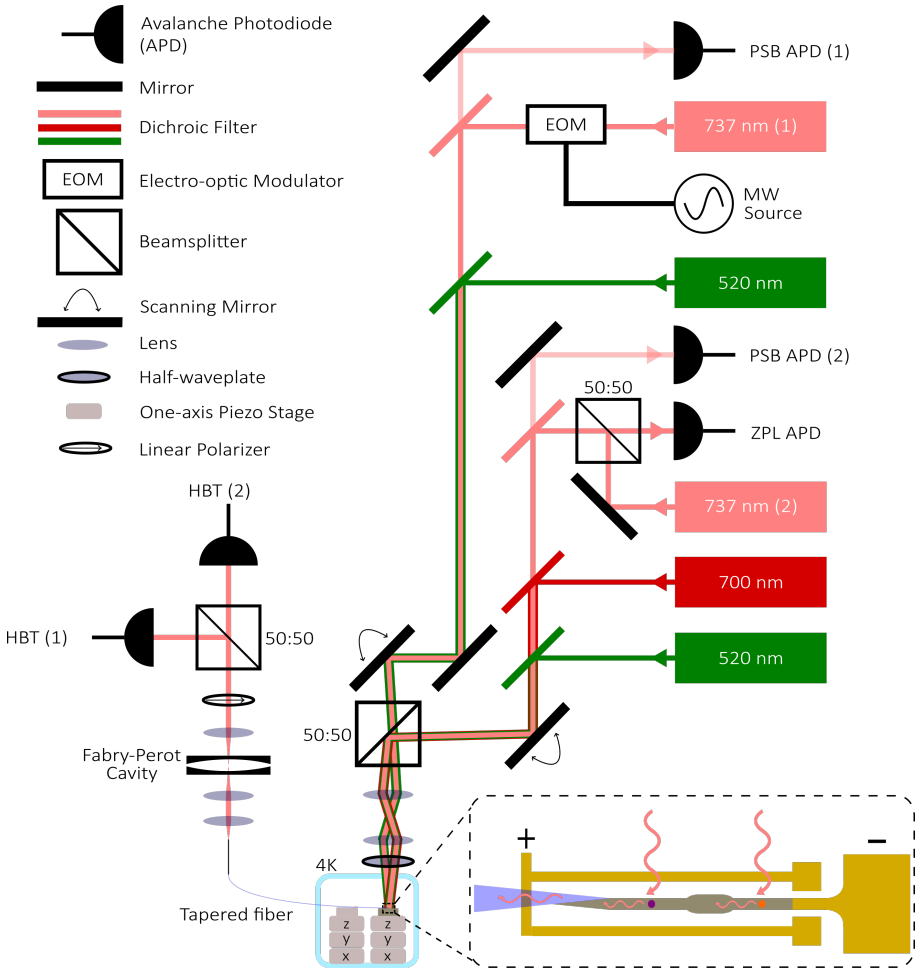

Figure I.2: Schematic of the setup used in the experiment in Chapter 3

I.2 Methods for Chapter 3

The layout of the setup used in Chapter 3 is shown in Fig. I.2. Strain was applied to the sample nanobeams by applying a voltage difference (from 0 to 100 volts) between two gold capacitor plates (Keithley Series 22020 voltage source). To allow for the independent excitation of spatially separated SiV centers, we set the location of the two independent excitation positions using two scanning mirrors (Newport FSM300 and Mad City Labs MCLS02813). We periodically pulsed a green laser (Thorlabs LP520 nm) to repump our SiV centers into the negative charge state. For identifying the location of the SiV centers within the diamond waveguide, an off-resonant 700 nm laser (Thorlabs M700F3) was scanned along the waveguide and the color center's zero-phonon line (ZPL) emission was

collected via free space using an avalanche photodiode (APD; 4X Perkin Elmer SPCM-AQRH-14-FC). Resonant excitation of SiV centers was performed using a continuous wave tunable Ti:Sapphire laser (M-Squared SolsTiS-2000-PSX-XF) and a homebuilt external-cavity diode laser (Opnext Diode HL7302MG, Littrow configuration) and the longer wavelength SiV phonon-sideband (PSB) emission was collected using a free-space APD. Fast modulation of the Ti:Sapphire laser sideband used in the feedback schemes described in Figure 3 was performed by sending the laser through an electro-optic modulator (iXBlue photonics NIR MX800) with a microwave frequency modulation input (HP 83711B, capable of operating up to 20 GHz).

A significant part of the SiV emission coupled to the diamond waveguide mode and was collected by a tapered optical fiber (collection efficiency of about 85%). This emission was then launched into free space and sent through a home-made, tunable, high-finesse (500 MHz linewidth, 150 GHz FSR) Fabry-Perot cavity frequency filter. This filter separated the SiV fluorescence from excitation laser photons scattered into the waveguide.

In the experiment involving two emitters, this frequency filter was used to guarantee successful spectral overlap of the two SiV centers' emission lines. Their emission then passed through a linear polarizer which erased any polarization mismatch (containing which-path information) between the two emitters, followed by a Hanbury-Brown Twiss (HBT) interferometer consisting of a 50:50 beam splitter (fiber coupled) with equal arm lengths and two APDs. A time correlator (Picoharp PH300) connected to the two APDs of the HBT interferometer was then used to measure the second-order photon correlation function.

The photon correlation function of indistinguishable emitters was obtained by programming the automatic start of the 0.5 second long measurement sequence conditioned on the APD count rate passing the set threshold value. This threshold value ensured that the photons emitted from both SiV centers passed through the Fabry-Perot cavity, which signified that their optical transitions were on resonance and the emitted photons were in-

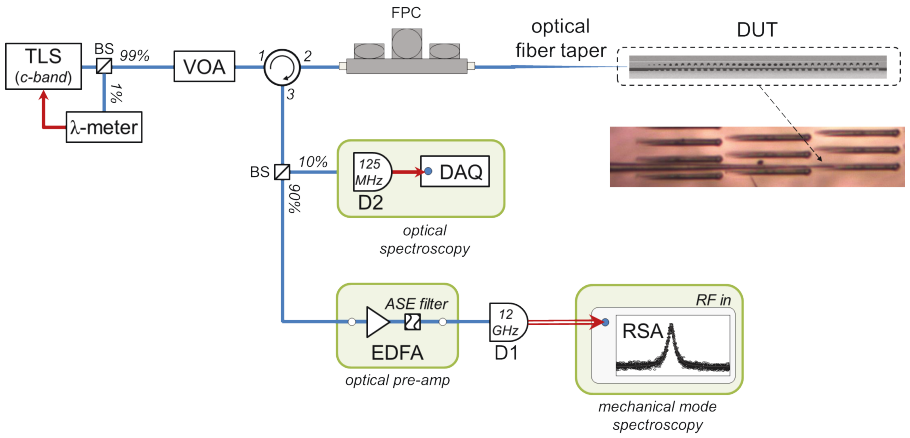

Figure I.3: Schematic of setup for OMC spectroscopy

distinguishable. In the case of the count rate dropping below the threshold value, strain would be applied until the count rate through the cavity filter was again maximized and the experiment would proceed. In the experiment measuring the photon correlation function of distinguishable emitters (Figure 4c, left panel), this overlap was not ensured and the polarizer was removed from the beam path, making the emitted photons distinguishable.

I.3 Spectroscopy of optomechanical crystals

A tunable laser source (TLS, Santec telecom c-Band TSL-510, 1480-1580 nm tuning bandwidth) was used to locate the optical cavity resonance. For general optical and radio frequency (RF) mechanical spectroscopy performed at low input powers, the laser pump was sent directly to a variable optical attenuator (VOA, EXFO FA-3150), before coupling into the DUT. After the VOA, laser light was first sent through a fiber polarization controller (FPC) and then into the tapered fiber. Optical reflection spectra from the device under test were collected as the tapered fiber is gradually bought into contact with the tapered waveguide section of the device under test. The reflected laser signal from the device was split (via a 90:10 coupler) between a low speed and high speed path, in order to collect the

optical cavity spectrum and mechanical cavity spectrum, respectively. In the high speed path, transmitted laser light is optically amplified by a second EDFA, with any amplified spontaneous emission (ASE) removed by a band pass filter (JDS Uniphase TB9) centered on the optical cavity resonance wavelength, and then detected by a high-bandwidth photoreceiver (D1, New Focus 1554-B, 12 GHz bandwidth). The high-bandwidth detector was connected to a real-time spectrum analyzer (RSA, Tektronix RSA 5126A) to measure photocurrent electronic power spectrum and monitor the mechanical cavity RF response. In the low speed path, transmitted laser light is sent to a high-gain low bandwidth photodetector (D2, New Focus 1811, 125 MHz bandwidth) used to measure the DC transmission response of the optical cavity. Thermometry of the mechanical mode was accomplished with a reference RF tone sent to an electro-optic phase modulator (EOPM, EOSpace Inc.) [CITE].

I.4 Magnetic field tuning

Experiments on SiV centers in OMCs are carried with tuning the magnetic field in the setup such that the splitting between the lowest spin-orbit ground states ω_s is swept across the mechanical mode ω_m. Prior to measurements geared to measure signatures of spin-phonon coupling, we calibrate the magnetic field at the SiV site with the motion of the positioner on which the permanent magnet is mounted. In Fig. I.4a, at step 0, the magnet is jammed against the sample and is slowly retracted. At each step, we take a resonant excitation spectrum of the C1 transition. This allows us to calibrate the tuning slope as shown in Fig. I.4b and identify the range of magnet positions for a fine sweep around the mechanical frequency as shown in Fig. I.4c. Ideally, one would perform such a calibration with a direct measurement of the spin resonance through ODMR or CPT. This would allow one to arrive at a narrower tuning range for the fine sweep of magnet position. Finer magnet positioning (up to KHz variation in ω_s) is possible by operating the positioner in

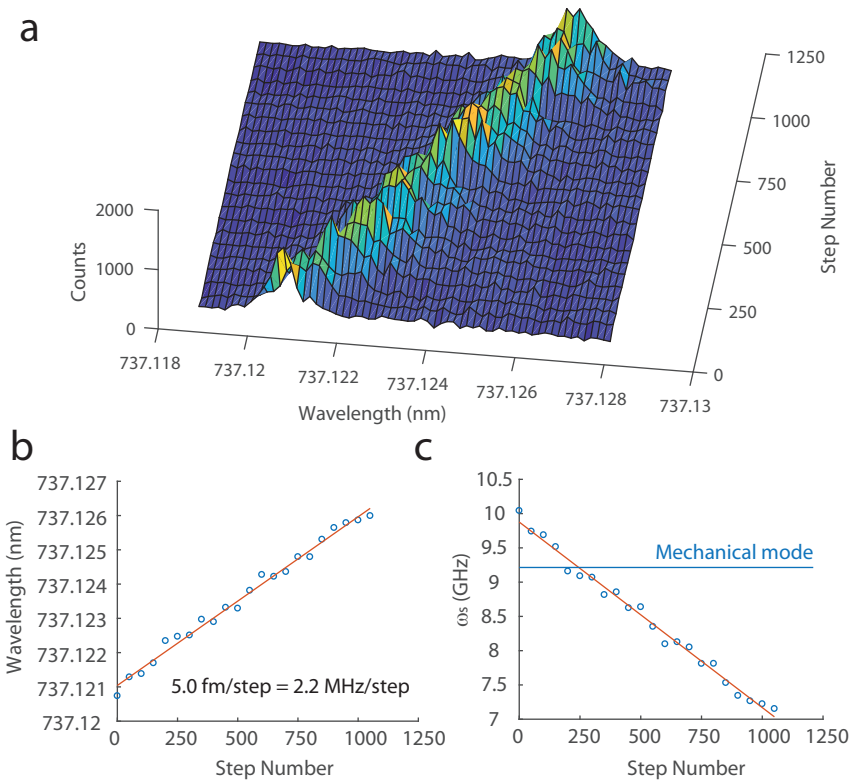

Figure I.4: Coarse tuning of the C1 transition of an SiV and calibration of magnetic field tuning. (a) Raw PLE spectra of the C1 transition against steps of the positioner (b) Center wavelength of C1 transition extracted from fits to spectra in part (a). (c) Corresponding tuning of SiV qubit transition frequency. Frequency of the mechanical mode is indicated with the horizontal line.

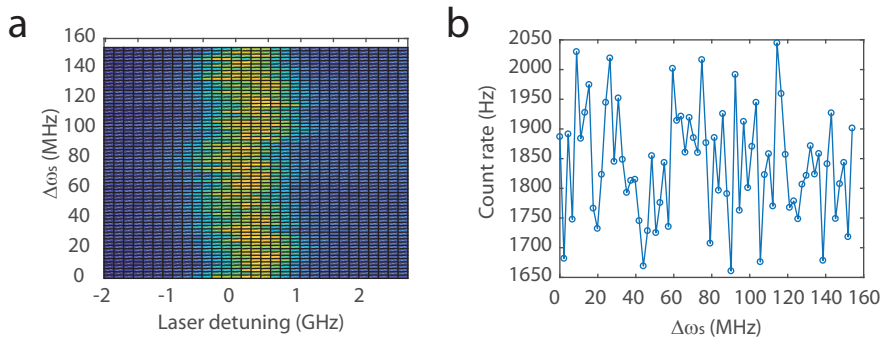

Figure I.5: Attempt to detect mechanical resonance in C1 fluorescence. (a) Raw PLE spectra of C1 transition plotted vs magnetic field tuning along y-axis (b) Variation in peak count rate with magnetic field tuning along x-axis.

continuous mode as opposed to the slip-stick mode used in these measurements.

Figure I.5a shows the C1 transition over a fine sweep of the magnet position around the expected resonance condition between ω_s and ω_m. In Fig. I.5b, we extract the peak intensity from a Lorentzian fit to each spectrum, essentially a measure of the population in the qubit excited state $|e_{g-} \uparrow\rangle$ as it is tuned across the mechanical mode. We do not see the effect of enhance spin relaxation from the mechanical mode potentially due to the SiV being relatively high strain (GS splitting of 150 GHz) lowering the strain susceptibility of the qubit transition according to the observations of Chapter 5.

References

[1] Michael A. Nielsen and Isaac L. Chuang. *Quantum Computation and Quantum Information: 10th Anniversary Edition*. Cambridge University Press, 2010.

[2] Aram W. Harrow and Ashley Montanaro. Quantum computational supremacy. *Nature*, 549:203–209, 2017.

[3] H. Bernien, B. Hensen, W. Pfaff, G. Koolstra, M. S. Blok, L. Robledo, T. H. Taminiau, M. Markham, D. J. Twitchen, L. Childress, and R. Hanson. Heralded entanglement between solid-state qubits separated by three metres. *Nature*, 497(7447):86–90, April 2013.

[4] W. Pfaff, B. J. Hensen, H. Bernien, S. B. van Dam, M. S. Blok, T. H. Taminiau, M. J. Tiggelman, R. N. Schouten, M. Markham, D. J. Twitchen, and R. Hanson. Unconditional quantum teleportation between distant solid-state quantum bits. *Science*, 345(6196):532–535, 2014.

[5] Stephanie Wehner, David Elkouss, and Ronald Hanson. Quantum internet: A vision for the road ahead. *Science*, 362(6412), 2018.

[6] Kevin S. Chou, Jacob Z. Blumoff, Christopher S. Wang, Philip C. Reinhold, Christopher J. Axline, Yvonne Y. Gao, L. Frunzio, M. H. Devoret, Liang Jiang, and R. J. Schoelkopf. Deterministic teleportation of a quantum gate between two logical qubits. *Nature*, 561:368–373, 2018.

[7] M. H. Abobeih, J. Cramer, M. A. Bakker, N. Kalb, M. Markham, D. J. Twitchen, and T. H. Taminiau. One-second coherence for a single electron spin coupled to a multi-qubit nuclear-spin environment. *Nature Communications*, 9:2552, 2018.

[8] J. L. O'Brien, S. R. Schofield, M. Y. Simmons, R. G. Clark, A. S. Dzurak, N. J. Curson, B. E. Kane, N. S. McAlpine, M. E. Hawley, and G. W. Brown. Towards the fabrication of phosphorus qubits for a silicon quantum computer. *Phys. Rev. B*, 64:161401, Sep 2001.

[9] H. J. Kimble. The quantum internet. *Nature*, 453(7198):1023–1030, June 2008.

[10] P. Rabl, S. J. Kolkowitz, F. H. L. Koppens, J. G. E. Harris, P. Zoller, and M. D. Lukin. A quantum spin transducer based on nanoelectromechanical resonator arrays. *Nature Physics*, 6(8):602–608, August 2010.

[11] Margareta Wallquist, Klemens Hammerer, Peter Rabl, Mikhail Lukin, and Peter Zoller. Hybrid quantum devices and quantum engineering. *Physica Scripta*, 2009(T137):014001, 2009.

[12] David M. Toyli, Christoph D. Weis, Gregory D. Fuchs, Thomas Schenkel, and David D. Awschalom. Chip-scale nanofabrication of single spins and spin arrays in diamond. *Nano Letters*, 10(8):3168–3172, 2010. PMID: 20698632.

[13] Tim Schröder, Matthew E. Trusheim, Michael Walsh, Luozhou Li, Jiabao Zheng, Marco Schukraft, Alp Sipahigil, Ruffin E. Evans, Denis D. Sukachev, Christian T. Nguyen, Jose L. Pacheco, Ryan M. Camacho, Edward S. Bielejec, Mikhail D. Lukin, and Dirk Englund. Scalable focused ion beam creation of nearly lifetime-limited single quantum emitters in diamond nanostructures. *Nature Communications*, 8:15376, May 2017.

[14] Sungkun Hong, Michael S. Grinolds, Linh M. Pham, David Le Sage, Lan Luan, Ronald L. Walsworth, and Amir Yacoby. Nanoscale magnetometry with nv centers in diamond. *MRS Bulletin*, 38(2):155–161, 2013.

[15] Serge Haroche. Nobel lecture: Controlling photons in a box and exploring the quantum to classical boundary. *Rev. Mod. Phys.*, 85:1083–1102, Jul 2013.

[16] Stephan Welte, Bastian Hacker, Severin Daiss, Stephan Ritter, and Gerhard Rempe. Photon-mediated quantum gate between two neutral atoms in an optical cavity. *Phys. Rev. X*, 8:011018, Feb 2018.

[17] R. E. Evans, M. K. Bhaskar, D. D. Sukachev, C. T. Nguyen, A. Sipahigil, M. J. Burek, B. Machielse, G. H. Zhang, A. S. Zibrov, E. Bielejec, H. Park, M. Lončar, and M. D. Lukin. Photon-mediated interactions between quantum emitters in a diamond nanocavity. *Science*, 362(6415):662–665, 2018.

[18] J. Majer, J. M. Chow, J. M. Gambetta, Jens Koch, B. R. Johnson, J. A. Schreier, L. Frunzio, D. I. Schuster, A. A. Houck, A. Wallraff, A. Blais, M. H. Devoret, S. M. Girvin, and R. J. Schoelkopf. Coupling superconducting qubits via a cavity bus. *Nature*, 449:443 EP –, Sep 2007.

[19] Michael J. Burek, Charles Meuwly, Ruffin E. Evans, Mihir K. Bhaskar, Alp Sipahigil, Srujan Meesala, Bartholomeus Machielse, Denis D. Sukachev, Christian T. Nguyen, Jose L. Pacheco, Edward Bielejec, Mikhail D. Lukin, and Marko Lončar. Fiber-Coupled Diamond Quantum Nanophotonic Interface. *Phys. Rev. Applied*, 8(2), August 2017.

[20] Markus Aspelmeyer, Tobias J. Kippenberg, and Florian Marquardt. Cavity optomechanics. *Rev. Mod. Phys.*, 86:1391–1452, Dec 2014.

[21] Jasper Chan, T. P. Mayer Alegre, Amir H. Safavi-Naeini, Jeff T. Hill, Alex Krause, Simon Gröblacher, Markus Aspelmeyer, and Oskar Painter. Laser cooling of a nanomechanical oscillator into its quantum ground state. *Nature*, 478:89–92, 2011.

[22] Sungkun Hong, Ralf Riedinger, Igor Marinković, Andreas Wallucks, Sebastian G. Hofer, Richard A. Norte, Markus Aspelmeyer, and Simon Gröblacher. Hanbury brown and twiss interferometry of single phonons from an optomechanical resonator. *Science*, 2017.

[23] Ralf Riedinger, Andreas Wallucks, Igor Marinković, Clemens Löschnauer, Markus Aspelmeyer, Sungkun Hong, and Simon Gröblacher. Remote quantum entanglement between two micromechanical oscillators. *Nature*, 556:473–477, 2018.

[24] Gregory S MacCabe, Hengjiang Ren, Jie Luo, Justin D Cohen, Hengyun Zhou, Alp Sipahigil, Mohammad Mirhosseini, and Oskar Painter. Phononic bandgap nano-acoustic cavity with ultralong phonon lifetime. *arXiv preprint arXiv:1901.04129*, 2019.

[25] A. D. O'Connell, M. Hofheinz, M. Ansmann, Radoslaw C. Bialczak, M. Lenander, Erik Lucero, M. Neeley, D. Sank, H. Wang, M. Weides, J. Wenner, John M. Martinis, and A. N. Cleland. Quantum ground state and single-phonon control of a mechanical resonator. *Nature*, 464(7289):697–703, April 2010.

[26] Yiwen Chu, Prashanta Kharel, William H. Renninger, Luke D. Burkhart, Luigi Frunzio, Peter T. Rakich, and Robert J. Schoelkopf. Quantum acoustics with superconducting qubits. *Science*, 2017.

[27] R. W. Andrews, R. W. Peterson, T. P. Purdy, K. Cicak, R. W. Simmonds, C. A. Regal, and K. W. Lehnert. Bidirectional and efficient conversion between microwave and optical light. *Nature Physics*, 10:321–326, 2014.

[28] A. P. Higginbotham, P. S. Burns, M. D. Urmey, R. W. Peterson, N. S. Kampel, B. M. Brubaker, G. Smith, K. W. Lehnert, and C. A. Regal. Harnessing electro-optic correlations in an efficient mechanical converter. *Nature Physics*, 14:1038–1042, 2018.

[29] S. Kolkowitz, A. C. Bleszynski Jayich, Q. P. Unterreithmeier, S. D. Bennett, P. Rabl, J. G. E. Harris, and M. D. Lukin. Coherent Sensing of a Mechanical Resonator with a Single-Spin Qubit. *Science*, 335(6076):1603–1606, March 2012.

[30] Sungkun Hong, Michael S. Grinolds, Patrick Maletinsky, Ronald L. Walsworth, Mikhail D. Lukin, and Amir Yacoby. Coherent, Mechanical Control of a Single Electronic Spin. *Nano Lett.*, 12(8):3920–3924, August 2012.

[31] O. Arcizet, V. Jacques, A. Siria, P. Poncharal, P. Vincent, and S. Seidelin. A single nitrogen-vacancy defect coupled to a nanomechanical oscillator. *Nature Physics*, 7(11):879–883, September 2011.

[32] I. Wilson-Rae, P. Zoller, and A. Imamoğlu. Laser Cooling of a Nanomechanical Resonator Mode to its Quantum Ground State. *Phys. Rev. Lett.*, 92(7), February 2004.

[33] Ö. O. Soykal, Rusko Ruskov, and Charles Tahan. Sound-based analogue of cavity quantum electrodynamics in silicon. *Phys. Rev. Lett.*, 107:235502, Nov 2011.

[34] Arthur Marshall Stoneham. *Theory of defects in solids: electronic structure of defects in insulators and semiconductors*. Oxford University Press, 2001.

[35] Matthias Imboden and Pritiraj Mohanty. Dissipation in nanoelectromechanical systems. *Physics Reports*, 534(3):89–146, January 2014.

[36] R. C. Zeller and R. O. Pohl. Thermal conductivity and specific heat of noncrystalline solids. *Phys. Rev. B*, 4:2029–2041, Sep 1971.

[37] W. Arnold and S. Hunklinger. Experimental evidence for the direct interaction between two-level systems in glasses at very low temperatures. *Solid State Communications*, 17(7):883 – 886, 1975.

[38] J. L. Black and B. I. Halperin. Spectral diffusion, phonon echoes, and saturation recovery in glasses at low temperatures. *Phys. Rev. B*, 16:2879–2895, Sep 1977.

[39] Birgit J.M. Hausmann, Mughees Khan, Yinan Zhang, Tom M. Babinec, Katie Martinick, Murray McCutcheon, Phil R. Hemmer, and Marko Lončar. Fabrication of diamond nanowires for quantum information processing applications. *Diamond and Related Materials*, 19(5-6):621–629, May 2010.

[40] Birgit J. M. Hausmann, Brendan Shields, Qimin Quan, Patrick Maletinsky, Murray McCutcheon, Jennifer T. Choy, Tom M. Babinec, Alexander Kubanek, Amir Yacoby, Mikhail D. Lukin, and Marko Lončar. Integrated Diamond Networks for Quantum Nanophotonics. *Nano Lett.*, 12(3):1578–1582, March 2012.

[41] Michael J. Burek, Nathalie P. de Leon, Brendan J. Shields, Birgit J. M. Hausmann, Yiwen Chu, Qimin Quan, Alexander S. Zibrov, Hongkun Park, Mikhail D. Lukin, and Marko Lončar. Free-Standing Mechanical and Photonic Nanostructures in Single-Crystal Diamond. *Nano Lett.*, 12(12):6084–6089, December 2012.

[42] Y. Tao, J. M. Boss, B. A. Moores, and C. L. Degen. Single-crystal diamond nanomechanical resonators with quality factors exceeding one million. *Nature Communications*, 5, April 2014.

[43] Behzad Khanaliloo, Matthew Mitchell, Aaron C. Hryciw, and Paul E. Barclay. High-Q / V Monolithic Diamond Microdisks Fabricated with Quasi-isotropic Etching. *Nano Lett.*, 15(8):5131–5136, August 2015.

[44] P. Ovartchaiyapong, L. M. A. Pascal, B. A. Myers, P. Lauria, and A. C. Bleszynski Jayich. High quality factor single-crystal diamond mechanical resonators. *Applied Physics Lett.*, 101(16):163505, October 2012.

[45] Behzad Khanaliloo, Harishankar Jayakumar, Aaron C. Hryciw, David P. Lake, Hamidreza Kaviani, and Paul E. Barclay. Single-Crystal Diamond Nanobeam Waveguide Optomechanics. *Phys. Rev. X*, 5(4), December 2015.

[46] Michael J. Burek, Daniel Ramos, Parth Patel, Ian W. Frank, and Marko Lončar. Nanomechanical resonant structures in single-crystal diamond. *Applied Physics Lett.*, 103(13):131904, September 2013.

[47] W. Weaver Jr, S. P. Timoshenko, and D. H. Young. *Vibration Problems in Engineering*. John Wiley & Sons, February 1990. Google-Books-ID: YZ7t8LgRqi0C.

[48] William F. Koehl, Bob B. Buckley, F. Joseph Heremans, Greg Calusine, and David D. Awschalom. Room temperature coherent control of defect spin qubits in silicon carbide. *Nature*, 479:84–87, 2011.

[49] M. Koperski, K. Nogajewski, V. Cherkez A. Arora, P. Mallet, J.-Y. Veuillen, J. Marcus, P. Kossacki, and M. Potemski. Single photon emitters in exfoliated wse_2 structures. *Nature Nanotechnology*, 10:503–506, 2015.

[50] Adam Gali and Jeronimo R Maze. Ab initio study of the split silicon-vacancy defect in diamond: Electronic structure and related properties. *Phys. Rev. B*, 88(23):235205, 2013.

[51] Tina Müller, Christian Hepp, Benjamin Pingault, Elke Neu, Stefan Gsell, Matthias Schreck, Hadwig Sternschulte, Doris Steinmüller-Nethl, Christoph Becher, and Mete Atatüre. Optical signatures of silicon-vacancy spins in diamond. *Nature Communications*, 5, February 2014.

[52] A. Sipahigil, K. D. Jahnke, L. J. Rogers, T. Teraji, J. Isoya, A. S. Zibrov, F. Jelezko, and M. D. Lukin. Indistinguishable Photons from Separated Silicon-Vacancy Centers in Diamond. *Phys. Rev. Lett.*, 113(11), September 2014.

[53] Christian Hepp. *Electronic structure of the silicon vacancy color center in diamond*. PhD thesis, Universität des Saarlandes, 2014.

[54] B. J. M. Hausmann, B. J. Shields, Q. Quan, Y. Chu, N. P. de Leon, R. Evans, M. J. Burek, A. S. Zibrov, M. Markham, D. J. Twitchen, H. Park, M. D. Lukin, and M. Loncăr. Coupling of NV Centers to Photonic Crystal Nanobeams in Diamond. *Nano Lett.*, 13(12):5791–5796, December 2013.

[55] Andrei Faraon, Charles Santori, Zhihong Huang, Victor M. Acosta, and Raymond G. Beausoleil. Coupling of Nitrogen-Vacancy Centers to Photonic Crystal Cavities in Monocrystalline Diamond. *Phys. Rev. Lett.*, 109(3), July 2012.

[56] A. Sipahigil, R. E. Evans, D. D. Sukachev, M. J. Burek, J. Borregaard, M. K. Bhaskar, C. T. Nguyen, J. L. Pacheco, H. A. Atikian, C. Meuwly, R. M. Camacho, F. Jelezko, E. Bielejec, H. Park, M. Lončar, and M. D. Lukin. An integrated diamond nanophotonics platform for quantum-optical networks. *Science*, 354(6314):847–850, November 2016.

[57] N. Bar-Gill, L.M. Pham, A. Jarmola, D. Budker, and R.L. Walsworth. Solid-state electronic spin coherence time approaching one second. *Nature Communications*, 4:1743, April 2013.

[58] Lachlan J. Rogers, Kay D. Jahnke, Mathias H. Metsch, Alp Sipahigil, Jan M. Binder, Tokuyuki Teraji, Hitoshi Sumiya, Junichi Isoya, Mikhail D. Lukin, Philip Hemmer, and Fedor Jelezko. All-Optical Initialization, Readout, and Coherent Preparation of Single Silicon-Vacancy Spins in Diamond. *Phys. Rev. Lett.*, 113(26), December 2014.

[59] Kay D Jahnke, Alp Sipahigil, Jan M Binder, Marcus W Doherty, Mathias Metsch, Lachlan J Rogers, Neil B Manson, Mikhail D Lukin, and Fedor Jelezko. Electron–phonon processes of the silicon-vacancy centre in diamond. *New Journal of Physics*, 17(4):043011, April 2015.

[60] Benjamin Pingault, David-Dominik Jarausch, Christian Hepp, Lina Klintberg, Jonas N. Becker, Matthew Markham, Christoph Becher, and Mete Atatüre. Coherent control of the silicon-vacancy spin in diamond. *Nature Communications*, 8:15579, May 2017.

[61] Denis D Sukachev, Alp Sipahigil, Christian T Nguyen, Mihir K Bhaskar, Ruffin E Evans, Fedor Jelezko, and Mikhail D Lukin. Silicon-vacancy spin qubit in diamond: A quantum memory exceeding 10 ms with single-shot state readout. *Phys. Rev. Lett.*, 119:223602, Nov 2017.

[62] M. Metcalfe, S. M. Carr, A. Muller, G. S. Solomon, and J. Lawall. Resolved Sideband Emission of InAs / GaAs Quantum Dots Strained by Surface Acoustic Waves. *Phys. Rev. Lett.*, 105(3), July 2010.

[63] I. Yeo, P-L. de Assis, A. Gloppe, E. Dupont-Ferrier, P. Verlot, N. S. Malik, E. Dupuy, J. Claudon, J-M. Gérard, A. Auffèves, G. Nogues, S. Seidelin, J-Ph. Poizat, O. Arcizet, and M. Richard. Strain-mediated coupling in a quantum dot–mechanical oscillator hybrid system. *Nature Nanotechnology*, 9(2):106–110, December 2013.

[64] S. D. Bennett, N. Y. Yao, J. Otterbach, P. Zoller, P. Rabl, and M. D. Lukin. Phonon-Induced Spin-Spin Interactions in Diamond Nanostructures: Application to Spin Squeezing. *Phys. Rev. Lett.*, 110(15), April 2013.

[65] R. J. Sewell, M. Koschorreck, M. Napolitano, B. Dubost, N. Behbood, and M. W. Mitchell. Magnetic Sensitivity Beyond the Projection Noise Limit by Spin Squeezing. *Phys. Rev. Lett.*, 109(25), December 2012.

[66] Preeti Ovartchaiyapong, Kenneth W. Lee, Bryan A. Myers, and Ania C. Bleszynski Jayich. Dynamic strain-mediated coupling of a single diamond spin to a mechanical resonator. *Nature Communications*, 5, July 2014.

[67] J. Teissier, A. Barfuss, P. Appel, E. Neu, and P. Maletinsky. Strain Coupling of a Nitrogen-Vacancy Center Spin to a Diamond Mechanical Oscillator. *Phys. Rev. Lett.*, 113(2), July 2014.

[68] E. R. MacQuarrie, T. A. Gosavi, N. R. Jungwirth, S. A. Bhave, and G. D. Fuchs. Mechanical Spin Control of Nitrogen-Vacancy Centers in Diamond. *Phys. Rev. Lett.*, 111(22), November 2013.

[69] E. R. MacQuarrie, T. A. Gosavi, A. M. Moehle, N. R. Jungwirth, S. A. Bhave, and G. D. Fuchs. Coherent control of a nitrogen-vacancy center spin ensemble with a diamond mechanical resonator. *Optica*, 2(3):233, March 2015.

[70] E. R. MacQuarrie, T. A. Gosavi, S. A. Bhave, and G. D. Fuchs. Continuous dynamical decoupling of a single diamond nitrogen-vacancy center spin with a mechanical resonator. *Phys. Rev. B*, 92(22), December 2015.

[71] K.-M. C. Fu, C. Santori, P. E. Barclay, and R. G. Beausoleil. Conversion of neutral nitrogen-vacancy centers to negatively charged nitrogen-vacancy centers through selective oxidation. *Applied Physics Lett.*, 96(12):121907, March 2010.

[72] Shanying Cui, Andrew S. Greenspon, Kenichi Ohno, Bryan A. Myers, Ania C. Bleszynski Jayich, David D. Awschalom, and Evelyn L. Hu. Reduced Plasma-Induced Damage to Near-Surface Nitrogen-Vacancy Centers in Diamond. *Nano Lett.*, 15(5):2887–2891, May 2015.

[73] P. Siyushev, H. Pinto, M. Vörös, A. Gali, F. Jelezko, and J. Wrachtrup. Optically Controlled Switching of the Charge State of a Single Nitrogen-Vacancy Center in Diamond at Cryogenic Temperatures. *Phys. Rev. Lett.*, 110(16), April 2013.

[74] Y. Chu, N.P. de Leon, B.J. Shields, B. Hausmann, R. Evans, E. Togan, M. J. Burek, M. Markham, A. Stacey, A.S. Zibrov, A. Yacoby, D.J. Twitchen, M. Loncar, H. Park, P. Maletinsky, and M.D. Lukin. Coherent Optical Transitions in Implanted Nitrogen Vacancy Centers. *Nano Lett.*, 14(4):1982–1986, April 2014.

[75] Nathalie de Leon, Ruffin Evans, Kristiaan de Greve, Michael Goldman, Alex High, Matthew Markham, Alastair Stacey, Daniel Twitchen, Marko Loncar, Hongkun Park, and Mikhail Lukin. Quantum Optics in the Solid State with Diamond Nanophotonics. In *APS Division of Atomic, Molecular and Optical Physics Meeting Abstracts*, May 2015.

[76] Daniel Ramos, Eduardo Gil-Santos, Valerio Pini, Jose M Llorens, Marta Fernández-Regúlez, Álvaro San Paulo, M Calleja, and J Tamayo. Optomechanics with Silicon Nanowires by Harnessing Confined Electromagnetic Modes. *Nano Lett.*, 12(2):932–937, February 2012.

[77] M. W. Doherty, F. Dolde, H. Fedder, F. Jelezko, J. Wrachtrup, N. B. Manson, and L. C. L. Hollenberg. Theory of the ground-state spin of the NV − center in diamond. *Phys. Rev. B*, 85(20), May 2012.

[78] Marcus W. Doherty, Viktor V. Struzhkin, David A. Simpson, Liam P. McGuinness, Yufei Meng, Alastair Stacey, Timothy J. Karle, Russell J. Hemley, Neil B. Manson, Lloyd C. L. Hollenberg, and Steven Prawer. Electronic Properties and Metrology

Applications of the Diamond NV − Center under Pressure. *Phys. Rev. Lett.*, 112(4), January 2014.

[79] Michael S. J. Barson, Phani Peddibhotla, Preeti Ovartchaiyapong, Kumaravelu Ganesan, Richard L. Taylor, Matthew Gebert, Zoe Mielens, Berndt Koslowski, David A. Simpson, Liam P. McGuinness, Jeffrey McCallum, Steven Prawer, Shinobu Onoda, Takeshi Ohshima, Ania C. Bleszynski Jayich, Fedor Jelezko, Neil B. Manson, and Marcus W. Doherty. Nanomechanical sensing using spins in diamond. *Nano Letters*, 17(3):1496–1503, 2017. PMID: 28146361.

[80] J R Maze, A Gali, E Togan, Y Chu, A Trifonov, E Kaxiras, and M D Lukin. Properties of nitrogen-vacancy centers in diamond: the group theoretic approach. *New Journal of Physics*, 13(2):025025, February 2011.

[81] A. Barfuss, J. Teissier, E. Neu, A. Nunnenkamp, and P. Maletinsky. Strong mechanical driving of a single electron spin. *Nature Physics*, 11(10):820–824, August 2015.

[82] L. Childress, M. V. Gurudev Dutt, J. M. Taylor, A. S. Zibrov, F. Jelezko, J. Wrachtrup, P. R. Hemmer, and M. D. Lukin. Coherent Dynamics of Coupled Electron and Nuclear Spin Qubits in Diamond. *Science*, 314(5797):281–285, October 2006.

[83] Young-Ik Sohn, Michael J. Burek, Vural Kara, Ryan Kearns, and Marko Lončar. Dynamic actuation of single-crystal diamond nanobeams. *Applied Physics Lett.*, 107(24):243106, December 2015.

[84] Michael J. Burek, Justin D. Cohen, Seán M. Meenehan, Nayera El-Sawah, Cleaven Chia, Thibaud Ruelle, Srujan Meesala, Jake Rochman, Haig A. Atikian, Matthew Markham, Daniel J. Twitchen, Mikhail D. Lukin, Oskar Painter, and Marko Lončar. Diamond optomechanical crystals. *Optica*, 3(12):1404, December 2016.

[85] Atac Imamoğlu. Cavity QED Based on Collective Magnetic Dipole Coupling: Spin Ensembles as Hybrid Two-Level Systems. *Phys. Rev. Lett.*, 102(8), February 2009.

[86] Gordon Davies and MF Hamer. Optical studies of the 1.945 eV vibronic band in diamond. In *Proceedings of the Royal Society of London A: Mathematical, Physical and Engineering Sciences*, volume 348, pages 285–298. The Royal Society, 1976.

[87] A. Batalov, V. Jacques, F. Kaiser, P. Siyushev, P. Neumann, L. J. Rogers, R. L. McMurtrie, N. B. Manson, F. Jelezko, and J. Wrachtrup. Low Temperature Studies of the Excited-State Structure of Negatively Charged Nitrogen-Vacancy Color Centers in Diamond. *Phys. Rev. Lett.*, 102(19), May 2009.

[88] H Sternschulte, K Thonke, R Sauer, PC Münzinger, and P Michler. 1.681-eV luminescence center in chemical-vapor-deposited homoepitaxial diamond films. *Phys. Rev. B*, 50(19):14554, 1994.

[89] Aymeric Delteil, Zhe Sun, Wei-bo Gao, Emre Togan, Stefan Faelt, and Atac Imamoglu. Generation of heralded entanglement between distant hole spins. *Nature Physics*, 12(3):218–223, 2016.

[90] R. Stockill, M. J. Stanley, L. Huthmacher, E. Clarke, M. Hugues, A. J. Miller, C. Matthiesen, C. Le Gall, and M. Atatüre. Phase-tuned entangled state generation between distant spin qubits. *Phys. Rev. Lett.*, 119:010503, Jul 2017.

[91] Jonas Nils Becker, Benjamin Pingault, David Groß, Mustafa Gündoğan, Nadezhda Kukharchyk, Matthew Markham, Andrew Edmonds, Mete Atatüre, Pavel Bushev, and Christoph Becher. All-optical control of the silicon-vacancy spin in diamond at millikelvin temperatures. *arXiv preprint arXiv:1708.08263*, 2017.

[92] Haig A Atikian, Pawel Latawiec, Michael J Burek, Young-Ik Sohn, Srujan Meesala, Normand Gravel, Ammar B Kouki, and Marko Lončar. Freestanding nanostructures via reactive ion beam angled etching. *APL Photonics*, 2(5):051301, 2017.

[93] Ruffin E. Evans, Alp Sipahigil, Denis D. Sukachev, Alexander S. Zibrov, and Mikhail D. Lukin. Narrow-Linewidth Homogeneous Optical Emitters in Diamond Nanostructures via Silicon Ion Implantation. *Phys. Rev. Applied*, 5(4), April 2016.

[94] V. M. Acosta, C. Santori, A. Faraon, Z. Huang, K.-M. C. Fu, A. Stacey, D. A. Simpson, K. Ganesan, S. Tomljenovic-Hanic, A. D. Greentree, S. Prawer, and R. G. Beausoleil. Dynamic Stabilization of the Optical Resonances of Single Nitrogen-Vacancy Centers in Diamond. *Phys. Rev. Lett.*, 108(20), May 2012.

[95] A. E. Hughes and W. A. Runciman. Uniaxial stress splitting of doubly degenerate states of tetragonal and trigonal centres in cubic crystals. *Proceedings of the Physical Society*, 90(3):827, 1967.

[96] H.-J. Briegel, W. Dür, J. I. Cirac, and P. Zoller. Quantum repeaters: The role of imperfect local operations in quantum communication. *Phys. Rev. Lett.*, 81:5932–5935, Dec 1998.

[97] L.-M. Duan, M. D. Lukin, J. I. Cirac, and P. Zoller. Long-distance quantum communication with atomic ensembles and linear optics. *Nature*, 414:413 EP –, Nov 2001. Article.

[98] Juan Ignacio Cirac, Peter Zoller, H Jeff Kimble, and Hideo Mabuchi. Quantum state transfer and entanglement distribution among distant nodes in a quantum network. *Phys. Rev. Lett.*, 78(16):3221, 1997.

[99] Tian Zhong, Jonathan M Kindem, John G Bartholomew, Jake Rochman, Ioana Craiciu, Evan Miyazono, Marco Bettinelli, Enrico Cavalli, Varun Verma, Sae Woo Nam, et al. Nanophotonic rare-earth quantum memory with optically controlled retrieval. *Science*, 357(6358):1392–1395, 2017.

[100] W. B. Gao, A. Imamoglu, H. Bernien, and R. Hanson. Coherent manipulation, measurement and entanglement of individual solid-state spins using optical fields. *Nature Photonics*, 9:363 EP –, May 2015. Review Article.

[101] Peter Lodahl. Scaling up solid-state quantum photonics. *Science*, 362(6415):646–646, 2018.

[102] Ph. Tamarat, T. Gaebel, J. R. Rabeau, M. Khan, A. D. Greentree, H. Wilson, L. C. L. Hollenberg, S. Prawer, P. Hemmer, F. Jelezko, and J. Wrachtrup. Stark shift control of single optical centers in diamond. *Phys. Rev. Lett.*, 97:083002, Aug 2006.

[103] Shuo Sun, Jingyuan Linda Zhang, Kevin A. Fischer, Michael J. Burek, Constantin Dory, Konstantinos G. Lagoudakis, Yan-Kai Tzeng, Marina Radulaski, Yousif Kelaita, Amir Safavi-Naeini, Zhi-Xun Shen, Nicholas A. Melosh, Steven Chu, Marko Lončar, and Jelena Vučković. Cavity-enhanced raman emission from a single color center in a solid. *Phys. Rev. Lett.*, 121:083601, Aug 2018.

[104] M. Gross and S. Haroche. Superradiance: An essay on the theory of collective spontaneous emission. *Physics Reports*, 93(5):301 – 396, 1982.

[105] J.R. Johansson, P.D. Nation, and Franco Nori. Qutip 2: A python framework for the dynamics of open quantum systems. *Computer Physics Communications*, 184(4):1234 – 1240, 2013.

[106] Bartholomeus Machielse, Stefan Bogdanovic, Srujan Meesala, Scarlett Gauthier, Michael J. Burek, Graham Joe, Michelle Chalupnik, Young-Ik Sohn, Jeffrey Holzgrafe, Ruffin E. Evans, Cleaven Chia, Haig Atikian, Mihir K. Bhaskar, Denis D. Sukachev, Linbo Shao, Smarak Maity, Mikhail D. Lukin, and Marko Lončar. Quantum interference of electromechanically stabilized emitters in nanophotonic devices. *arXiv preprint arXiv:1901.09103*, 2019.

[107] M. K. Bhaskar, D. D. Sukachev, A. Sipahigil, R. E. Evans, M. J. Burek, C. T. Nguyen, L. J. Rogers, P. Siyushev, M. H. Metsch, H. Park, F. Jelezko, M. Lončar, and M. D. Lukin. Quantum nonlinear optics with a germanium-vacancy color center in a nanoscale diamond waveguide. *Phys. Rev. Lett.*, 118:223603, May 2017.

[108] Takayuki Iwasaki, Yoshiyuki Miyamoto, Takashi Taniguchi, Petr Siyushev, Mathias H. Metsch, Fedor Jelezko, and Mutsuko Hatano. Tin-vacancy quantum emitters in diamond. *Phys. Rev. Lett.*, 119:253601, Dec 2017.

[109] S. Ditalia Tchernij, T. Herzig, J. Forneris, J. Küpper, S. Pezzagna, P. Traina, E. Moreva, I. P. Degiovanni, G. Brida, N. Skukan, M. Genovese, M. Jakšić, J. Meijer, and P. Olivero. Single-photon-emitting optical centers in diamond fabricated upon sn implantation. *ACS Photonics*, 4(10):2580–2586, 2017.

[110] M.-A. Lemonde, S. Meesala, A. Sipahigil, M. J. A. Schuetz, M. D. Lukin, M. Loncar, and P. Rabl. Phonon networks with silicon-vacancy centers in diamond waveguides. *Phys. Rev. Lett.*, 120:213603, May 2018.

[111] Ronald Hanson and David D Awschalom. Coherent manipulation of single spins in semiconductors. *Nature*, 453(7198):1043–1049, 2008.

[112] Vitaly N Golovach, Alexander Khaetskii, and Daniel Loss. Phonon-induced decay of the electron spin in quantum dots. *Phys. Rev. Lett.*, 93(1):016601, 2004.

[113] G. D. Fuchs, V. V. Dobrovitski, D. M. Toyli, F. J. Heremans, C. D. Weis, T. Schenkel, and D. D. Awschalom. Excited-state spin coherence of a single nitrogen–vacancy centre in diamond. *Nature Physics*, 6:668–672, 2010.

[114] R. Orbach. Spin-lattice relaxation in rare-earth salts. *Proc. R. Soc. Lond. A*, 264(1319):458–484, December 1961.

[115] Miloš Rančić, Morgan P Hedges, Rose L Ahlefeldt, and Matthew J Sellars. Coherence time of over a second in a telecom-compatible quantum memory storage material. *arXiv preprint arXiv:1611.04315*, 2016.

[116] Benjamin Pingault, Jonas N. Becker, Carsten H. H. Schulte, Carsten Arend, Christian Hepp, Tillmann Godde, Alexander I. Tartakovskii, Matthew Markham, Christoph Becher, and Mete Atatüre. All-Optical Formation of Coherent Dark States of Silicon-Vacancy Spins in Diamond. *Phys. Rev. Lett.*, 113(26), December 2014.

[117] Gopalakrishnan Balasubramanian, Philipp Neumann, Daniel Twitchen, Matthew Markham, Roman Kolesov, Norikazu Mizuochi, Junichi Isoya, Jocelyn Achard, Johannes Beck, Julia Tissler, Vincent Jacques, Philip R. Hemmer, Fedor Jelezko, and Jörg Wrachtrup. Ultralong spin coherence time in isotopically engineered diamond. *Nature Materials*, 8(5):383–387, May 2009.

[118] E. Togan, Y. Chu, A. Imamoglu, and M. D. Lukin. Laser cooling and real-time measurement of the nuclear spin environment of a solid-state qubit. *Nature*, 478(7370):497–501, October 2011.

[119] Jiangfeng Du, Xing Rong, Nan Zhao, Ya Wang, Jiahui Yang, and RB Liu. Preserving electron spin coherence in solids by optimal dynamical decoupling. *Nature*, 461(7268):1265–1268, 2009.

[120] G De Lange, ZH Wang, D Riste, VV Dobrovitski, and R Hanson. Universal dynamical decoupling of a single solid-state spin from a spin bath. *Science*, 330(6000):60–63, 2010.

[121] L. B. Freund and S. Suresh. *Thin Film Materials: Stress, Defect Formation and Surface Evolution*. Cambridge University Press, 2004.

[122] Srujan Meesala, Young-Ik Sohn, Haig A. Atikian, Samuel Kim, Michael J. Burek, Jennifer T. Choy, and Marko Lončar. Enhanced Strain Coupling of Nitrogen-Vacancy Spins to Nanoscale Diamond Cantilevers. *Phys. Rev. Applied*, 5(3), March 2016.

[123] Martin JA Schütz. Universal quantum transducers based on surface acoustic waves. In *Quantum Dots for Quantum Information Processing: Controlling and Exploiting the Quantum Dot Environment*, pages 143–196. Springer, 2017.

[124] Juan I Cirac and Peter Zoller. Quantum computations with cold trapped ions. *Phys. Rev. Lett.*, 74(20):4091, 1995.

[125] Rusko Ruskov and Charles Tahan. On-chip cavity quantum phonodynamics with an acceptor qubit in silicon. *Phys. Rev. B*, 88(6):064308, 2013.

[126] Immo Söllner, Leonardo Midolo, and Peter Lodahl. Deterministic Single-Phonon Source Triggered by a Single Photon. *Phys. Rev. Lett.*, 116(23), June 2016.

[127] Justin D. Cohen, Seán M. Meenehan, Gregory S. MacCabe, Simon Gröblacher, Amir H. Safavi-Naeini, Francesco Marsili, Matthew D. Shaw, and Oskar Painter. Phonon counting and intensity interferometry of a nanomechanical resonator. *Nature*, 520(7548):522–525, April 2015.

[128] Lachlan J. Rogers, Kay D. Jahnke, Marcus W. Doherty, Andreas Dietrich, Liam P. McGuinness, Christoph Müller, Tokuyuki Teraji, Hitoshi Sumiya, Junichi Isoya, Neil B. Manson, and Fedor Jelezko. Electronic structure of the negatively charged silicon-vacancy center in diamond. *Phys. Rev. B*, 89(23), June 2014.

[129] Kenneth W. Lee, Donghun Lee, Preeti Ovartchaiyapong, Joaquin Minguzzi, Jero R. Maze, and Ania C. Bleszynski Jayich. Strain Coupling of a Mechanical Resonator to a Single Quantum Emitter in Diamond. *Phys. Rev. Applied*, 6(3), September 2016.

[130] D. P. Lake, M. Mitchell, Y. Kamaliddin, and P. Barclay. Optomechanically induced transparency and cooling in thermally stable diamond microcavities. *arXiv preprint arXiv:1712.01408*, 2017.

[131] D. Andrew Golter, Thein Oo, Mayra Amezcua, Kevin A. Stewart, and Hailin Wang. Optomechanical Quantum Control of a Nitrogen-Vacancy Center in Diamond. *Phys. Rev. Lett.*, 116(14), April 2016.

[132] D. Andrew Golter, Thein Oo, Mayra Amezcua, Ignas Lekavicius, Kevin A. Stewart, and Hailin Wang. Coupling a surface acoustic wave to an electron spin in diamond via a dark state. *Phys. Rev. X*, 6:041060, Dec 2016.

[133] Young-Ik Sohn, Srujan Meesala, Benjamin Pingault, Atikian Haig A., Jeffrey Holzgrafe, Mustafa Gundogan, Camille Stavrakas, Megan J. Stanley, Alp Sipahigil, Joonhee Choi, Mian Zhang, Jose L. Pacheco, John Abraham, Edward Bielejec, Mikhail D. Lukin, Mete Atature, and Marko Loncar. Controlling the coherence of a diamond spin qubit through its strain environment. *arXiv preprint arXiv:1706.03881*, 2017.

[134] Donghun Lee, Kenneth W Lee, Jeffrey V Cady, Preeti Ovartchaiyapong, and Ania C Bleszynski Jayich. Topical review: spins and mechanics in diamond. *Journal of Optics*, 19(3):033001, March 2017.

[135] Matt Eichenfield, Jasper Chan, Ryan M. Camacho, Kerry J. Vahala, and Oskar Painter. Optomechanical crystals. *Nature*, 462:78–82, 2009.

[136] Rishi N. Patel, Christopher J. Sarabalis, Wentao Jiang, Jeff T. Hill, and Amir H. Safavi-Naeini. Engineering phonon leakage in nanomechanical resonators. *Phys. Rev. Applied*, 8:041001, Oct 2017.

[137] Jasper Chan, Amir H. Safavi-Naeini, Jeff T. Hill, Seán Meenehan, and Oskar Painter. Optimized optomechanical crystal cavity with acoustic radiation shield. *Applied Physics Lett.*, 101(8):081115, 2012.

[138] Sara Mouradian, Noel H. Wan, Tim Schröder, and Dirk Englund. Rectangular photonic crystal nanobeam cavities in bulk diamond. *Applied Physics Lett.*, 111(2), 2017.

[139] Edo Waks and Jelena Vuckovic. Dipole induced transparency in drop-filter cavity-waveguide systems. *Phys. Rev. Lett.*, 96:153601, Apr 2006.

[140] C. L. Garrido Alzar, M. A. G. Martinez, and P. Nussenzveig. Classical analog of electromagnetically induced transparency. *American Journal of Physics*, 70(37), 2002.

[141] Jarryd J. Pla, Kuan Y. Tan, Juan P. Dehollain, Wee H. Lim, John J. L. Morton, David N. Jamieson, Andrew S. Dzurak, and Andrea Morello. A single-atom electron spin qubit in silicon. *Nature*, 489:541–545, 2012.

[142] Jonas Nils Becker, Johannes Görlitz, Carsten Arend, Matthew Markham, and Christoph Becher. Ultrafast all-optical coherent control of single silicon vacancy colour centres in diamond. *Nature Communications*, 7:13512, November 2016.

[143] K V Kepesidis, S D Bennett, S Portolan, M D Lukin, and P Rabl. Phonon cooling and lasing with nitrogen-vacancy centers in diamond. *Phys. Rev. B*, 88(6):064105, June 2013.

[144] M.-A. Lemonde, S. Meesala, A. Sipahigil, M. J. A. Schuetz, M. D. Lukin, M. Loncar, and P. Rabl. Phonon networks with silicon-vacancy centers in diamond waveguides; supplementary information. *Phys. Rev. Lett.*, 120:213603, May 2018.

[145] K. V. Kepesidis, M.-A. Lemonde, A. Norambuena, J. R. Maze, and P. Rabl. Cooling phonons with phonons: Acoustic reservoir engineering with silicon-vacancy centers in diamond. *Phys. Rev. B*, 94:214115, Dec 2016.

[146] Peter Lodahl, Sahand Mahmoodian, and Søren Stobbe. Interfacing single photons and single quantum dots with photonic nanostructures. *Rev. Mod. Phys.*, 87:347–400, May 2015.

[147] Peter Zoller and C. W. Gardiner. Quantum noise in quantum optics: the stochastic schrödinger equation. *arXiv:quant-ph/9702030*, 1997.

[148] S. Massar and S. Popescu. Optimal extraction of information from finite quantum ensembles. *Phys. Rev. Lett.*, 74:1259–1263, Feb 1995.

[149] S J M Habraken, K Stannigel, M D Lukin, P Zoller, and P Rabl. Continuous mode cooling and phonon routers for phononic quantum networks. *New Journal of Physics*, 14(11):115004, nov 2012.

[150] K. Jahne, B. Yurke, and U. Gavish. High-fidelity transfer of an arbitrary quantum state between harmonic oscillators. *Phys. Rev. A*, 75:010301, Jan 2007.

[151] Alexander N. Korotkov. Flying microwave qubits with nearly perfect transfer efficiency. *Phys. Rev. B*, 84:014510, Jul 2011.

[152] U. Dorner and P. Zoller. Laser-driven atoms in half-cavities. *Phys. Rev. A*, 66:023816, Aug 2002.

[153] Tomás Ramos, Vivishek Sudhir, Kai Stannigel, Peter Zoller, and Tobias J. Kippenberg. Nonlinear quantum optomechanics via individual intrinsic two-level defects. *Phys. Rev. Lett.*, 110:193602, May 2013.

[154] Rishi N. Patel, Zhaoyou Wang, Wentao Jiang, Christopher J. Sarabalis, Jeff T. Hill, and Amir H. Safavi-Naeini. Single-mode phononic wire. *Phys. Rev. Lett.*, 121:040501, Jul 2018.

[155] A. Goban, C.-L. Hung, S.-P. Yu, J.D. Hood, J.A. Muniz, J.H. Lee, M.J. Martin, A.C. McClung, K.S. Choi, D.E. Chang, O. Painter, and H.J. Kimble. Atom–light interactions in photonic crystals. *Nature Communications*, 5:3808, 2014.

[156] M. V. Gurudev Dutt, L. Childress, L. Jiang, E. Togan, J. Maze, F. Jelezko, A. S. Zibrov, P. R. Hemmer, and M. D. Lukin. Quantum register based on individual electronic and nuclear spin qubits in diamond. *Science*, 316(5829):1312–1316, 2007.

[157] Andreas Reiserer, Norbert Kalb, Machiel S. Blok, Koen J. M. van Bemmelen, Tim H. Taminiau, Ronald Hanson, Daniel J. Twitchen, and Matthew Markham. Robust quantum-network memory using decoherence-protected subspaces of nuclear spins. *Phys. Rev. X*, 6:021040, Jun 2016.

[158] Inc. Materials Design. Elastic properties of diamond. Technical report, 2017.

[159] element six ™, April 2017.

[160] F. Maier, M. Riedel, B. Mantel, J. Ristein, and L. Ley. Origin of surface conductivity in diamond. *Phys. Rev. Lett.*, 85:3472–3475, Oct 2000.

[161] Kenneth Chien-Ying Chen, Larry Kevin Warne, Yau Tang Lin, Robert L Kinzel, Johnathon D Huff, Michael B McLean, Mark W Jenkins, and Brian M Rutherford. Conductor fusing and gapping for bond wires. *Progress In Electromagnetics Research M*, 31:199–214, 2013.

[162] Comsol multiphysics® v. 5.2.

[163] Sheng Zhan, Micheal H Azarian, and Michael G Pecht. Surface insulation resistance of conformally coated printed circuit boards processed with no-clean flux. *IEEE transactions on electronics packaging manufacturing*, 29(3):217–223, 2006.

[164] John Sealy Townsend. Oxford University Press, 1915.

[165] Fabian W Strong, Jack L Skinner, Paul M Dentinger, and Norman C Tien. Electrical breakdown across micron scale gaps in mems structures. In *MOEMS-MEMS 2006 Micro and Nanofabrication*, pages 611103–611103. International Society for Optics and Photonics, 2006.

[166] Lachlan J Rogers, Kay D Jahnke, T Teraji, Luca Marseglia, Christoph Müller, Boris Naydenov, Hardy Schauffert, C Kranz, Junichi Isoya, Liam P McGuinness, and Fedor Jelezko. Multiple intrinsically identical single-photon emitters in the solid state. *Nature Communications*, 5:4739, 2014.